SIMULTANEOUS HOT AND COLD FORGING

OF SOLID CYLINDERS

A THESIS SUBMITTED TO

THE GRADUATE SCHOOL OF NATURAL AND APPLIED SCIENCES

OF

THE MIDDLE EAST TECHNICAL UNIVERSITY

BY

KÜRŞAD KAYATÜRK

IN PARTIAL FULFILLMENT OF THE REQUIREMENTS FOR THE DEGREE OF

MASTER OF SCIENCE

IN

THE DEPARTMENT OF MECHANICAL ENGINEERING

JULY 2003

ABSTRACT

SIMULTANEOUS HOT AND COLD FORGING
OF SOLID WORKPIECES

Kayatürk, Kürşad
M.S., Department of Mechanical Engineering
Supervisor: Prof. Dr.-Ing. A. Erman Tekkaya

July 2003, 165 pages

Forging operations are widely used for manufacturing processes. Forging process is done hot, warm or cold. All three temperature ranges have advantages and disadvantages. The aim of this study is to combine the advantages of hot and cold forging in a flange forming process with cylindirical workpieces in a single step. The process idea is the partial heating of the workpiece at locations where large deformations occur and to keep the parts of the workpiece cold at regions where high precision forming is required. Firstly, the process idea has been investigated virtually by the finite element method supplying the theoretical verification of the feasibility of the novel process. By this analysis also the process limits have been estimated. All analysis are based on an elasto-plastic large strain material law with thermomechanical coupling. The experimental part of the study served to realize the new process idea and to verify the process window. In the experimental study two different materials, three different part geometries and different initial conditions such as temperature field, lubrication etc. have been investigated. The specifimens are heated by induction.

Keywords: Cold Forging, Hot Forging, Experimental Verifications, Finite Element Analysis, Induction Heating

ÖZ

SİLİNDİRİK MALZEMELERDE EŞZAMANLI OLARAK
SICAK VE SOĞUK DÖVME İŞLEMİ

Kayatürk, Kürşad
Yüksek Lisans, Makina Mühendisliği Bölümü
Tez Yöneticisi: Prof. Dr.-Ing. A. Erman Tekkaya

Temmuz 2003, 165 sayfa

Dövme işlemi, üretim amaçlı olarak geniş bir kullanım alanına sahiptir. Dövme işlemi sıcak, ılık veya soğuk olarak yapılabilir. Her biri avantaj ve dezavantajlara sahiptir. Bu çalışmanın amacı sıcak ve soğuk dövme işleminin avantajlarını, silindirik malzemelerde, tek basamaklı dövme işlemi sırasında birleştirmektir. Yüksek deformasyona maruz kalan bölgelerin kısmi ısıtılması ve yüksek kesinlik istenen bölgelerin soğuk tutulması, yöntemin ana fikridir. Öncelikli olarak, bu yeni üretim fikrinin, sanal olarak, sonlu elemanlar yöntemi ile olabilirliği incelenmiştir. Bu analiz sayesinde, yöntem sınırları belirlenmiştir. Tüm analizler termo-mekanik kenetlenmiş elasto-plastik yüksek genlemeli malzeme modelleri üstüne kurulmuştur. Çalışmanın deneysel kısmı, yeni yöntem fikrinin gerçekleştirilmesine ve yöntem penceresinin belirlenmesine yardımcı olmuştur. Deneysel çalışma esnasında, iki değişik malzeme, üç değişik parça geometrisi ve yağlama, sıcaklık dağılımı gibi değişik başlangıç şartları incelenmiştir. Örnekler indüksiyon ile ısıtılmıştır.

Anahtar Kelimeler: Soğuk Dövme, Sıcak Dövme, Deneysel Doğrulamalar, Sonlu Eleman Analizleri, İndüksiyon Isıtma

ACKNOWLEDGEMENT

I would like to express my deepest gratitude and appreciation to my supervisor Prof. Dr.-Ing. A . Erman Tekkaya, Dr.-Ing. Ursula Weidig and Prof. Dr.-Ing. Kurt Steinhoff, who inspired, encouraged and supported me for this study.

I would like to thank to my colleagues Ahmet Kurt, Christian Schelle, Tiziano Minghetti, Gürol İpek whose help and guidance made great contribution to this work. I am very grateful to Karl Zurfluh, Hans Zurfluh and Urs Ziegler for their help during the tests and Rudolf Gisler in metallurgy laboratory in RUAG Munition.

This study was carried out at METU and RUAG Munition as a cooperative research project. The support provided by METU Graduate School of Natural and Applied Sciences and RUAG Munition is greatly acknowledged.

I would like to thank my colleauges Tahir FİDAN and İ. Erkan Önder for their help in this study.

The greatest thanks go to my parents and my brother for their endless support and trust throughout my education.

I would like to thank to Prof. Dr. Ing. A. Erman Tekkaya for his great patience and support without his understanding this thesis cannot be completed.

TABLE OF CONTENTS

LIST OF TABLES

TABLE

LIST OF FIGURES

FIGURE

CHAPTER 1

INTRODUCTION

Metal forming is defined in DIN 8580 as the manufacture by way of plastic deformation of a solid body while retaining its mass and material composition. Hence, forming does not belong to the group of metal-cutting manufacturing methods.

Metal forming methods are divided into three groups according to process temperature, (Figure 1.1).

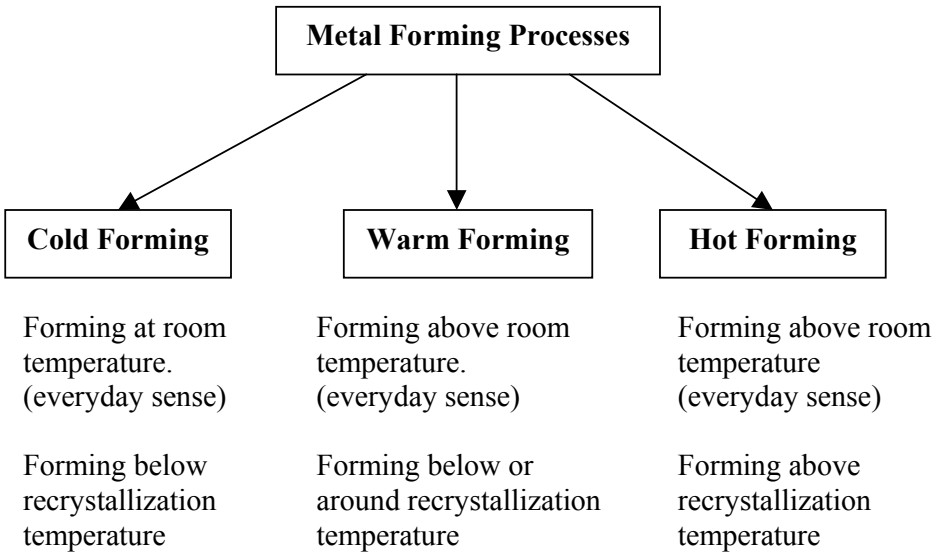

Figure 1.1 Classification of metal forming processes according to process temperature

The benefits of cold formation processes (low machining, high surface qualities) are generally lost when it comes to the production of workpieces with flanges. Poor formability due to excessive work hardening limits the possible flange diameters. Low strains at one formation step are the reason for lots of intermediate annealings and formation steps or the choice of a hot formation process with its known disadvantages (scaling, low tolerances, poor surfaces).
The advantages and disadvantages of both forming techniques are compared below.

Benefits of cold working processes are:

1- Surface quality is superior when compared to other processes.
2- Superior dimensional accuracy is achieved (near net shape).
3- Mechanical properties of the product are improved by strain hardening.
4- Less material is wasted.
5- No heating is required.

Disadvantages of cold working processes are:

1- Low formability of the material
2- Higher punch forces are required.
3- More forming steps are required.
4- Metal surfaces must be clean.

While the benefits of hot working are:

1- High formability of the material.
2- Few formations steps are required.
3- Lower punch forces are required

Disadvantages of hot forming are:

1- Scale forming on the surface need to be processed.
2- Low tolerances require additional steps.
3- Poor surface quality.

For reducing the amount of deformation steps a combination of cold and hot forming has been proposed by Körner & Knödler [15]. Their suggestion was to start with a hot forging process with high strains followed by cold forging for the final deformation steps. New processing concepts describe how to integrate a partial heating for the following upsetting into a processing line [14]. But the cold parts of the workpiece remain undeformed. In contrast to this the new process, described in the following, combines both forging types (cold and hot forging) in a way that they occur simultaneously in one deformation step. It benefits from the advantages of cold and hot forging whilst it reduces the disadvantages to a minimum as described in previous page. This kind of deformation process can be realised in an industrial process in a way as indicated in Figure 1.2.

The process is detailed as follows:
Step 1: An industrial robot is equipped with an induction coil integrated in the gripping device. During the positioning of the workpiece the heating of desired area to high temperature above recrystallization temperature takes place.

Step 2: After this heating process. The workpiece will be positioned in the setup deformation process begins while the ends of the workpieces are below cold forging temperatures.

Step 3: The workpiece is forged. The middle of the workpiece is hot forged while the ends are cold forged simultaneously.

Step 4: A second industrial robot with another modified gripping device removes the workpiece afterwards. During this operation a controlled cooling of the heated area can be realised by integrating water cooling jets into the gripper of the robot to have desired mechanical properties for the flange. As a result of these steps the stock piece [Figure 1.3a] will be formed into final product [Figure 1.3b].

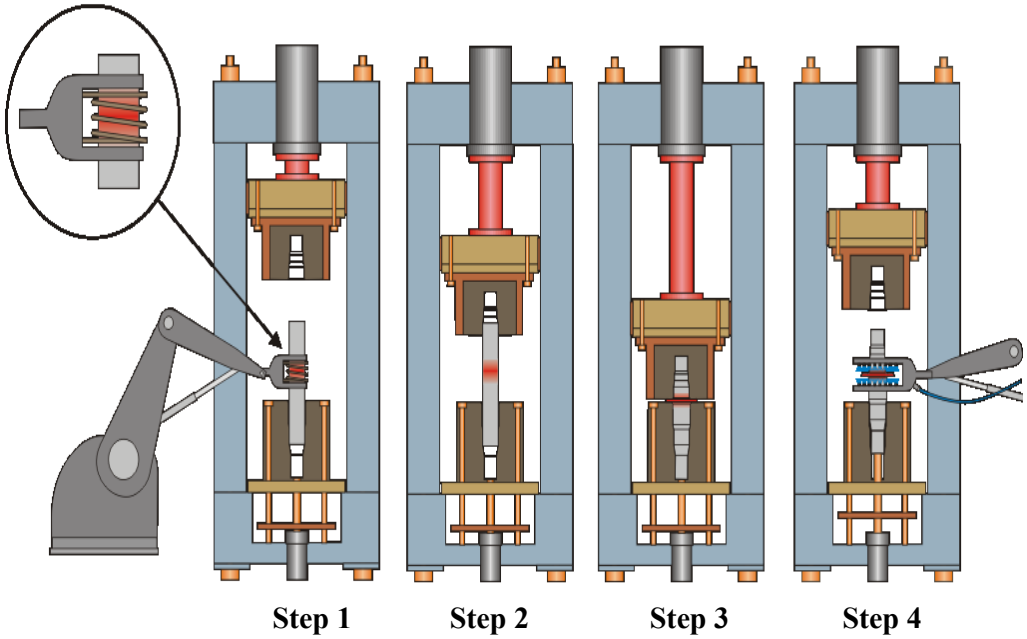

Figure 1.2 Simultaneous hot and cold forging process steps.

The aim of this study is develop a new process like the ones proposed by [14] and [15]. This new process will overcome the limits of cold forging and hot forging by combining both. The new process is named as "Simultaneous hot and cold forging" because of its nature. The simultaneous hot and cold forging process has been analyzed both experimentally and with Finite Element Analysis (FEA) technique.

The FEA reduces the number of experiments required for the development of the process thus reducing the costs. Because of this reason today manufacturing industry utilizes CAM, CAD and CAE techniques. These techniques also can speed up the development and productions phases.

The program used for FE-analysis is MARC/Autoforge (MSC.Superform) from MSC.Software. This program was chosen because it is specialized on forging processes. This feature makes FE analysis easier because of its optimized algorithms for forging.

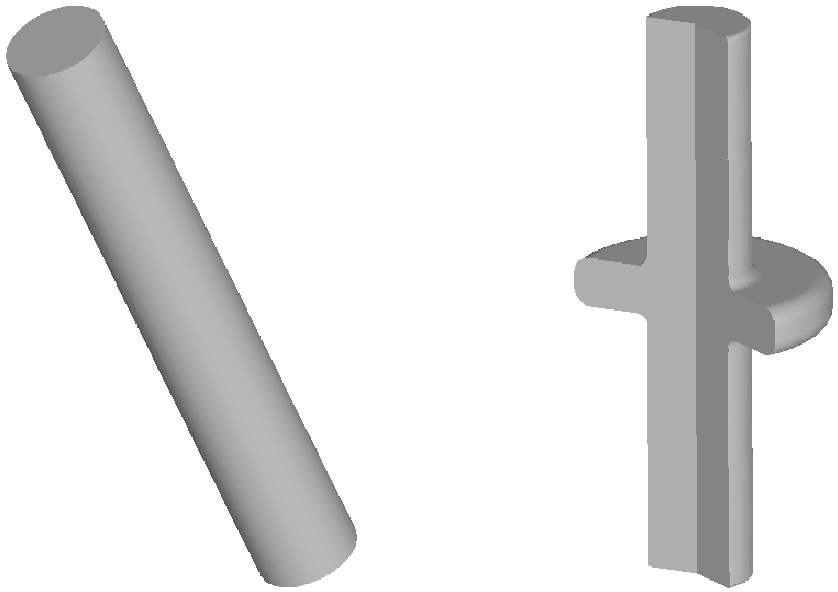

a) Initial Geometry **b)** Final Geometry

Figure 1.3 Simultaneous hot and cold forging intial stock piece and the final product.

This thesis is divided into nine chapters. This chapter "Introduction" is focused on the overview of the new process idea and the aim & scope of the study. In Chapter 2 literature survey, the previous work done on this subject is discussed. The FE-analysis background is discussed in Chapter 3 FEM Basics. Chapter 4 is focused on some analytical formulations. Basic force calculation of the extrusion force and the buckling formulation is also introduced in Chapter 4. Chapter 5 gives insight about the experiment setup and experimental results. In Chapter 6, the metallurgical properties of the final products of the experiments are investigated. The FE-analysis about the simultaneous hot and cold forging process is done in Chapter 7. The effects of parameters are discussed on the basis of the results of the FE simulations. Chapter 8 compares results of experiments with FEM simulations. Finally, Chapter 9 gives the overall conclusion of the thesis and puts recommendations for further development of the process.

CHAPTER 2

LITERATURE SURVEY

2.1 Introduction

In this chapter, first the local heating and its technologies will be discussed. Secondly, the upsetting process and the application of the local heating to the upsetting process will be discussed.

2.2 Local Heating

The aim of local heating is to extend the process limits. Larger strains and better die filling can be achieved without cracking and possibly even without adverse effects on the microstructure (texture, embrittlement etc). Local heating method enables the utilization of the advantages of both hot and cold forming. Also the cost of the process drops because of less energy spent to heat the workpiece when compared to heating of the whole workpiece.

There are several ways of local heating, the widely used ones are:

a. Induction heating
b. Laser heating
c. Electro upsetting

2.2.1 Induction Heating

Induction heating is a method of providing fast, consistent heat for manufacturing applications which involve bonding or changing the properties of metals or other electrically conductive materials. The process relies on electrical currents within the

material to produce heat. The basic components of an induction heating system are an AC power supply, induction coil, and workpiece (material to be heated or treated). The power supply sends alternating current through the coil, generating a magnetic field. When the workpiece is placed in the coil and enters the magnetic field, eddy currents are induced within the workpiece, generating precise amounts of clean, localized heat without any physical contact between the coil and the workpiece [18] (Figure 2.1). One important point in induction heating is that the workpiece should be rotated at bout 600 rpm [18]. The reason is that the ends of the coil are not flat and the heated region also will not have flat regions if the workpiece heated held static inside the coil (Figure 2.2). The rotation speed found by Ameritherm experimentally.

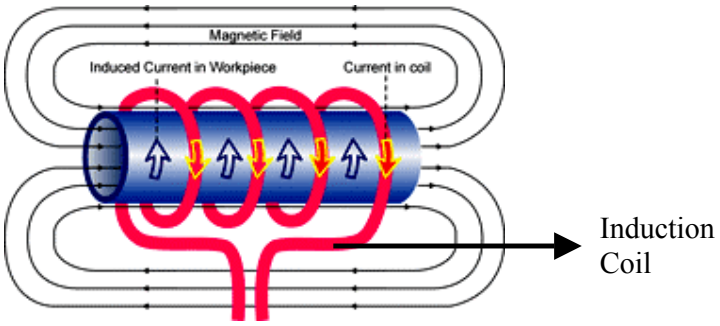

Figure 2.1 Induction heating principle

Advantages of induction heating are [18] :

a. Maximum repeatability: The heating pattern is always the same for a given setup.
b. Faster cycle time: Heating rate is higher than the conventional techniques
c. Local Heating: Small areas can be heated without affecting the surrounding areas.
d. Environmentally sound: A non-polluting process

Disadvantages of induction heating are:

a. Process is limited to ferro-metals
b. Every workpiece requires a special induction coil.

2.2.2 Laser Heating

Laser heating is a fast and localized heating method. The laser beam is a high energy that is focused on a small point. The powerful lasers mostly are not visible to human beings. The boundary between the heated region and the other areas is thin. The laser heating can be used in variety of areas. Some of them are health, defence and manufacturing. For example, laser can be used in sheet metal-forming for bending operations. Bending of a sheet metal (Figure 2.2) by laser induced thermal stresses can be used for rapid prototyping and other bending tasks that demand a high flexibility of the process. Experimental investigations on laser bending in the range of the temperature gradient mechanism showed an acceptable reproducibility of the bending angle and the bending radius for a wide range of applications [5].

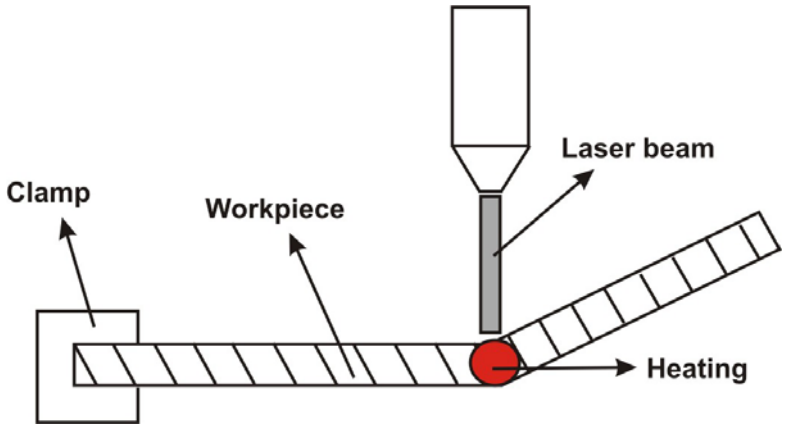

Figure 2.2 Bending with laser heating

Advantages of laser heating are:

a. Highly localized heating.
b. High precision of heating region and temperature with computer control

Disadvantages laser heating are:

a. The beam energy can only affect a few millimeters beneath the surface
b. Due to thin boundary between heated zone and the cold zone cooling rate is high.

2.2.3 Electro upsetting

Electro upsetting is used for heading of the billets. In the process the die and the punched are charged oppositely and the workpiece forms a short circuits between punch and the die. So that the part of the workpiece between die and the punch will heat up and form easily preventing buckling of the workpiece (Figure 2.3).

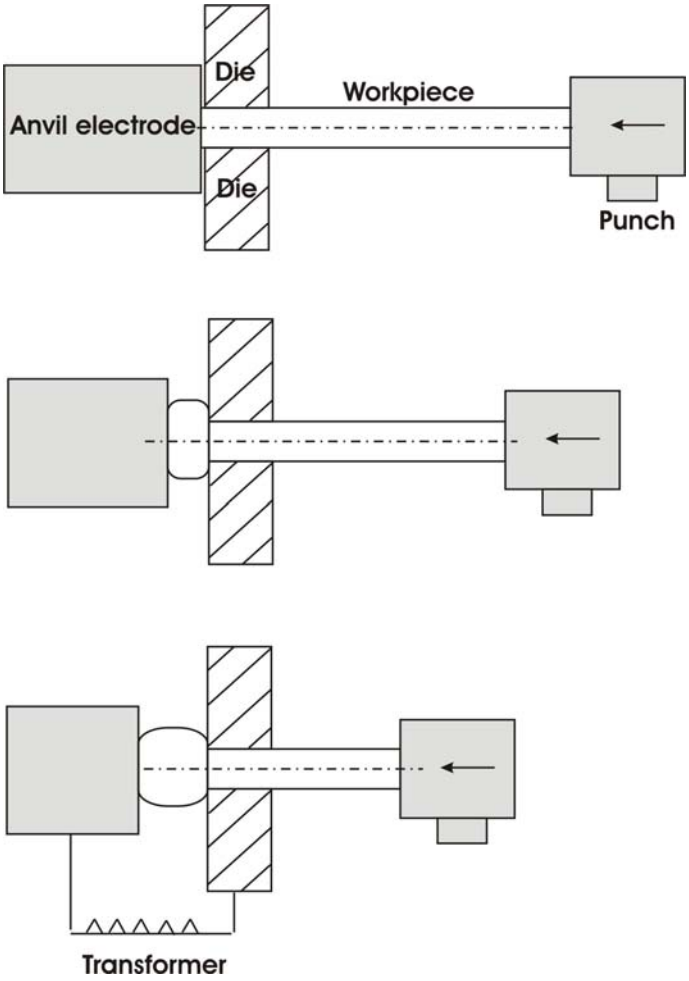

Figure 2.3 Heading with electro-upsetting [4]

2.3 Upsetting

Upsetting defined as “free forming, by which a workpiece segment is reduced in dimension between usually palne, parallel palatens,” according to DIN 8583, sheet

3 [10, 1]. Upsetting involves increasing the diameter of material by compressing its length (Figure 2.4). It also includes coining and heading. The upsetting process is the most widely used of all forging processes due its production rate [16]. Upsetting can be done both cold and hot. The upsetting of long workpieces is done in several steps with conventional methods. But these methods are limited by slenderness ratio (s) because of buckling. In single step upsetting the ratio is limited to s=2.3 [4]. The s ratio is also affected by lubrication, surface condition and the shape of the tool. The slenderness ratios for multiple step operations can be found in Table 2.1.

Table 2.1 Recommended s values [4]

One operation (single-stroke process)	$s \leq 2.3$
Two operations (two-stroke process)	$s \leq 4.5$
Three operation (three-stroke process)	$s \leq 8.0$
More than three operation (with whole die)	$s \leq 10.0$
Three operation (with split die)	$s \leq 20.0$

The effects of local heating on forming processes were studied by Merrygold [6]. The basic theory is sketched in Figure 2.4. In this study local heating is realized by oxyacetylene burner. The flame heating penetrated through the billet much faster than induction heating and therefore the heat transfer through the entire billet was much smaller. The intensive flame heat in the examples in Figure 2.5 was applied to an area of approximately 5x10 mm, where the billet length is 38.1 mm, the diameter is 25 mm and the difference in heating time yields to different product geometries. The buckling behavior of the upsetting process can also be avoided with local heating.

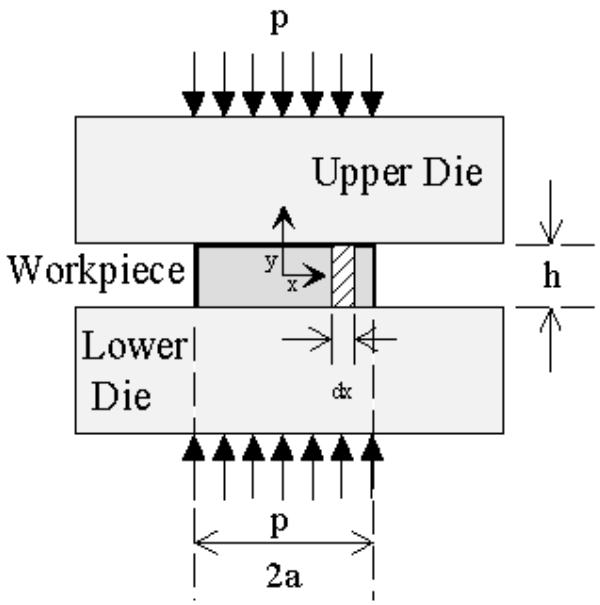

Figure 2.4 Schematic representation of upsetting [1]

Mild Carbon Steel

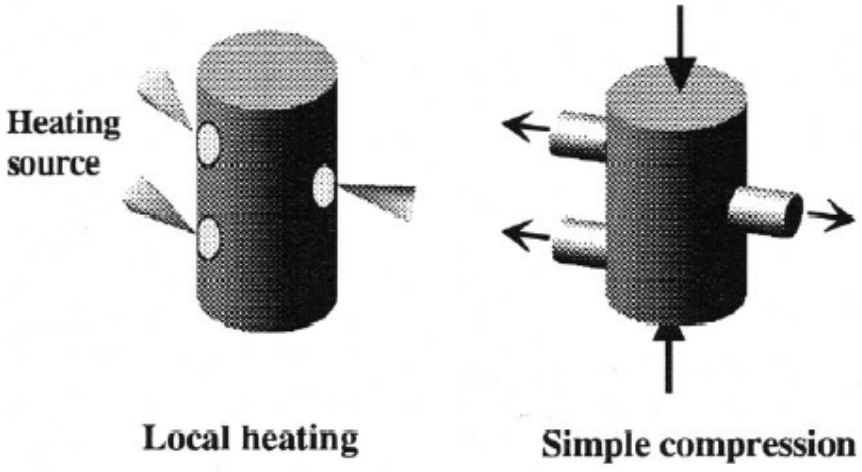

Figure 2.5 Idealised differential heating [6]

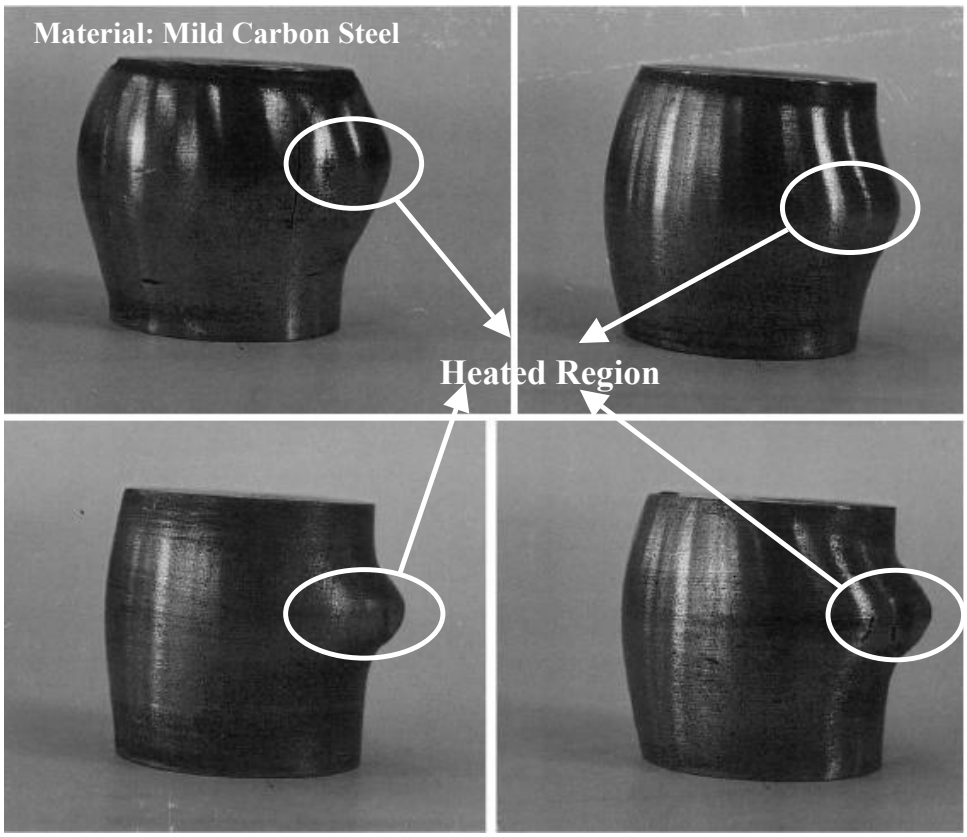

Figure 2.6 Billet local formed with different heating times [6]

Complex workpiece can also be formed using local heating. In order to produce complex geometry parts with varying deformation in more than one location using simple compression a more extensive heating system will be required. An example of the application can be demonstrated and idealised by the use of compound billets. Cylindrical aluminum billets of 25.4 mm diameter and 45 mm height were used and 3.5 mm holes were drilled through the billet section at various locations along the length of the billet. The holes were then filled with plasticine to simulate the softening of the material. Because the volume of the plasticine is much smaller compared to the volume of the billet, only a very small increment of compression is applied to the billet. Figure 2.7 shows the produced profile. It is obvious that there should not be such large gradients of yield stress along the same material but future technologies may lead to such improvements. The mode of deformation in these examples is local and anisotropic, therefore a fast heating method such as that produced by laser could enable the production of near net complex profiles.

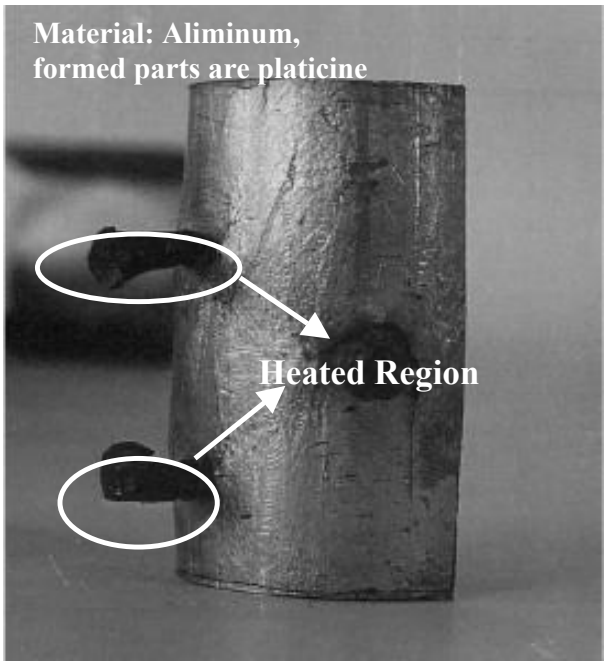

Figure 2.7 Exhibit of local heating [6]

More complex forming process is simultaneous cold and hot forging in a single forming step [13]. In this study, a long hollow workpiece is extruded at the ends and a big flange formed in the middle. In Figure 2.8 the forming steps are explained.

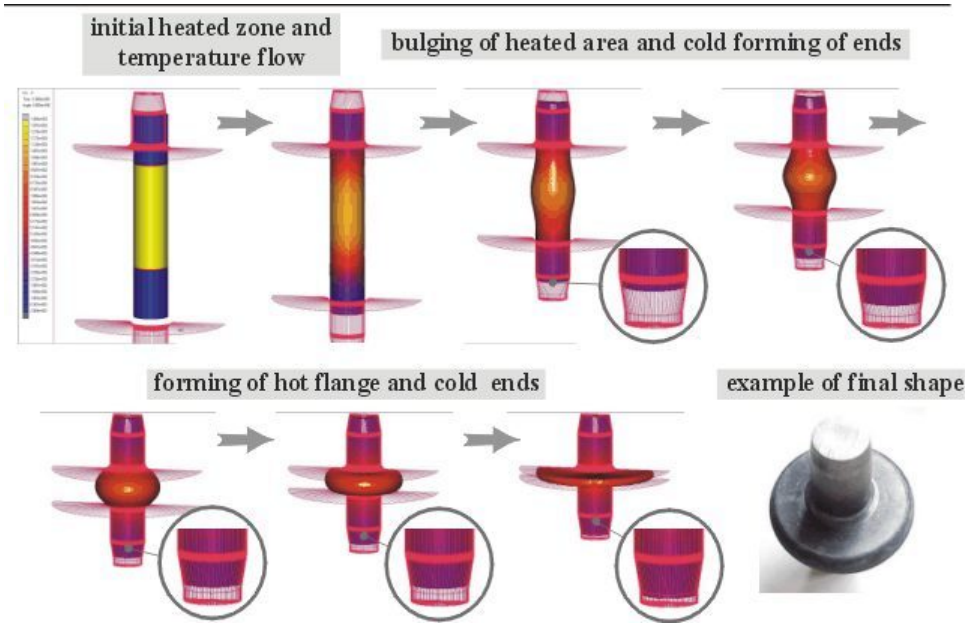

Figure 2.8 Forming steps of solid cylinders [13].

The simultaneous hot and cold forging is a solution for workpieces with local high deformations. It combines most of the advantages of cold and hot forging. The most important parameter for this process is the forming of the bulge which depends on the heated zone length and the temperature. The combination of this simulation process with a controlled cooling offers various possibilities of influencing mechanical properties with the help of heat treatments [13]. As explained above the long workpieces above the $s = 2.3$ can be easily formed without buckling.

2.4 Conclusion

In this chapter we discussed localized heating techniques and upset forging, its limitations.

Local heating is a promising development in metal forming and forming with local heating can save hardware, heating and the post processing cost accompanied with increased mechanical properties of the workpiece. Merrygold [6] used local heating with torch and induction coils successfully. Kurt [13] used induction heater and successfully formed locally heated hollow workpieces. One more important point is that Kurt [13] also successfully achieved simultaneous hot and cold forging.

The local heating can be achieved by various technologies depending on the application. While lasers are successful with sheet metal forming, it is not the same with bulk material which behaves as a semi-infinite medium. Laser heat can only penetrate a few millimeters beneath the surface which suitable for sheet metals but not for bulk metals. But the laser technology, at the moment is developing very fast so that in future the situation may change. By the help of the local heating the limitations of the upsetting processed can also be loosened.

CHAPTER 3

REVIEW OF NONLINEAR FINITE ELEMENT METHOD

3.1 Introduction

During the study, a commercial finite element package is used. In this chapter, theoretical fundamental basics of the finite element code and the meaning of some input parameters of the code will be discussed.

Idealization and discretization is the basics of the finite element. Idealization is the physical assumptions like geometry, material behavior and etc. Discretization is the next step to idealization. Discretization can be divided in two sub steps first simplifying element response.

The basic concept of the finite element method is discretization. It is constructed in the following manner. A number of finite points are defined in the solution domain and the values of the function and its derivatives, when needed, are specified at these points. These points are called nodal points or basicly nodes. The domain of the function is represented approximately by a finite collection of subdomains called finite elements. The domain then turns out to be an assemblage of elements connected together on their boundaries. The function is approximated locally within each element by continuous functions that are uniquely described in terms of the nodal-point values associated with the particular element.

The resulting equations can be divided into two categories as linear and non-linear. In linear equations structural stiffness is independent of displacement (Eqn 3.1) where nonlinear ones are dependent on displacement (Eqn 3.2).

$$\{F\} = [k] \cdot \{u\} \tag{3.1}$$

$$\{F\} = [k\{u\}] \cdot \{u\} \tag{3.2}$$

where F is force, k is the stiffness and u is the displacement field. Nonlinear equations in finite element analysis are introduced by:

a) Material nonlinearity (flow of material in plastic region, large strains {not necessary})
b) Contact nonlinearity (contact of workpiece with other workpieces or tools)
c) Geometric nonlinearity (large rotation and displacement of the system with small strains{not necessary})

3.1.1 Obtaining Elemental Stiffness Matrix

Consider a general element as in Figure 3.1, where U is displacement and f is the force acting.

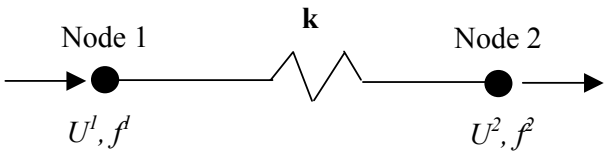

Figure 3.1 General element

From statics and the law for springs;

$$f^1 = f^2 \tag{3.3}$$

$$f^2 = -k \cdot (U^1 - U^2) \tag{3.4}$$

For a general element;

$$f^1 = k \cdot U^1 - k \cdot U^2 \tag{3.5}$$

$$f^2 = -k \cdot U^1 + k \cdot U^2 \tag{3.6}$$

Or, in matrix form;

$$\{f\} = [k] \cdot \{u\} \tag{3.7}$$

where $\{f\} = \begin{Bmatrix} f^1 \\ f^2 \end{Bmatrix}$ and $\{u\} = \begin{Bmatrix} u^1 \\ u^2 \end{Bmatrix}$ which yields to a stiffness matrix as in Equation 3.8.

$$[k] = \begin{bmatrix} k_{11} & k_{12} \\ k_{21} & k_{22} \end{bmatrix} = \begin{bmatrix} k & -k \\ -k & k \end{bmatrix} \tag{3.8}$$

In direct approach, the components k_{ij} of the elemental stiffness can be interpreted as "influence" coefficients. For example, k_{ij} is the force (response) of the element at the i^{th} node. [19]

3.1.2 Shape Functions

Consider the element in Figure 3.2 with the local coordinate system.

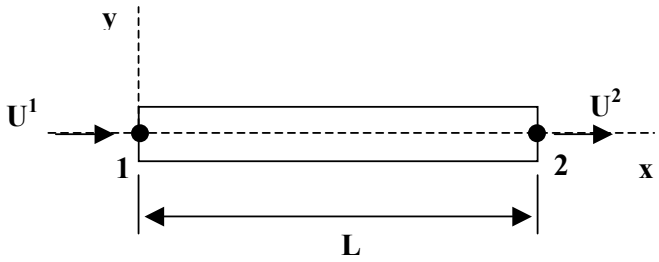

Figure 3.2 Simple element with local coordinate system

The variation of U(x) is assumed to be as

$$U(x) = \alpha \cdot x + \beta \tag{3.9}$$

The unknown coefficients (called "general coordinates") can be found by the boundary conditions

$$U(0) = U^1 \quad \text{and} \quad U(L) = U^2 \tag{3.10}$$

So Eqn. 3.9 yields to be

$$U(x) = (1 - \frac{x}{L}) \cdot U^1 + (\frac{x}{L}) \cdot U^2 \tag{3.11}$$

which can be written as

$$U(x) = N^1 \cdot U^1 + N^2 \cdot U^2 \tag{3.12}$$

In matrix form it yields to

$$U(x) = [N] \cdot \{U\} \tag{3.13}$$

N matrice is defined as the local shape function. Shape functions helps us to define the weight of the nodal deformations on the element.

3.1.3 Tranformation to The Global System

As can be seen in Figure 3.3, local coordiante system will be converted to the global system by means of a transformation matrix.

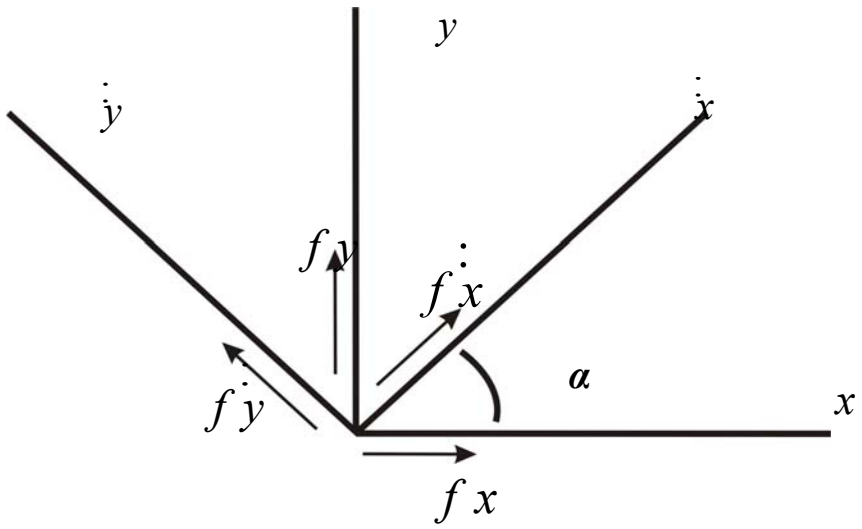

Figure 3.3 Transformation of local coordinate system

Having the relations between the local and global system as rotation, one can write down the relations as follows

$$fx^1 = \dot{f}\dot{x}^1 \cdot \cos\alpha \tag{3.14}$$

$$fy^1 = \dot{f}\dot{y}^1 \cdot \sin\alpha \tag{3.15}$$

In matrix form all the variables can be expressed as

$$\begin{Bmatrix} fx^1 \\ fy^1 \\ fx^2 \\ fy^2 \end{Bmatrix} = \begin{vmatrix} \cos\alpha & 0 \\ \sin\alpha & 0 \\ 0 & \cos\alpha \\ 0 & \sin\alpha \end{vmatrix} \cdot \begin{Bmatrix} \dot{f}\dot{x}^1 \\ \dot{f}\dot{x}^2 \end{Bmatrix} \tag{3.16}$$

In a more general form, the equations will include the *A* matrix which is named as the transformation matrix.

$$\{f\} = [A]^T \cdot \left\{\dot{\dot{f}}\right\} \tag{3.17}$$

Subtituting Eqn. (3.1)

$$\{f\} = [A]^T \cdot \left[\dot{\dot{K}}\right] \cdot \left\{\dot{\dot{U}}\right\} \tag{3.18}$$

Similar to force components, displacement componenets can also be related as

$$\dot{U}^1 = U^1 \cdot \cos\alpha + V^1 \cdot \sin\alpha \tag{3.19}$$

$$\dot{U}_2 = U_2 \cdot \cos\alpha + V_2 \cdot \sin\alpha \tag{3.20}$$

In matrix form

$$\begin{Bmatrix} \dot{U}_1 \\ \dot{U}_2 \end{Bmatrix} = [A] \cdot \begin{Bmatrix} U_1 \\ V_1 \\ U_2 \\ V_2 \end{Bmatrix} \tag{3.21}$$

$$\left\{\dot{U}\right\} = [A] \cdot \{U\} \tag{3.22}$$

Eqn. (3.22) with (3.17) yields to

$$\{f\} = [A]^T \cdot \left[\dot{K}\right] \cdot [A] \cdot \{U\} \tag{3.23}$$

With the help of Eqn. (3.23), global stiffness matrix can be expressed as

$$[K] = [A]^T \cdot \left[\dot{K}\right] \cdot [A] \tag{3.24}$$

3.1.4 Numerical Solution of Equations

In metal forming applications equations are highly nonlinear with material, geometric and contact nonlinearities. Solution of the equations are by means of numerical methods. These methods are mainly Euler method, self correcting Euler method, direct iteration method, the Newton-Raphson method, modified Newton-

Raphson method, quasi Newton-Raphson method and BFGS. In the simulations with MARC, Newton-Raphson method is used as numerical solver of equations (Figure 3.4).

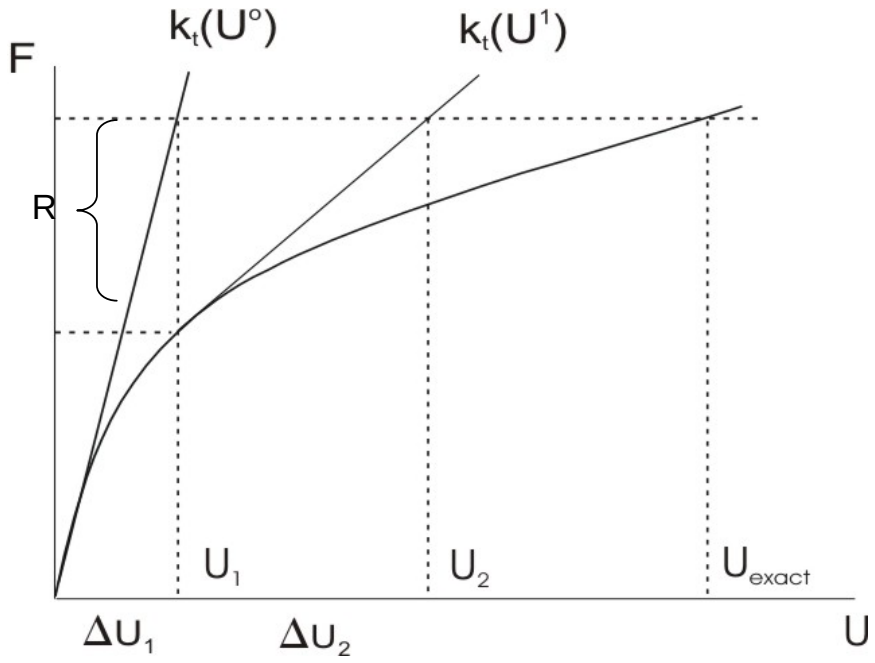

Figure 3.4 Newton-Raphson method

Eqn (3.2), with Taylor series expansion, can be reduced to Eqn (3.25) for Newton Raphson method.

$$\left[k_t\left\{U^{i-1}\right\}\right]\cdot\left\{\Delta U^i\right\}=\left\{R\left\{U^{i-1}\right\}\right\} \tag{3.25}$$

Stability of the numerical solution with Newton-Raphson method is dependent on the initial guess. If initial guess is not good there exist a possibility of divergence of the solution.

3.1.5 Linear and Non-Linear Parts of Stiffness Matrix

Similar to Newton-Raphson method force and residuals can be related as

$$\{F\} = \{f\} - \left[\dot{k}\right] \cdot \left\{\dot{U}\right\} \tag{3.26}$$

$$-\left[\frac{\partial\left\{\dot{R}\right\}}{\partial\left\{\dot{U}\right\}}\right] \cdot \left\{\Delta\dot{U}\right\} = \left\{\dot{R}\right\} \tag{3.27}$$

Since k_t can be written as

$$\left[\dot{k}_t\right] = -\left[\frac{\partial\left\{\dot{R}\right\}}{\partial\left\{\dot{U}\right\}}\right] = \left\{\frac{\partial(\left[\dot{k}\right] \cdot \left\{\dot{U}\right\})}{\partial(\dot{U})}\right\} \tag{3.28}$$

The numerator of Eqn. (3.28) will be formulated with Eqn. (3.29).

$$\left[\dot{k}\right] \cdot \left\{\dot{U}\right\} = \frac{\partial U}{\partial\left\{\dot{U}\right\}} = \frac{\partial(U_L + U_{NL})}{\partial\left\{\dot{U}\right\}} \tag{3.29}$$

Eqn. (3.29) contains two displacement values as linear and non-linear. This will also effect the stiffness matrix as two distinct parts. With the help of Eqn. (3.29), Eqn. (3.28) will reduce to Eqn. (3.30).

$$\left[\dot{k}_t\right] = \left\{ \frac{\partial\left(\frac{\partial U_L}{\partial\left\{\dot{U}\right\}} + \frac{\partial U_{NL}}{\partial\left\{\dot{U}\right\}}\right)}{\partial\left\{\dot{U}\right\}} \right\} \tag{3.30}$$

Stiffness matrix, can be now written as two parts names as linear and non-linear.

$$\left[\dot{k}_{t,L}\right] = \frac{\partial^2 U_L}{\partial\left\{\dot{U}\right\}^2}$$

$$\left[\dot{k}_{t,NL}\right] = \frac{\partial^2 U_{NL}}{\partial\left\{\dot{U}\right\}^2} \tag{3.32}$$

$$\left[\dot{k}_t\right] = \left[\dot{k}_{t,L}\right] + \left[\dot{k}_{t,NL}\right]$$

Non-Linear displacement term in Eqn. (3.32) can be written as [21]

$$U_{NL} = \frac{1}{4}\cdot E\cdot A\cdot 1_0\cdot\left\{2\cdot\left(\frac{\dot{U}_2-\dot{U}_1}{1_0}\right)\cdot\left(\frac{\dot{V}_2-\dot{V}_1}{1_0}\right)^2 + \frac{1}{2}\cdot\left(\frac{\dot{V}_2-\dot{V}_1}{1_0}\right)^4\right\} \tag{3.33}$$

In indicial notation, Eqn. (3.32) will be converted to

$$\left(\dot{\dot{k}}_{t,NL}\right)_{ij} = \frac{\partial^2 U_{NL}}{\partial \dot{U}_i \cdot \partial \dot{U}_j} \tag{3.34}$$

In matricial notation, non-linear stiffness matrix, after the derivations will be reduced to the simplified form with linear and non-linear strain terms.

$$\left(\dot{\dot{k}}_{t,NL}\right) = \frac{E \cdot A}{l_0} \cdot \begin{bmatrix} 0 & \sqrt{2 \in_{NL}} & 0 & -\sqrt{2 \in_{NL}} \\ \sqrt{2 \in_{NL}} & \in_L + 3 \in_{NL} & -\sqrt{2 \in_{NL}} & -\in_L - 3 \in_{NL} \\ 0 & -\sqrt{2 \in_{NL}} & 0 & \sqrt{2 \in_{NL}} \\ -\sqrt{2 \in_{NL}} & -\in_L - 3 \in_{NL} & \sqrt{2 \in_{NL}} & \in_L + 3 \in_{NL} \end{bmatrix} \tag{3.35}$$

This will divide the non-linear stiffness matrix into two, named as “initial displacement” and “initial stress” matrices as in Eqn. (3.36).

$$\left(\dot{\dot{k}}_{t,ID}\right) = \frac{E \cdot A}{l_0} \cdot \begin{bmatrix} 0 & \sqrt{2 \in_{NL}} & 0 & -\sqrt{2 \in_{NL}} \\ \sqrt{2 \in_{NL}} & 2 \in_{NL} & -\sqrt{2 \in_{NL}} & -2 \in_{NL} \\ 0 & -\sqrt{2 \in_{NL}} & 0 & \sqrt{2 \in_{NL}} \\ -\sqrt{2 \in_{NL}} & -2 \in_{NL} & \sqrt{2 \in_{NL}} & 2 \in_{NL} \end{bmatrix}$$

$$\left(\dot{k}_{t,IS}\right)=\frac{P}{l_0}\cdot\begin{bmatrix}0 & 0 & 0 & 0\\ 0 & 1 & 0 & -1\\ 0 & 0 & 0 & 0\\ 0 & -1 & 0 & 1\end{bmatrix} \tag{3.36}$$

$$\left(\dot{k}_{t,NL}\right)=\left(\dot{k}_{t,ID}\right)+\left(\dot{k}_{t,IS}\right)$$

In initial stress matrix, variable P can be expressed as

$$P=E\cdot A\cdot(\in_L+\in_{NL}) \tag{3.37}$$

So Eqn. (3.32) will yield to

$$\left[\dot{k}_t\right]=\left[\dot{k}_{t,L}\right]+\left[\dot{k}_{t,ID}\right]+\left[\dot{k}_{t,IS}\right] \tag{3.38}$$

where the stiffness matrix is divided into three as, small displacement (linear) stiffness matrix, initial displacement matrix and initial stress matrix.

3.1.6 Technical Background for Total Lagrange Formulation

Starting with the equations of equilibrium, excluding the inertia effects for the body

$$\frac{\partial\sigma}{\partial x}+q=0 \tag{3.39}$$

which is true for the body in the current or deformed configuration where σ is the Cauchy or true stress tensor and q will be described as shape functions. Small letters (x,v,s) refer to the deformed configuration where capital letters (X,V,S) will refer to the undeformed configuration. The equilibrium equations are equivalent to the principle of virtual work.

$$\int_V \sigma \cdot \frac{\partial \delta u}{\partial x} \cdot dv = \int_V q \cdot \delta u \cdot dv + \int_S t \cdot \delta u \cdot ds \tag{3.40}$$

where all the integration occurs over the deformed configurations. In structural mechanics, one knows the undeformed configuration so with the help of Jacobian of the deformation one can also have the equation of virtual work in deformed configuration

$$J = \frac{dv}{dV} = \det\left(\frac{\partial x}{\partial X}\right) = \det(F) \tag{3.41}$$

$$\int_V J \cdot \sigma \cdot \frac{\partial \delta u}{\partial X} \cdot dV = \int_V Q \cdot \delta u \cdot dV + \int_S T \cdot \delta u \cdot dS \tag{3.42}$$

Introducing the symmetry second Piola-Kirchoff stress tensor, S

$$J \cdot \sigma = F^T \cdot S \cdot F \tag{3.43}$$

The principle virtual work becomes

$$\int_V S \cdot F \cdot \frac{\partial \delta u}{\partial X} \cdot dV = \int_V Q \cdot \delta u \cdot dV + \int_S T \cdot \delta u \cdot dS \tag{3.44}$$

The Green Lagrange strain is the work conjugate to the second Piola-Kirchoff stress

$$E = \frac{1}{2}\left(F^T \cdot F - I \right) \quad \text{or} \tag{3.45}$$

$$E_{ij} = \frac{1}{2}\left(\frac{\partial u_i}{\partial X_j} + \frac{\partial u_j}{\partial X_i} + \frac{\partial u_1}{\partial X_i} \cdot \frac{\partial u_1}{\partial X_j} \right) \tag{3.46}$$

The variation in the Green Lagrange Strain becomes

$$\delta E_{ij} = \frac{1}{2}\left(F_{1i} \frac{\partial \delta u_1}{\partial X_j} + \frac{\partial \delta u_1}{\partial X_i} F_{1j} \right) \tag{3.47}$$

This results in a principle of virtual work integrated over the undeformed volume

$$\int_V S^T \cdot \delta E \cdot dV = \int_V Q \cdot \delta u \cdot dV + \int_S T \cdot \delta u \cdot dS \tag{3.48}$$

For viscoelastic fluids and elastic-plastic and viscoplastic solids, the constitutive equations supply an expression for the rate of stress in terms of deformation rate, stress, deformation and sometimes other internal material parameters.

If therefore seems most obvious to differentiate the Lagrangian virtual work equation with respect to time. The rate of virtual work is readily found as

$$\int_V \left[\dot{S}_{ij} \cdot \delta E_{ij} + S_{ij} \cdot \frac{\partial v_k}{\partial X_i} \cdot \frac{\partial \delta u_k}{\partial X_j} \right] dV = \int_V \dot{Q}_i \cdot \delta u_i \cdot dV + \int_S \dot{T}_i \cdot \delta u_i \cdot dS \qquad (3.49)$$

3.1.7 Updated Lagrangian Approach

In the Updated Lagrangian Approach, the element stiffness is assembled in the current configuration of the element. The approach can be used to analyze structures where inelastic behavior causes large deformations such as those encountered in forging. The Lagrangian coordinate frame has little physical significance in these analyses since the inelastic deformations are, by definition, permanent in the body. For these analyses, the Lagrangian frame of reference is redefined at the beginning of each increment.

Although it is possible to derive theoretical constitutive equations of the type Eqn. 3.49 for most materials, it is often more suitable to specify the equations with reference to the current state. The desired formulation can be obtained by taking Eqn. 3.49 to the reference state as current state. It follows that momentarily

$$F_{ij} = \delta_{ij} \;,\; \delta E_{ij} = \delta D_{ij} \;,\; \frac{\partial}{\partial X_i} = \frac{\partial}{\partial x_i} \;,\; S_{ij} = \sigma_{ij} \qquad (3.50)$$

where F is the deformation tensor and D is the rate of deformation, and therefore, Eqn. 3.49 transforms into

$$\int_V \left[\dot{\sigma}_{ij}^{T} \cdot \delta D_{ij} + \sigma_{ij} \cdot \frac{\partial v_k}{\partial x_i} \cdot \frac{\partial \delta u_k}{\partial x_j} \right] dv = \int_V \dot{q}_i \cdot \delta u_i \cdot dv + \int_S \dot{t}_i \cdot \delta u_i \cdot ds \qquad (3.51)$$

In this equation, $\dot{\sigma}_{ij}^{T}$ is the Trusdell rate of Cauchy stress which can be obtained from the usual material rate of Cauchy stress by differentiation by

$$\dot{\sigma}_{ij} = J^{-1} F_{ik} \dot{S}_{kl} F_{jl} + J^{-1} \dot{F}_{ik} S_{kl} F_{jl} + J^{-1} F_{ik} S_{kl} \dot{F}_{jl} - \dot{J} J^{-2} F_{ik} S_{kl} F_{jl} \qquad (3.52)$$

If one converts the state to current and reference state, it follows that

$$\dot{\sigma}_{ij} = \dot{\sigma}_{ij}^{T} + \frac{\partial v_i}{\partial x_k} \cdot \sigma_{kj} + \sigma_{ik} \cdot \frac{\partial v_j}{\partial x_k} - \sigma_{ij} \cdot \frac{\partial v_k}{\partial x_k} \qquad (3.53)$$

The Truesdell rate of Cauchy stress is materially objective. That is, if rigid rotation is imposed on the material, the Trusdell rate vanishes, whereas the usual material rate does not vanish. The constitutive equations may well be formulated in terms of the Truesdell rate of Cauchy stress. It may be written as

$$\dot{\sigma}_{ij}^{T} = L_{ijkl}(\sigma_{mn}) D_{kl} \qquad (3.54)$$

The moduli L_{ijkl} are not equal to classical elastic-plastic moduli

$$L_{ijkl}^{e-p} = 2G \cdot \left[\delta_{ik} \cdot \delta_{jl} + \frac{\lambda}{2G} \cdot \delta_{ij} \cdot \delta_{kl} - \frac{3}{2} \cdot \frac{\sigma_{ij}' \cdot \sigma_{kl}'}{\sigma_o^{\,2}} \right] \qquad (3.55)$$

These moduli supply the relation between the Jaumann rate of Cauchy stress and the deformation rate

$$\dot{\sigma}_{ij}^{J} = L_{ijkl}^{e-p} D_{kl} \tag{3.56}$$

The Jaumann rate of Cauchy stress is related to the material rate of Cauchy stress with the equation

$$\dot{\sigma}_{ij}^{J} = \dot{\sigma}_{ij} - \omega_{ik} \cdot \sigma_{kj} - \sigma_{ik} \cdot \omega_{jk} \tag{3.57}$$

where the spin tensor w_{ij} is defined by

$$\omega_{ij} = \frac{1}{2}\left(\frac{\partial v_i}{\partial x_j} - \frac{\partial v_j}{\partial x_i} \right) \tag{3.58}$$

The Jaumann rate of Cauchy stress is the rate of change of the Cauchy stress in a corotational system. The material rate of Cauchy stress can be eliminated from Eqn. 3.57 with the use of Eqn. 3.58, which yields the relation

$$\dot{\sigma}_{ij}^{T} = \sigma_{ij}^{J} - D_{ik} \cdot \sigma_{kj} - \sigma_{ik} \cdot D_{kj} + \sigma_{ij} \cdot D_{kk} \tag{3.59}$$

Thus the relation between the large strain moduli and the classical elastic-plastic moduli is

$$L_{ijkl} = L_{ijkl}^{e-p} - \delta_{il} \cdot \sigma_{kj} - \sigma_{il} \cdot \delta_{kj} + \sigma_{ij} \cdot \delta_{kl} \tag{3.60}$$

Note that the last term in Eqn. 3.60 does not satisfy the usual symmetry relation. This is not relevant for material plasticity problems since the deformations are approximately incompressible. Hence, Eqn. 3.60 may be approximated by

$$L_{ijkl} = L_{ijkl}^{e-p} - \delta_{il} \cdot \sigma_{kj} - \sigma_{il} \cdot \delta_{kj} \tag{3.61}$$

3.2 Finite Element Procedures

There are two procedures available for solving these problems: a)elastic-plastic method, b) rigid-plastic method. The finite element analysis of metal forming processes using the rigid-plastic material model is very popular due to the following properties of this method [21]:

- The material does not require the consideration of the linear kinematics of the finite deformation. Hence it is less time consuming.
- Rigid-plastic formulations are numerically rather robust and reliable.
- In three-dimensional analysis it is possible to formulate linear mixed tetrahedral elements, which allow easy automatic meshing.
- The computer implementation of rigid-plastic finite element code is simple.

Beside these advantages of rigid-plastic formulations there are some serious drawbacks.

- Any elastic based property such as residual stresses and spring-back cannot be analysed by means of the rigid-plastic material law, which neglects elastic strains.
- A more serious drawback is the fact that rigid-plasticmodels utilize a pseudo-elastic description of material regions, which are assumed to be rigid. This leads to the fact that, especially in cold forming processes, friction which is always present between the tools and the workpiece in elastic regions of the workpiece is not modelled correctly.
- Another drawback is that rigid-plastic materials connot detect stress peaks, which occur at the transition between elastic and elasto-plastic material zones.

- Finally, if net shape forming porcesses are analyzed, the accuracy requirements of the analysis cannot be fulfilled usually.

In the simulations conducted by author, elasto-plastic material model was used due to its advantages. Especially in such cases as simultaneous hot and cold forging, friction parameters in the cold region are important. Elasto-plastic model increases the accuracy of the formation in cold regions.

3.3 Thermo-Mechanically coupled Analysis

High percentage of operations in the metal forming industry including forging with high strains may require a thermo-mechanically coupled analysis where thermal strains and temperature dependency of material properties should also be considered. The observed phenomena must be modelled by a coupled analysis if the following conditions are present [9]:

- The body undergoes large deformations such that there is a change in the boundary conditions associated with the heat transfer problem.

- Deformation converts mechanical work into heat through an irreversible process, which is large relative to other heat sources.

In either case, a change in the temperature distribution contributes to the deformation of the body through thermal strains and influences the material properties.
The coupled analysis is realized in a so called loose sense (Figure 3.5) [21]. At a given time step, say t, first the mechanical equilibrium equations are solved using the flow curve corresponding to the known temperature distribution at this time step. Now, the geometry at the new time step $t+\Delta t$ is updated using the velocity of step t. Then, knowing the latent heat, a purely thermal analysis is performed at time $t+\Delta t$ suppliying a new temperature distribution for this time increment. For the new

increment at time t+Δt a velocity field is computed using the flow curve at the updated temperature field.

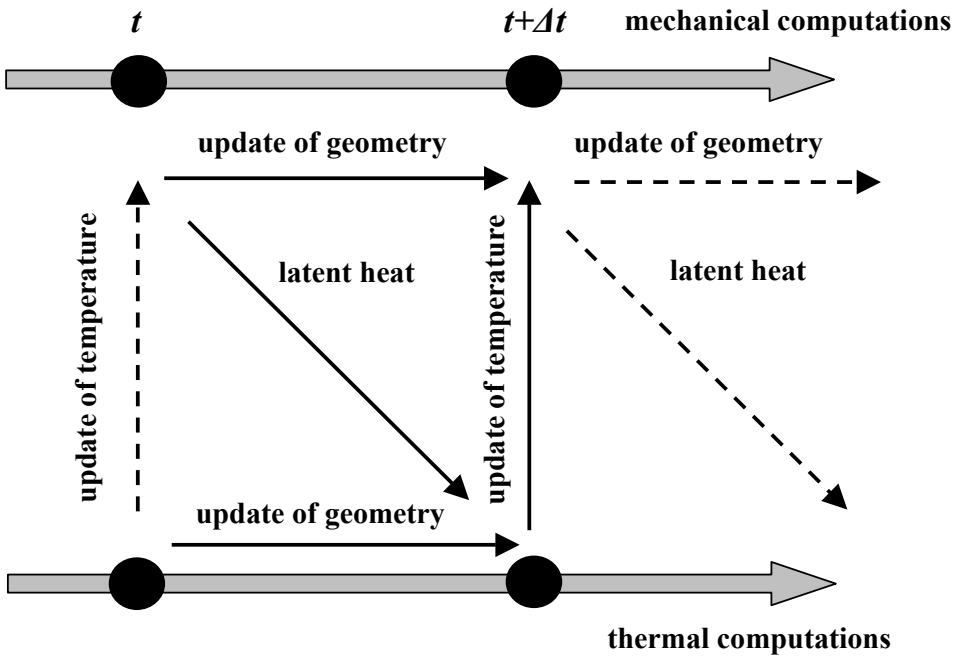

Figure 3.5 Loosely coupled thermo-mechanical analysis

This supplies a new latent heat input, from which a new temperature field at the updated geometry at time t+2Δt with a purely thermal analysis is obtained and so on.

3.4 Convergence Control of Numerical Solution

The default procedure for convergence criterion in the finite element program MARC-Autoforge is based on the magnitude of the maximum residual load to the maximum reaction force [9]. This method is appropriate since the residuals measure the out-of-equilibrium force, which should be minimized. This technique is also

appropriate for Newton-Raphson method, where zero load iterations reduce residual load. The procedure is as follows:

- Resiual Checking:

$$\frac{\left\| F_{residual} \right\|_\infty}{\left\| F_{resident} \right\|_\infty} < TOL_1 \tag{3.62}$$

$$\left\| F_{residual} \right\|_\infty < TOL_1 \tag{3.63}$$

where F is the force vector, and TOL_1 is the control tolerances. $\|F\|_\infty$ indicates the component of F with the highest absolute value. Equation 3.62 represents relative residual checking where Eqn 3.63 represents absolute residual checking.

- Displacement Checking:

$$\frac{\left\| \delta_u \right\|_\infty}{\left\| d_u \right\|_\infty} < TOL_1 \tag{3.64}$$

$$\left\| \delta_u \right\|_\infty < TOL_1 \tag{3.65}$$

where d_u is the displacement increment vector, δ_u is the displacement iteration vector. With this method, convergence is satisfied if the maximum displacement of the last iteration compared to the actual displacement change of the increment is small than tolerance value for relative convergence check (Eqn. 3.64), and for absolute check Eqn. 3.65 is valid.

3.5 Friction Modeling

Friction is a complex physical phenomenon that involves the characteristics of the surface such as roughness, temperature, normal stress and relative velocity. Since the modeling of friction can be complex with the variables defined above, it is simplified to two idealistic models [9].

The most popular friction model for cold forming is the Adhesive Friction or Coulomb Friction model (Eqn. 3.66).

$$\sigma_{fr} \leq -\mu\sigma_n \cdot t \tag{3.66}$$

where σ_n is the normal stress, σ_{fr} is the tangential (friction) stress, μ is the friction coefficient and t is the tangential vector in the direction of the relative velocity.

In contact problems, often neutral lines develop which means that along a contact surface, the material flows in one direction in a part of the surface, and in the other direction in another part (Figure 3.6). This discontinuity in the value of σ_{fr} can result in numerical difficulties. During the simulations the solver can overcome these difficulties by smoothing the friction line (Figure 3.6).

Second friction model is the shear model as shown in Eqn. 3.67.

$$\sigma_{fr} \leq -m\frac{\sigma_n}{\sqrt{3}} \cdot t \tag{3.67}$$

Shear friction model is generally used for the friction modeling in hot regions. Since simultaneous hot and cold forging collects both cold and hot regions under friction forces, a combination of both seems the right way to model friction. But the deformation in hot region takes most of the formation time and the velocities are

higher than the cold formed region. So shear friction model will be used in the simulations.

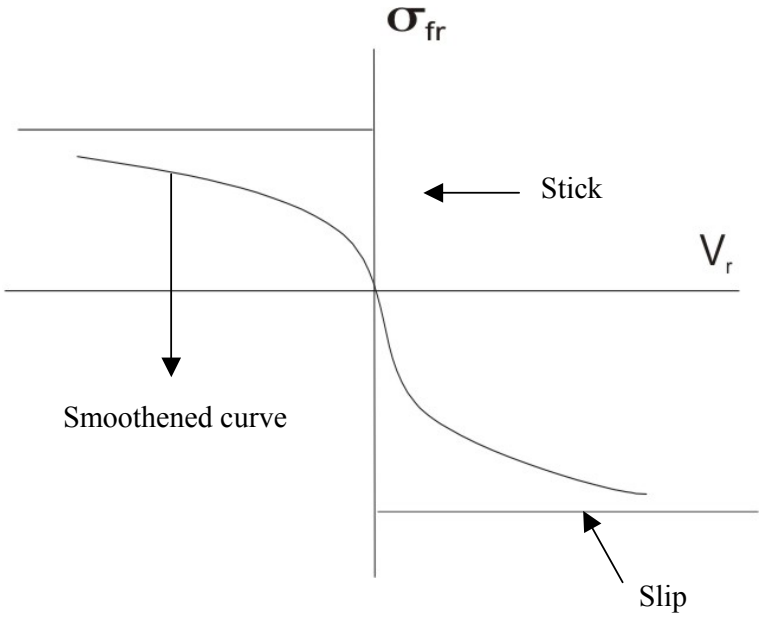

Figure 3.6 Smoothening of the curve

CHAPTER 4

ANALYTICAL METHODS

4.1 Introduction

Metal forming processes are commonly complex processes. FEA is generally used to solve the complex problems numerically. But FEA may include wrong assumptions about the problem. It is necessary to verify if the FEA results can be verified by analytical methods. These methods may not give the exact results but they may enable to verify the order of magnitude of the results at least. If FEA and analytical methods have completely different results then the user will have a warning. This means that one or more parameters used into simulation are wrong. In this chapter, the extrusion phase force and the buckling ratios will be calculated. The extrusion phase is the beginning of the process. The workpiece will extrude at both ends than it will be upset in the middle.

4.2 Analytical Solution Methods

Methods present several different analytical solutions for axis-symmetric extrusion processes.

a- Lower Bound Theorem

b- Upper Bound Theorem

c- Empirical methods

The upper bound and lower bound analyses are designed so that the actual power or stress requirement is less than that predicted by upper bound and greater than that

predicted by the lower bound. Lower bound and the upper bound reduce the uncertainty of the actual power requirement. Upper and lower bounds will permit the determination of such quantities as required forces, limitations on the process, optimal die design, flow patterns, and prediction and prevention of defects. For both upper and the lower bound solution is the division of the workpiece body into zones. For each of the zones there is written either a velocity field (upper bound) or a stress field (lower bound). A better choice of zones and fields brings the calculated values closer to the actual values. In this work, upper bound method with triangular velocity field is used to find extrusion forces.

4.2.1 Upper Bound Method

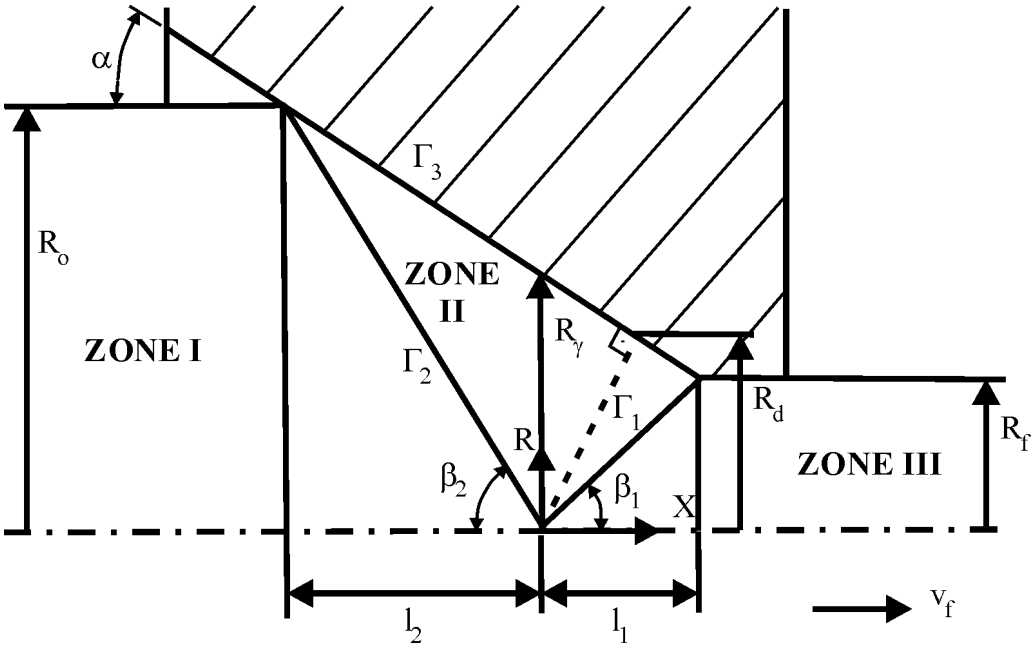

Figure 4.1 Modeling of Upper Bound Method (Triangular velocity field) [20]

Upper bound method can be used to analyze axis-symmetric metal forming such as forging, extrusion, and rolling. In upper bound, a kinematically admissible velocity field has to be set for each zone and the total consumption energy is calculated by summing up all zonal consumption energies. In the basic axis-symmetric extrusion problem, three velocity zones are assumed. The zones III and I have only horizontal velocity component. Forward rod extrusion is conically

converging flow in zone II so a triangular velocity field is assumed. In triangular velocity field model Γ_1 and Γ_2 are the surfaces of velocity discontinuities. These surfaces are conical to satisfy the axis-symmetry. The intersection point of these surfaces assumed arbitrarily. The velocities change their direction at these surfaces. The input velocity in zone I and the output velocity in zone III are related by volume constancy

4.2.1.1 Determination of the Velocity Field in Zone II

Γ_2 discontinuity surface can be determined by using the relation between the radius on that surface point R_Γ and the axial distance X_Γ (Figure 4.2).

$$R_\Gamma = R_0 - Z_\Gamma \tan\beta = R_0 - (l_2 + X_\Gamma)\tan\beta \tag{4.1}$$

As described previously any material entering the Γ_2 surface at X_Γ, R_Γ with respect to the intersection point of surfaces Γ_2 and Γ_1 flows in zone II parallel to the die surface. So the coordinates can be obtained using Equation (4.2)

$$R = R_\Gamma - (Z - Z_\Gamma)\tan\alpha = R_\Gamma - (X - X_\Gamma)\tan\alpha \tag{4.2}$$

Combining Equations (4.1) and (4.2):

$$R_\Gamma = \frac{R + [X + l_2 - (R_0 / \tan\beta)]\tan\alpha}{1 - (\tan\alpha / \tan\beta)} \tag{4.3}$$

Also from geometric relations:

$$l_2 = \frac{R_0}{\tan\beta} \tag{4.4}$$

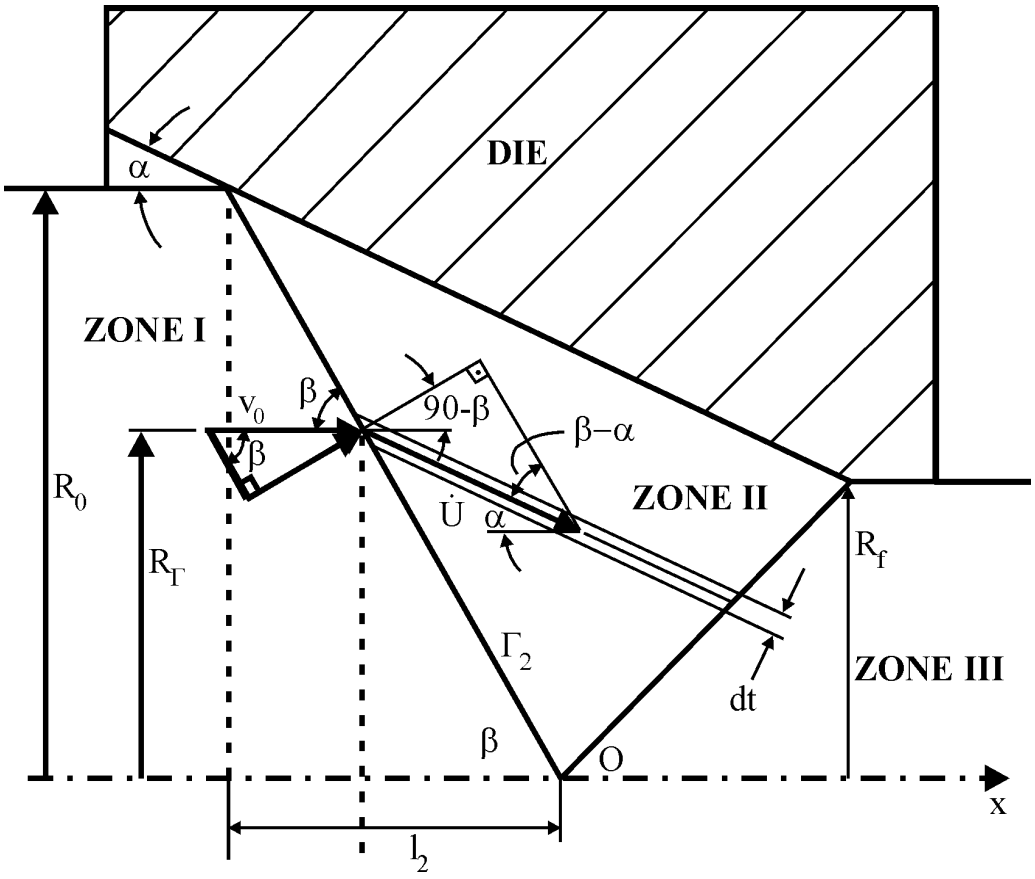

Figure 4.2 Triangular velocity field model [20]

Equation (4.3) reduces to:

$$R_{\Gamma} = \frac{R + X\tan\alpha}{1 - (\tan\alpha / \tan\beta)} \tag{4.5}$$

The continuity at surface Γ_2 implies that the normal components of the velocity v_0 in zone I and $\dot{U}_{\Gamma}$ in zone II should be equal.

$$\dot{U}_{\Gamma} = v_0 \frac{\sin\beta}{\sin(\beta - \alpha)} \tag{4.6}$$

In zone II it is assumed that the material flow in a small channel of thickness *dt.* Volume constancy in the channel:

$$\dot{V} = 2\pi R_\Gamma t \dot{U}_\Gamma = 2\pi R_\Gamma t \dot{U}_\Gamma \tag{4.7}$$

$$\dot{U} = \frac{R_\Gamma \dot{U}_\Gamma}{R} \tag{4.8}$$

Putting $\dot{U}_\Gamma$ from Equation (4.6) and R_Γ from Equation (4.5) into Equation (4.8) leads to:

$$\dot{U} = v_0 \frac{\sin\beta}{\sin(\beta-\alpha)} \frac{1+(X/R)\tan\alpha}{1-(\tan\alpha/\tan\beta)} \tag{4.9}$$

With the help of the trigonometry Equation (4.9) reduces to:

$$\dot{U} = \frac{v_0}{\cos\alpha} \frac{1+(X/R)\tan\alpha}{[1-(\tan\alpha/\tan\beta)^2]} \tag{4.10}$$

From Figure (4.1) trigonometric relation of the triangle gives

$$\frac{R_0 - R_\gamma}{R_0} = \frac{\tan\alpha}{\tan\beta} \tag{4.11}$$

Then Equation (4.10) becomes:

$$\dot{U} = \frac{v_0}{\cos\alpha}(1+\frac{X}{R}\tan\alpha)(\frac{R_0}{R_\gamma})^2 \tag{4.12}$$

Resolving the velocity $\dot{U}_\Gamma$ into its components

$$v_R = -\dot{U}\sin\alpha \text{ and } v_X = \dot{U}\cos\alpha \tag{4.13}$$

Velocity field is determined and the velocity parallel to the die surface has the following components

$$\left.\begin{aligned} v_R &= -K\tan\alpha\left(1+\frac{x}{R}\tan\alpha\right), \\ v_x &= K(1+\frac{x}{R}\tan\alpha), \\ v_\theta &= 0 \end{aligned}\right\} \tag{4.14}$$

The constant K is obtained calculating the volumetric flow through the section at *x=0,* where $v_x = K$, and equating it either with $v_0 R_0^2$ (the inflow) or $v_f R_f^2$ (the outflow). R_f and R_o are final and the initial radii respectively.

$$K = V_0 \cdot (\frac{R_0}{R_f})^2 = V_f \cdot (\frac{R_f}{R_0})^2 \tag{4.15}$$

4.2.1.2 Total Power

The extrusion force, in any solution, is built up from three components. The internal power of deformation, power loss at velocity discontinuities and the power needed to compensate friction losses. At small die angles friction is the dominant but as the angle increases, friction force drops drastically. But at the same time power loss at the velocity discontinuities increase. Each of these powers should be determined independently.

The internal power calculated as follows:

$$\dot{W}_i = \frac{2}{\sqrt{3}} \cdot \sigma_o \cdot \int_V \sqrt{\frac{1}{2} \cdot \dot{\varepsilon}_{ij} \cdot \dot{\varepsilon}_{ij}} \cdot dV \tag{4.16}$$

The strain values for the axis-symmetric extrusion process are:

$$\left.\begin{aligned} \dot{\varepsilon}_{RR} &= \frac{K \dot{g} \dot{x} \dot{g} \tan^2 \alpha}{R^2}, \\ \dot{\varepsilon}_{\theta\theta} &= -\frac{K \dot{g} \tan^2 \alpha}{R} \dot{g} (1 + \frac{x}{R} \tan \alpha), \\ \dot{\varepsilon}_{XX} &= \frac{K \dot{g} \tan \alpha}{R} \end{aligned}\right\} \tag{4.17}$$

$\dot{\varepsilon}_{RR}$, $\dot{\varepsilon}_{\theta\theta}$ and $\dot{\varepsilon}_{xx}$ are calculated in Equation (4.17). All the shear strain components except $\dot{\varepsilon}_{xR}$ are zero.

$$\dot{\varepsilon}_{XR} = \frac{1}{2}(\frac{\partial v_R}{\partial x} + \frac{\partial v_x}{\partial R}) = -\frac{1}{2} K \frac{\tan \alpha}{R} (\tan \alpha + \frac{x}{R}) \tag{4.18}$$

Substitution of the Equations (4.17) and (4.18) into the square root in equation (4.16) results in

$$\sqrt{\frac{1}{2} \cdot \dot{\varepsilon}_{ij} \cdot \dot{\varepsilon}_{ij}} = \frac{1}{2} K \tan \alpha \frac{1}{R} \sqrt{\left[C(\frac{x}{R})^2 + B \frac{x}{R} + A \right]} \tag{4.19}$$

Where *A, B* and *C* are constants and they are equal to

$$A = 4 + \tan^2 \alpha, \quad B = 6 \tan \alpha, \quad A = 1 + 4 \tan^2 \alpha \tag{4.20}$$

The volume element in zone II is $2\pi R dx dR$. So the expression for $\dot{W}_i$ becomes

$$\dot{W}_i = \frac{2\pi}{\sqrt{3}} \sigma_0 \dot{g} K \dot{g} (h_1 + h_2) \tag{4.21}$$

Where h_1 and h_2 are respectively.

$$h_1 = \int_0^{R_f} \int_{x_e}^{x_a} \sqrt{\left[C(\frac{x}{R})^2 + B \frac{x}{R} + A \right]} dx dR \tag{4.22}$$

$$h_2 = \int_{R_f}^{R_0} \int_{x_e}^{x_c} \sqrt{\left[C(\frac{x}{R})^2 + B\frac{x}{R} + A \right]} dx dR$$

The values of x_e, x_a, x_c can be obtained from geometry. Along Γ_2 surface $x_e = -R\cot\beta_2$, $x_a = R\cot\beta_1$ and along Γ_3 $x_a = (R_\gamma - R)\cot\alpha$. Also $\frac{x}{R}$ is substituted with η in the integrals. Then the integrals become

$$\begin{aligned} h_1 &= \int_0^{R_f} \int_{-\cot\beta_2}^{\cot\beta_1} \sqrt{\left[C\eta^2 + B\eta + A \right]} d\eta R dR \\ h_2 &= \int_{R_f}^{R_0} \int_{-\cot\beta_2}^{\eta_c(R)} \sqrt{\left[C\eta^2 + B\eta + A \right]} d\eta R dR \end{aligned} \tag{4.23}$$

Where $\eta_c = \left[\left(R_\gamma / R \right) - 1 \right] \cot\alpha$. The integration of the h_1 results in

$$h_1 = \frac{1}{2} R_f^2 \int_{-\cot\beta_2}^{\cot\beta_1} \sqrt{\left[C\eta^2 + B\eta + A \right]} d\eta \tag{4.24}$$

Converting RdR to $d(\frac{1}{2}R^2)$, the outer integral of h_2 can be integrated easily using the integration by parts technique

$$\begin{aligned} h_2 &= \left[\frac{1}{2} R^2 \int_{-\cot\beta_2}^{\eta_c(R)} \sqrt{\left[C\eta^2 + B\eta + A \right]} d\eta \right]_{R_f}^{R_0} \\ &\quad - \int_{R_f}^{R_0} \frac{1}{2} R^2 \sqrt{(C\eta_c^2 + B\eta_c + A)} \left(\frac{d\eta_c}{dR} \right) dR \end{aligned}$$

$$\begin{aligned} h_2 &= \frac{1}{2} R_0^2 \int_{-\cot\beta_2}^{\left[(R_\gamma / R_0) - 1 \right] \cot\alpha} \sqrt{(C\eta^2 + B\eta + A)} d\eta \\ &\quad - \frac{1}{2} R_f^2 \int_{-\cot\beta_2}^{\left[(R_\gamma / R_f) - 1 \right] \cot\alpha} \sqrt{(C\eta^2 + B\eta + A)} d\eta \\ &\quad + \frac{1}{2} R_\gamma \cot\alpha \int_{R_f}^{R_0} \sqrt{\left[C\left(\frac{R_\gamma}{R} - 1 \right)^2 \cot^2\alpha + B\left(\frac{R_\gamma}{R} - 1 \right) \cot\alpha + A \right]} dR \end{aligned} \tag{4.25}$$

Also

$$\left[\left(R_\gamma / R_0\right)-1\right]\cot\alpha = \cot\beta_1$$
$$\left[\left(R_f / R_0\right)-1\right]\cot\alpha = -\cot\beta_2 \tag{4.26}$$

Making simplifications found in Equation (4.23) to Equation (4.22). h_1+h_2 reduces to

$$\dot{W}_i = h_1 + h_2 = \frac{\pi}{3}\sigma_0 K R_\gamma^2 \int_{R_f}^{R_0} \sqrt{\left[C\left(\frac{R_\gamma}{R}-1\right)^2 \cot^2\alpha + B\left(\frac{R_\gamma}{R}-1\right)\cot\alpha + A\right]}\,dR \tag{4.27}$$

And let $\xi = (R/R_d)$, where $R_d = R_\gamma \cos^2\alpha$ to be substituted as the integration variable. Substituting this variable along with A, B and C results in

$$\dot{W}_i = h_1 + h_2 = \frac{\pi}{\sqrt{3}}\sigma_0 K R_\gamma^2 \cot\alpha \int_{(R_f/R_d)}^{(R_0/R_d)} \frac{1}{\xi}\sqrt{\left[4\tan^2\alpha + (1-\xi)^2\right]}\,d\xi \tag{4.28}$$

Finally,

$$F_\alpha(Z) = \int_1^Z \frac{1}{\xi}\sqrt{\left[4\tan^2\alpha + (1-\xi)^2\right]}\,d\xi = \sqrt{\left[4\tan^2\alpha + (1-Z)^2\right]} - 2\tan\alpha$$
$$+arcsh\left(\frac{1-Z}{2\tan\alpha}\right) + \sqrt{\left(4\tan^2\alpha+1\right)}\left[arcsh(2\tan\alpha) - arcsh\left(\frac{4\tan^2\alpha+1-z}{2Z\tan\alpha}\right)\right] \tag{4.29}$$

The internal power is

$$\dot{W}_i = \frac{\pi}{\sqrt{3}}\sigma_0 K R_\gamma^2 \cot\alpha\left[F_\alpha\left(R_0/R_d\right) - F_\alpha\left(R_f/R_d\right)\right] \tag{4.30}$$

All above was for the internal power which was the deformation energy. Now power losses due to the friction (shear) at the velocity discontinuity boundaries Γ_1, Γ_2 and conical die surface will be calculated.

Shear power loss on Γ_1 are

$$\dot{W}_{s1} = \int_{\Gamma_1} \frac{\sigma_0}{\sqrt{3}} |\Delta v| dS \tag{4.31}$$

Where Δv is the velocity discontinuity along Γ_1.

$$(\Delta v_t)_{\Gamma_1} = v_f \cos\beta_1 - v_R \sin\beta_1 - v_x \cos\beta_1 \tag{4.32}$$

Substituting Equations (4.1) and (4.15) in (4.30)

$$(\Delta v_t)_{\Gamma_1} = v_f \cos\beta_1 + v_f \left(1 + \frac{\tan\alpha}{\tan\beta_1}\right)^{-1} \tan\alpha \sin\beta_1 - v_f \cos\beta_1 \left(1 + \frac{\tan\alpha}{\tan\beta_1}\right)^{-1} \tag{4.33}$$

After some simplifications Equation (4.31) would become

$$(\Delta v_t)_{\Gamma_1} = v_f \frac{\sin\alpha}{\sin(\beta_1 + \alpha)} \tag{4.34}$$

The Δv_t is constant on Γ_1 thus the integration gives

$$\dot{W}_{s1} = \frac{\sigma_0}{\sqrt{3}} (\Delta v_t)_{\Gamma_1} \frac{1}{\sin\beta_1} \pi R_f^2 = \frac{\pi}{\sqrt{3}} \sigma_0 v_f R_f^2 \frac{\sin\alpha}{\sin\beta_1 \sin(\beta_1 + \alpha)} \tag{4.35}$$

Similarly the power loss due shear friction on boundary Γ_2

$$\dot{W}_{s2} = \frac{\pi}{\sqrt{3}} \sigma_0 v_0 R_0^2 \frac{\sin\alpha}{\sin\beta_2 \sin(\beta_2 - \alpha)} \tag{4.36}$$

The power loss due to the shear friction on the die surface Γ_3 is

$$\dot{W}_{fD} = \int_{\Gamma_3} \frac{m\sigma_0}{\sqrt{3}} |\Delta v_t| dS \tag{4.37}$$

The $|\Delta v_t|$ is the length of the velocity vector along Γ_3

$$(\Delta v_t) = (v_R^2 + v_x^2)^{1/2} = K \sec\alpha (1 + \frac{x}{R} \tan\alpha) \tag{4.38}$$

On the die surface Γ_3, $x = (R_\gamma - R)\cot\alpha$, $R_d = R_\gamma \cos^2\alpha$ and $dS = 2\pi R \sec^{-1}\alpha dR$. Substitution in Equations (4.37) and the integration from $R = R_f$ to $R = R_0$ results

$$\dot{W}_{fD} = \frac{2\pi m}{\sqrt{3}}\sigma_0 v_0 R_0^2 \left[\left(\frac{R_0}{R_d}\right) - \left(\frac{R_f}{R_d}\right)\right]\cot\alpha \tag{4.39}$$

The power losses associated with the extrusion process is

$$\dot{W}_{ext} = -\pi\sigma_{xf} v_f R_f^2 \tag{4.40}$$

The total power loss in the process is the sum of $\dot{W}_{s1}, \dot{W}_{s2}, \dot{W}_{fD}, \dot{W}_i$ and $\dot{W}_{ext}$. Thus the relative pressure in extrusion (negative) is

$$\frac{\sigma_{xb}}{\sigma_0} = \frac{\sigma_{xf}}{\sigma_0} - \dot{w}_{s1} - \dot{w}_{s2} - \dot{w}_{fD} - \dot{w}_i \tag{4.41}$$

The non-dimensional forms of the power terms obtained by dividing them by $\pi\sigma_0 K R_\gamma^2$. The non-dimensional forms are

$$\begin{aligned} &\dot{w}_{s1} = \frac{1}{\sqrt{3}}\frac{\sin\alpha}{\sin\beta_1 \sin(\beta_1 + \alpha)},\ \dot{w}_{s2} = \frac{1}{\sqrt{3}}\frac{\sin\alpha}{\sin\beta_2 \sin(\beta_2 - \alpha)}, \\ &\dot{w}_{fD} = \frac{2m}{\sqrt{3}}\left(\frac{R_0}{R_d} - \frac{R_f}{R_d}\right)\cot\alpha,\ \dot{w}_i = \frac{1}{\sqrt{3}}\cot\alpha\left[F_\alpha\left(\frac{R_0}{R_d}\right) - F_\alpha\left(\frac{R_0}{R_d}\right)\right] \end{aligned} \tag{4.42}$$

The lower upper bound can be obtained by selecting appropriate R_d value that minimizes the sum of the power terms.

$$\dot{w} = \dot{w}_{s1} + \dot{w}_{s2} + \dot{w}_{fD} + \dot{w}_i \tag{4.43}$$

The positive root of the equation $\partial\dot{w}/\partial R_d$ which will give the lowest value of $\dot{w}$ should be chosen. The resulting equation is as follows

$$0 = \frac{\sqrt{3}R_d}{\cot\alpha}\left(\frac{\partial \dot{w}}{\partial R_d}\right) = \frac{R_f}{R_d} + \frac{R_0}{R_d} - \left(\frac{R_d}{R_f} + \frac{R_d}{R_0}\right)\sec^2\alpha + 2m\left(\frac{R_0}{R_d} - \frac{R_f}{R_d}\right) + \sqrt{\left[4\tan^2\alpha + \left(1 - \frac{R_0}{R_d}\right)^2\right]} - \sqrt{\left[4\tan^2\alpha + \left(1 - \frac{R_f}{R_d}\right)^2\right]} \tag{4.44}$$

The R_d should be found by using iterative methods such as Newton-Raphson method.

$$\phi\left(\frac{R_d}{R_0}\right) = \left(\frac{R_0}{R_d}\right)\left[1 + \frac{R_f}{R_0} + 2m\left(1 - \frac{R_f}{R_0}\right)\right] - \left(\frac{R_d}{R_0}\right)\left(1 + \frac{R_0}{R_f}\right)\sec^2\alpha + \sqrt{\left[4\tan^2\alpha + \left(1 - \frac{R_0}{R_d}\right)^2\right]} - \sqrt{\left[4\tan^2\alpha + \left(1 - \frac{R_f}{R_d}\right)^2\right]} \tag{4.45}$$

And the initial value of R_d should be chosen the root of the Equation (4.45) without the square roots. Then the root can be found easily with the iterative methods.

$$R_d^{(0)} = R_0\sqrt{\left[\left(\frac{R_f}{R_0}\right)\left(1 + 2m\frac{1 - (R_f/R_0)}{1 + (R_f/R_0)}\right)\right]}\cos\alpha \tag{4.46}$$

Then the force can be found by the following equation:

$$F = \frac{\pi R_0^2 \sigma_{xb}}{g} \text{ where } \sigma_{xb} = \sigma_0(w_{s1} + w_{s2} + w_{fD} + w_i) \tag{4.47}$$

4.2.2 Upper-bound solution

Forces countered in the forward extrusion part of the experiments can be calculated using upper-bound method.

The values are as below for the experiments.

$\sigma_0 = 402\text{MPa}$ $R_0 = 15\text{mm}$

$\sigma_{fm} = 640\text{MPa}$ at ε=0.2 $\alpha = 15\,\text{deg}$

$R_f = 10\text{mm}$ $m = 0.1$

For the experiments the R_d value is found by using MathCAD program [Appendix B], which utilizes Newton-Raphson algorithm. Using Equation (4.46) as the initial value R_d is found to be 12 mm. The detailed solution can be found in appendices. The total force required to for the punch is found to be 36 tons, which is computed by using initial flow stress. When the force is calculated by mean flow stress a value of 48 tons. The σ_{fm} is calculated by taking the average of initial flow stress and the flow stress at ε=0.2. The stress values are calculated by taking mean of flow stress at 200 °C and 20 °C of the flow curve of 16MnCr5. The flow curves were obtained at a strain rate of 0.5 s^{-1}.

4.3 Buckling

In a tensile loading fracture occurs when ultimate tensile strength value is reached. But in compressive loading failure may occur before the critical compressive fracture stress value is reached depending on several parameters. The buckling is closely related to the ratio of the total free length to cross-sectional area or diameter. The other parameters are the loading force and the boundary conditions at the ends. Buckling may not be a great problem for structures because a buckled load-carrying element does not lose its ability to carry load because of the post-buckling state shown in Figure (4.2). On the other hand, in metal forming such failures result unacceptable workpieces. Forexample the flange of the workpiece will be eccentric or totally fail due to fractures occurring inside the workpiece. The dies may break which are very expensive to build. So this type of situation must be handed carefully. The buckling behavior may be explained by energy. The material selects the deformation mode that has lowest cost in terms of energy. Generally, this behavior depends neither on the workpiece material nor on

the temperature [4]. In this study it is discovered that this rule is valid if the body temperature is uniform all over the body.

4.3.1 Buckling types

There are several different buckling behaviors of the material depending on the loading nature (e.g impact or static loading), shape of the workpiece (e.g. shell or solid) and some material properties (e.g strain rate sensitivity).

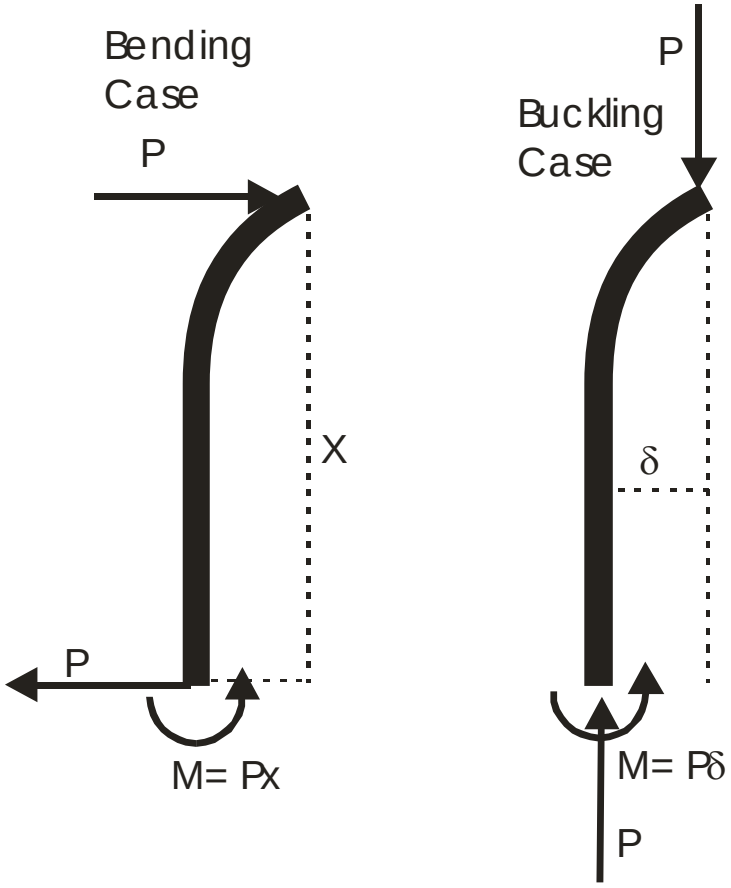

Figure 4.3 Bending and Post-Buckling analogy

Types of buckling:

a- Elastic column buckling

b- Inelastic column buckling

c- Shell buckling

4.3.1.1 Elastic Column buckling

Elastic column buckling is the type buckling occurs generally. The solid structures with excessive length will buckle elastically under loading. As the name implies the buckling itself can be determined by the equations of elasticity starting with Equation (4.47) (Bending moment).

$$M(x) = EI\frac{d\theta}{dx} \tag{4.47}$$

Where $\frac{d\theta}{dx}$ is the curvature and is given by:

$$\frac{d\theta}{dx} = \frac{1}{\cos\theta}\frac{d^2\delta}{ds^2} = \frac{1}{\sqrt{1-\left(\frac{d\delta}{ds}\right)}}\cdot\frac{d^2\delta}{ds^2} \tag{4.48}$$

δ is the finite distance from the neutral axis of the bar.

For moderate angles θ: (via expansion)

$$\left[1+\frac{1}{2}\left(\frac{d\delta}{ds}\right)^2 + H.O.T.\right]\cdot\frac{d^2\delta}{ds^2} + \frac{P\delta}{E\cdot I} = 0 \tag{4.49}$$

Assuming a mode that satisfies the boundary conditions $\delta=q_1.\sin\pi s/l$ and integrating a weighted average of the solution and the ordinary differential equation. This results in Equation (4.23)

$$-q_1\cdot\frac{\pi^2}{2l} - q_1^3\cdot\frac{\pi^4}{16l^3} + q_1\cdot\frac{Pl}{2EI} = 0 \tag{4.50}$$

Solving Equation (4.50) will give:

$$\begin{aligned} q_1 &= 0 \\ q_1 &= 0.903l\cdot\sqrt{\frac{P}{P_{cr}}-1} \end{aligned} \tag{4.51}$$

The q value that is found from Equation (4.51) will be put into $\delta=q_1.\sin\pi s/l$. Then it is easy to find the deflection versus P/P_{cr}.

4.3.1.2 Inelastic Buckling

In plastic zone, Euler's formula is not valid anymore. Inelastic buckling is also the case in impact loading (Figure 4.4). The Euler formula does only considers the elastic modulus of the material and this is insufficient. Several methods can be used to detect plastic buckling. Some methods use tangential elastic modulus in plastic zone. One of the best methods is the finite element method to solve the problem due to its complex nature.

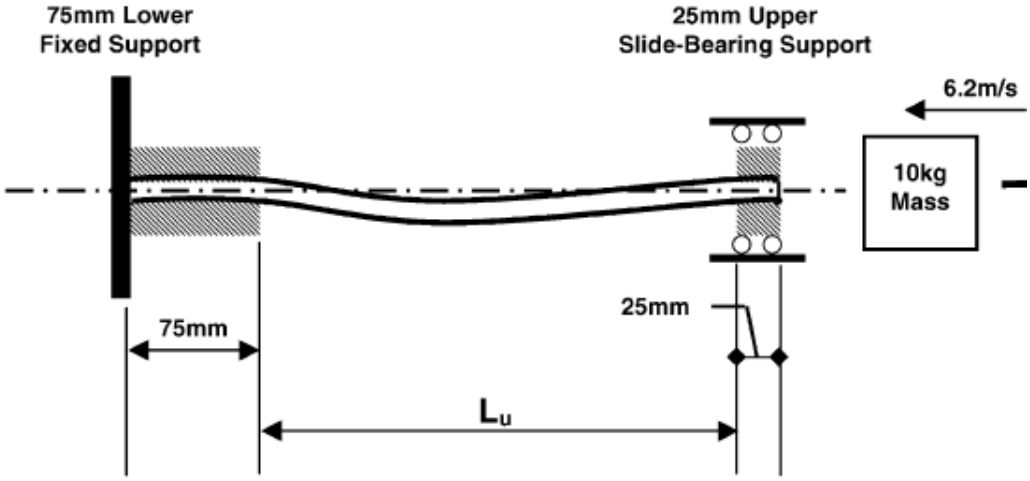

Figure 4.4 Inelastic buckling (impact loading case)

4.4 Conclusion

In this chapter the analytical approach to the simultaneous hot and cold forging process is described. The extrusion part of the problem is solved using upper bound method. The analysis of extrusion part of the problem gave results slightly over the results found from FEA. The FEA results will be explained in Chapter 8. This should be due to low strain rate values caused by slow punch motion. The

flow stress values are taken at a strain rate value of 0.5 s^{-1}. The actual strain rate in the extrusion area is between 0.005-0.05 s^{-1}.

The analytical calculation of the upsetting force by using the upper bound method is difficult and cumbersome. The difficulty comes from the fact that an extreme bulging occurs during upsetting (complex velocity field) and the extreme temperature changes between zones.

Analytical detection of buckling in simultaneous hot and cold forming process is difficult to model. Main reason is the body temperature of the workpiece is changing by time and temperature is not uniform all over the body. This fact changes elastic modulus and tangential elastic modulus in the body from point to point. The best method of buckling detection for this type of process is a 3-D FEA. In a 3-D FEA, boundary and initial condition can vary from point to point.

CHAPTER 5

EXPERIMENTAL STUDY

5.1 Introduction

Analysis world is full of assumptions and engineers cannot solve any problem without assumptions. Any simplification made to solve the problem must be verified. In applying the finite element method, there are several inputs such as boundary conditions, initial conditions, flow curve etc, whose validity should be proved. Even the theory underlying FEM used to solve the problem, the solution may be incorrect. All the reasons above show that every analytical result should be checked by experiments. If the experiments show that the results obtained from analytical methods are wrong, then the whole solution procedure should be repeated with corrections made to the assumptions. This loop continues unless an acceptable error is obtained.

The aims of the experimental study are temperature measurements during and after the heating process, force measurements, shape investigation and metallurgical investigation during and after forming the workpiece.

The temperature measurements were done in order to determine the initial body temperature distribution after the heating process and its variation in time. Force measurements were done in order to observe the validity of our assumptions of FE simulations. Final shape of the product has been investigated to compare it with the FEM output. Finally, the metallurgical investigations have been made to see the final product quality and failures inside the body such as voids appearing during formation.

The next Section 5.2 briefly discusses the equipment used in the experiments. The results of the experiments are discussed in the Sections 5.3 and 5.4.

5.2 Experiment Setup

RUAG Munition Company based in Altdorf / Switzerland supplies the devices used for the experiments. These devices are as follows:

1. Induction Heater
2. Thermocouples
3. Data acquisition system
4. Hydraulic press
5. Dies
6. Lubricants
7. Force Measurement Cell

These device are discussed in the forthcoming subsections

5.2.1 Induction Heater Setup

Induction heating is a special topic and will be briefly explained in this section. Induction heater requires three main subunits. These are:

1- Power Supply
2- Induction Coils
3- Rotor

Power supply unit (Figure 5.1a) is the main component of the heating setup. It supplies high voltages at high resonance levels. The voltage supplied can be varied from 200 ~ 650 Volts with a maximum resonance of 10 kHz. The maximum power output of the machine is 80 kW. The unit was rented from the company Elotherm [Elotherm, 2000]. Induction coils are the replaceable/changeable parts. The geometry of the coils depends on the workpiece geometry and process. There are special coils for different applications (forming, hardening, etc). In the experiments, three different coils were used. They differ only in their axial length and so, there are no geometry differences. The purpose of using different coils is to see the effect of different heated zone lengths.

a) Power Supply Unit

b) Medium sized Induction coil, Rotor and the workpiece

Figure 5.1 Induction Heater

Table 5.1 Induction Coil Sizes

Coil Name (Figure 5.2)	**Axial Length** (Figure 5.2)
Small Coil	45 mm
Medium Coil	96 mm
Large Coil	145 mm

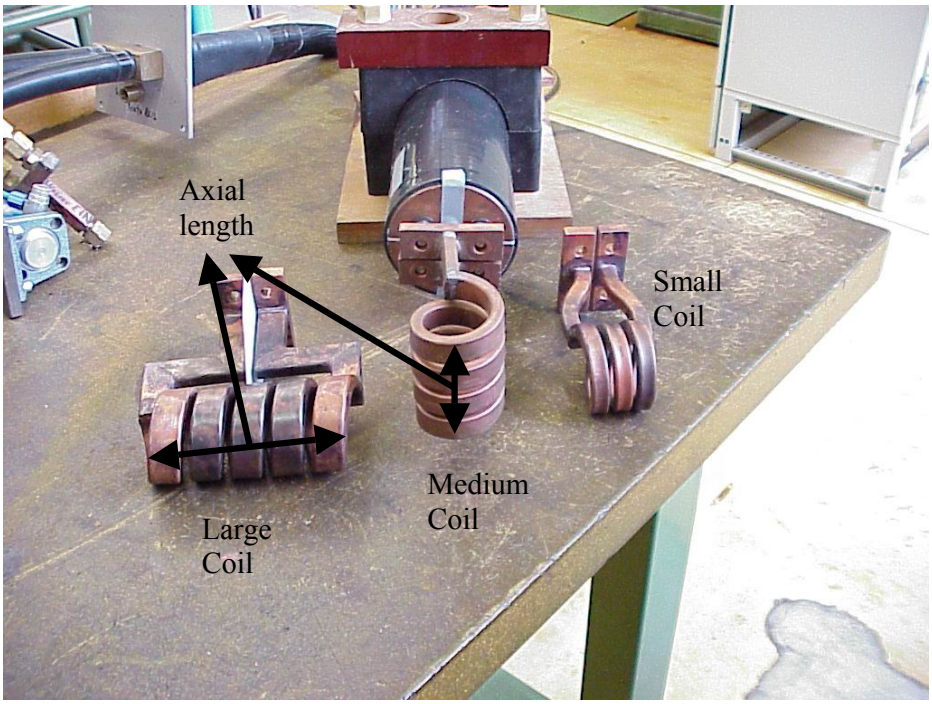

Figure 5.2 Induction coils. Large, medium and small coil (Left to right).

This is only achievable with coils with different axial sizes. In Figure 5.1 b, a medium sized coil (Table 5.1) is mounted on the heater setup. The coils are made from copper because of its high conductivity (low resistance to current flow). The high voltage in the process is dangerous because of any contact between the workpiece and the coil. This can be hazardous to human life. As a caution the coils are coated with silk (Figure 5.1b) and a special resin resistant to heat. The rotor was not a component of the original setup. After the first experiments, the preliminary results showed that without turning the workpiece uniform heating cannot be achieved. The reason of non-uniform heating is the end geometry of the coils. Generally, flat-ended coils are expensive and difficult to produce. The coils used in the experiments had inclined ends (Figure 5.1b). The setup has been modified to include a motor and a workpiece holder. The motor was turning the holder at a rate of about 600 rpm.

5.2.2 Thermocouples

A temperature difference between any two points in a normal metal will result in an electrostatic potential difference (V_1) if no electrical current is allowed to flow between those two points. This potential difference is proportional to the temperature difference T_1-T_2 between those two points. However, the attached voltmeter actually measures the potential drop across all the metal items between its terminals. This includes a strip of metal, and the two wires used to connect it to the voltmeter terminals. To counterbalance the additive potential arising from the connecting wires, a strip of metal dissimilar to the first is attached serially to the first, such that its ends too are between the temperatures T_1 and T_2. This results in a sum of potentials measured by the voltmeter firstly. The potential (V_1) formed in the first metal from the temperatures T_2 to T_1, secondly, the potential (V_2) that arises in the second metal from temperatures T_1 to T_2, (Figure 5.3) Now as long as the two metals are dissimilar, this sum of ($V_1 + V_2$) will not be zero. The potential that is measured is dependent upon the difference in temperatures ($T_1 - T_2$), and not the actual values of T_1 and T_2. Therefore, if one of those temperatures (T_2) can be fixed at a known value, accurate temperature measurements can be made. An easy way to fix the temperature of T_2 is to have it in an ice water bath; as long as ice is present, and in equilibrium with the water, the temperature of the water will be 0 °C. The thermocouple can be leads that are in the ice water bath connected to the Digital Multimeter (DMM) by small wires. The lengths of wire have to be the same. Two kinds of metals should be used in the strip. The reasoning for this is the same as that for the thermocouple being made of dissimilar metals. The potential of the system is the sum of the individual potentials that arise throughout the system. Starting at the DMM, there is the potential V_0 that arises through our first lead, going from room temperature to 0 °C. Then there is the aforementioned, ($V_1 + V_2$) of the thermocouple and finally the potential that arises within the second DMM lead, as it goes from 0 °C to room temperature V_3. If the strips of wire that attach the DMM to the thermocouple are the same, then the potential V_0 cancels out the potential V_3. The DMM then only displays the potential ($V_1 + V_2$), which is what is required to make the temperature measurement.

5.2.3 Data acquisition system

The data acquisition system collects the data from the sensors. In this case sensors are the thermocouples. Data acquisition system reads the voltage difference in the thermocouples and converts the voltage difference to temperature.

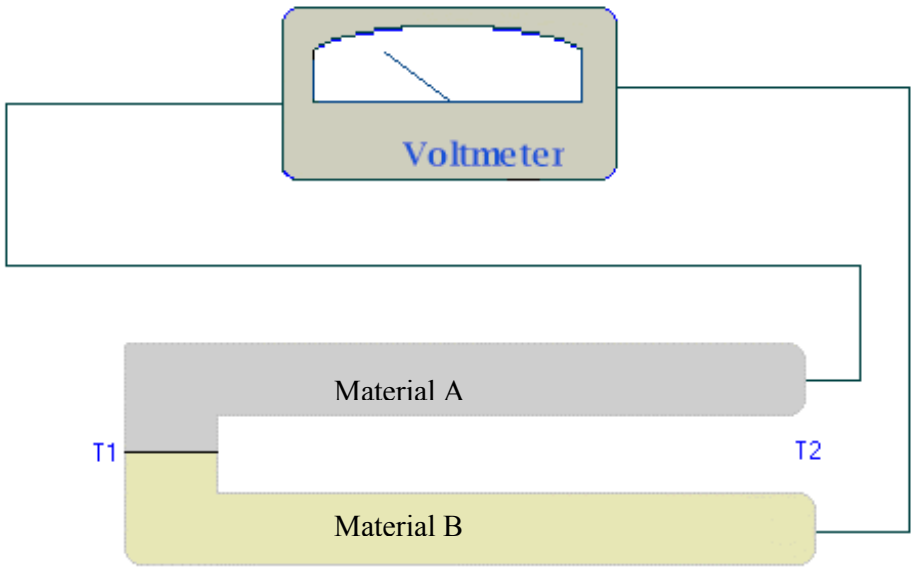

Figure 5.3 Sample Thermocouple

The system used in the experiments supports up to four channels. This means that at the same time four measurements can be taken from four sensors. A special docked laptop station is used in the system. The docking station has the required cards to collect data and the laptop runs a commercial data processing program to process the data received from the channels. The system is a software based data acquisition system. Data sampling rate was not originating from data acquisition card. The computer's clock and processor is used by the program to generate the sampling rate. In the experiments, 100 Hz has been used as sampling rate for temperature measurements.

5.2.4 Hydraulic Press

There are various presses to perform cold forging. The press should be selected for a given application considering the capacity, the power, the stroke length, etc. Mechanical presses provide faster motions and more control over the displacement than hydraulic presses. However, the flexibility of the mechanical presses is limited because their stroke length is fixed at design time. In addition, the force usually varies with the punch displacement in mechanical presses. Hydraulic presses are slower and powerful than its mechanical counterparts. The force does not vary with punch displacement. The stroke length is not fixed at design time. Considering all above facts a hydraulic press was chosen. The hydraulic press used is of Bucher-Guyer type LS 150 (Figure 5.4). Technical data for the press is in given in Table 5.2

5.2.5 Dies

Dies are the most important parts for a metal forming process. Using a die a geometrical shape can be imposed on the workpiece during deformation (closed die forging). Usually dies are harder than the workpiece material and they are produced with higher precision than the normal workpieces. The dies used in the experiments were very simple. Upper die and lower die were the same with small differences. Both contained an extrusion section inside. In Figure 5.5, the sections can be easily seen.

5.2.6 Lubricants

Lubrication is one of the most important issues in forging processes and especially in cold forging. Die life, forming forces and surface quality of the workpiece depends on lubrication.

Figure 5.4 Bucher-Guyer type LS 150 Hydraulic Press

Table 5.2 Press technical data [17]

Total Press Force	150 Tons
Total Displacement	450 mm
Distance Between Upper and Lower Pressing Surfaces	640 – 790 mm. (Adjustable)
Maximum Speed	100 mm/s
Minimum Speed	3.7 mm/s
Maximum Removal Punch Force	10 Tons
Maximum Reverse Direction Force	20 Tons

There are several lubricants available in the market. In the experiments, the lubricant used was GleitMetall-Paste of Techno Service GmbH (Table 5.3). The lubricant itself was not sufficient. Due to the excessive pressure on the surface, it is hard to hold paste on the surface. The surface roughening method chosen is

phosphating. Phosphating forms paste pools on the surfaces that can withstand a higher working pressure than the paste specifications. However, phosphating is an expensive process because of the recycling process after the forming operation. Without proper lubrication, a special defect, which is called cold welding (Figure 5.6), may occur, which depends on the contact pressure between die and the workpiece.

Table 5.3 GleitMetall-Paste of Techno Service GmbH Properties

Maximum Working Pressure	235.4 N/mm^2
Working Temperature Range	-180 ºC to +1450 ºC
Resistive Against	Water, Oil, Benzene

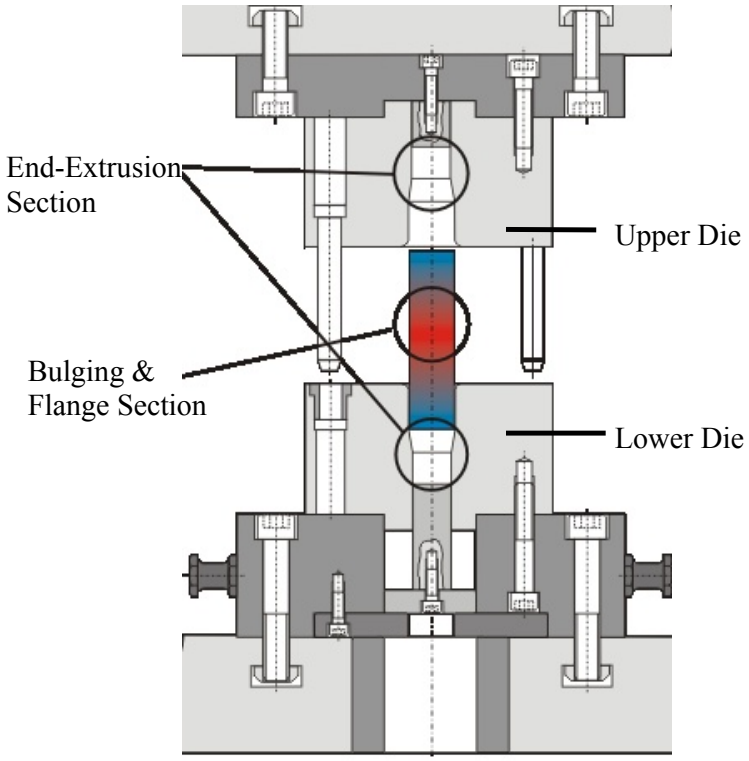

Figure 5.5 Die Setup

5.2.7 Force Measurement Device

Punch force during the experiments is measured with the help of a quartz load washer. Quartz load washers are piezoelectric force transducers, which convert a force in to an electrical charge. In a so-called charge amplifier, this is converted in to a voltage. Due to extremely high resolution of quartz (low voltage differences can be detected), it is possible to measure a change in force in the order of one Newton under a preload of several tons. Such force transducers have an inherently high rigidity and correspondingly high resonant frequency. This allows them to be fitted in measuring objects without altering the elastic behavior of these significantly. The quartz load washer used during the experiments is a KISTLER - 9081A type.

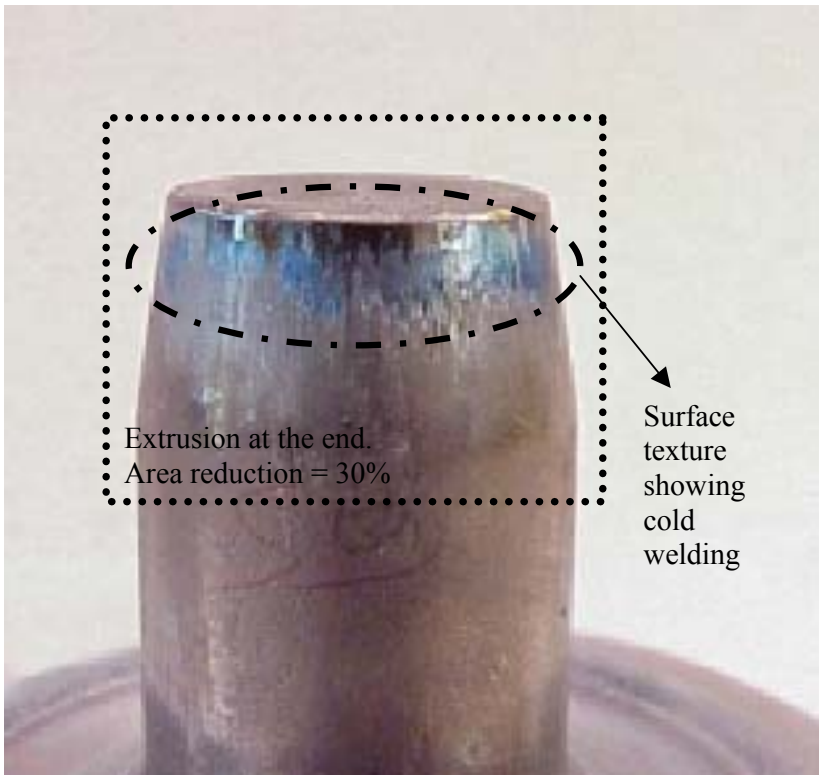

Figure 5.6 Cold welding example

5.3 Heating Experiments

Induction heating is a new topic in metal forming world although it was used for hardening processes for long time. The advantage of induction heating is to heat up a specific area in a short time of about 3 to 6 seconds up to 1000 ºC. The theory behind induction heating is as follows: When a coil through which an alternation current is fed surrounds a steel workpiece, the two are linked by an alternating magnetic field. This field induces an alternating electrical current to flow in the surface of the component. Due to the resistance and magnetic permeability of the steel, rapid heating of the component surface occurs. The intensity of heating is greatest at the surface, and reduces with increase in depth from the surface. This is known as the "skin effect" and the depth of heating decreases as the frequency of the alternating current increases. This effect is advantageous in surface hardening since it helps to confine heating to the surface layers. Heating the inside of the material depends on the equipment specifications such as frequency, voltage, etc.

Experiments were conducted to see the capabilities of the available devices and to take some important data such as temperature profile in the workpieces. This data will be used in finite element models and for tuning the heating devices. The temperature sensors used in the experiments are thermocouples, their properties were discussed in Section 5.2.2. Every experiment was done twice because of the shortcomings in the data acquisition system. The data acquisition was limited by four data channels at a time. In the first experiment temperature distribution data was taken only from the surface of the workpieces parallel to the axis of it (Figure 5.7) at locations 1, 2, 3 and 4. Then with same parameters, the second experiment has been performed but this time radial temperature distribution at the center plane of the workpiece has been measured (Figure 5.7) at locations 4, 5 and 6. Thermocouples are spot-welded to the surface of the workpiece where possible. The other points were contacted by forcing the thermo couples onto the surface. The welding points of the thermocouples have a low location accuracy of about 2-3 mm because of the welding machine used. Temperature readings were taken at room temperature. The different variables used during the tests were voltage, coil size,

frequency of the inductor and amount of time that material heated inside the inductor.

5.3.1 Effect of Voltage

Voltage parameter is important because it is directly related to energy given to the workpiece. Energy is related to the maximum achieved temperature. The range varied was between 210V up to 450V. The machine was capable of giving 650V but this value was not tried regarding the life of thermocouples and their accuracy. The maximum temperature in the heating region increases as the voltage of the inductor increases (Figure 5.8). This behavior was expected. The workpiece used had a 30 mm diameter and 200 mm length. The effect of voltage is not linearly related to maximum temperature achieved in the workpiece (Table 5.4). The values (Table 5.4) are taken at the end of the heating process at the middle (Pos. 4 in Figure 5.7) of the workpiece with the medium coil. As the voltage increases, it is seen that material cannot heat up as much as the voltage increased.

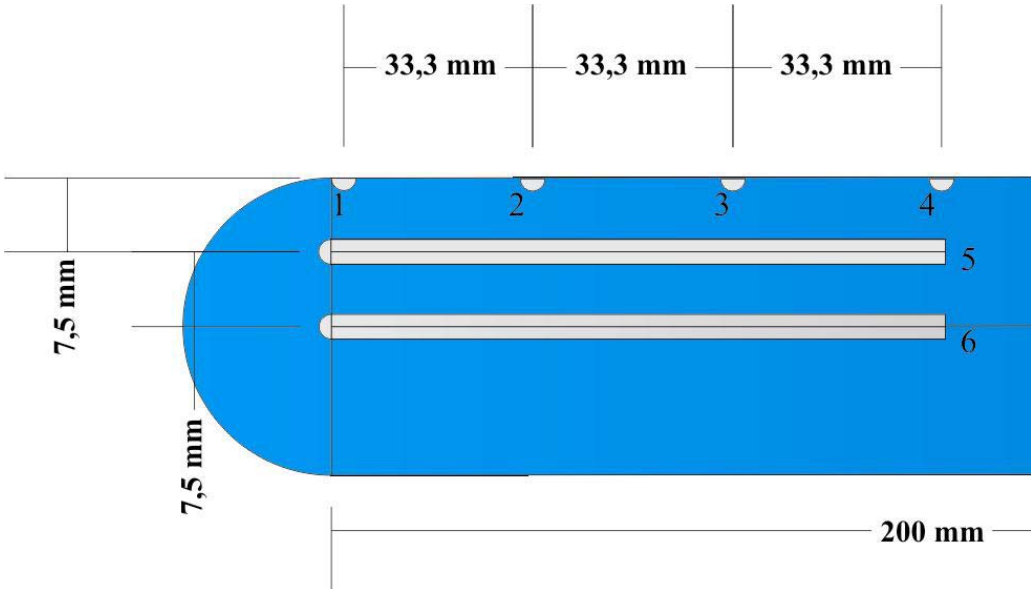

Figure 5.7 Layout of the thermo couples welding points

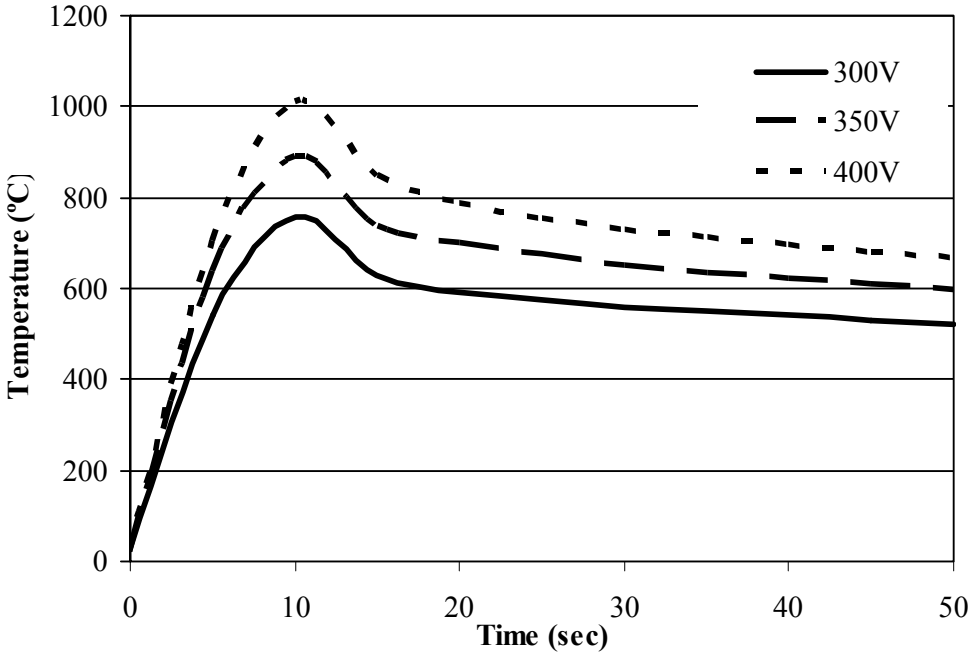

Figure 5.8 Effect of voltage on maximum temperature measured at thermocouple 4. l_0 = 200 mm, d_0 = 30 mm, material: 16MnCr5

Table 5.4 Linearity of voltage vs. maximum temperature (Position 4)

	T_1^{Max} / T_2^{Max}	V_1 / V_2
300V → 350V	1.18	1.17
350V → 450V	1.13	1.29
300V → 450V	1.34	1.50

Table 5.4 shows that if the voltage increased with a ratio 1.3 from 350V → 450V, the maximum temperature ratio is only 1.13. Escalating voltage from 350V to 450V provides an increase of 120 ºC (Figure 5.8). One important problem is that even a high voltage value is used the cooling process is very fast. In five seconds after the heating process is finished, maximum temperature drops about 150 ~ 200 ºC. The energy is spread all over the workpiece body, which causes maximum temperature to drop. The major drawback of this is that workpiece body will have uniform

temperature after some certain time. This is against to this theses starting idea of forming with partial heating process. The idea assumes that one area of the workpiece have a high temperature compared to other areas. The solution to this problem is simple, start the forming process in the quickest possible way.

5.3.2 Effect of Coil Size

In the experiments, three different types of coils were used. Different coils mean different heating volumes (heated zone lengths). Temperature can be changed by changing the amount of energy inputted into unit volume. This is because of the fact that nearly same amount of energy is inputted into the larger material volume thus decreasing the maximum temperature inside the workpiece (Figure 5.9). The problem is solved by increasing the voltage of the inductor, as the coil size gets larger. A large heated volume means a large flange radius at the end of the process and since the aim of the thesis is searching for the limits of the process, this effect should be examined. Coil lengths were 45, 96 and 145 mm respectively. The temperature drop with the coil size length is approximately linear. This shows that with increasing coil length, inductor voltage should be increased proportionally (Section 5.3.1). There are two limits for the size of the induction heating coils:

1-) Workpiece length
2-) Power supply unit capacity

If the coil size is approximately equal to the workpiece first problem is handling and the second problem is the heating of a complete body, which is not desired. The second limit is related with the electronics; for a certain coil size the given power supply unit cannot supply the required voltage at required frequency.

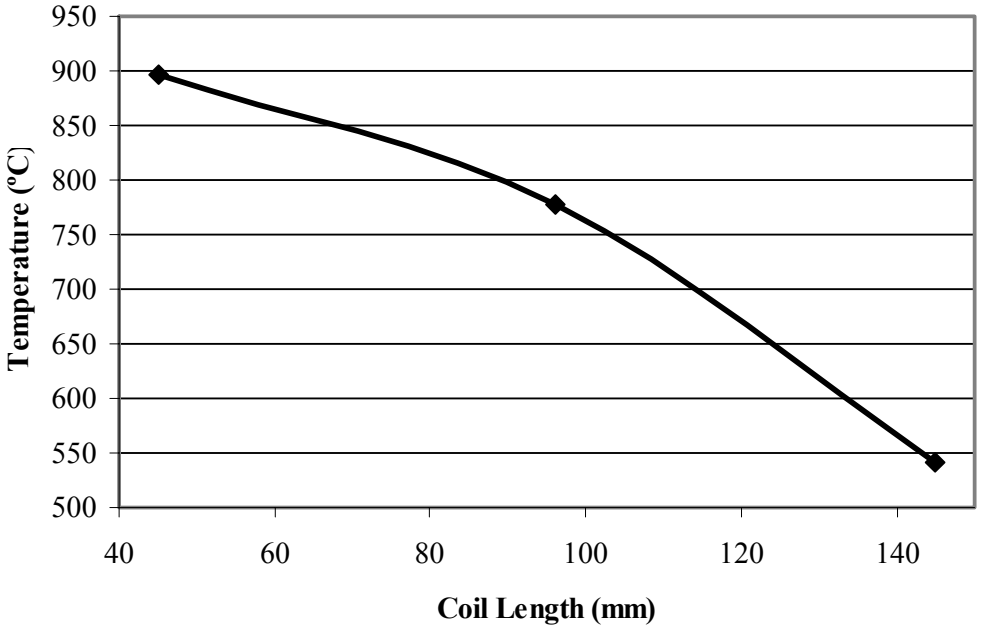

Figure 5.9 Coil Length vs. Max. Surface Temp at 300V
l_0 = 200 mm, d_0 = 30 mm, material: 16MnCr5

5.3.3 Total heating time of the workpiece

Heating time can improve drastically the maximum temperature achieved through out the body. Nevertheless, disadvantage of this variable is the time gets longer heat dissipation inside the body also increases. Power supplier frequency and the heating time are closely related. The operator can change heating time parameter but to change the frequency parameter the service should be called. By increasing the frequency, high temperatures can be achieved in very short periods. That is beneficial to have sharp borders between cold zone and hot zone. The heat cannot flow in a very short period inside the workpiece. For this purpose, extensive experiments and finite element simulations were required in order to find the optimum condition. It can be easily understood from Figure 5.10 that increased heating time increases the temperature at the ends. In Figure 5.10 the end temperature varies 20 degrees from each other. The important point is that Figure 5.10 only shows the temperature profile right after the heating process. The process

requires additional 30 seconds time. This time is used to transfer the workpiece to the press. Using robots can shorten even this time. In this period, end temperatures will rise further.

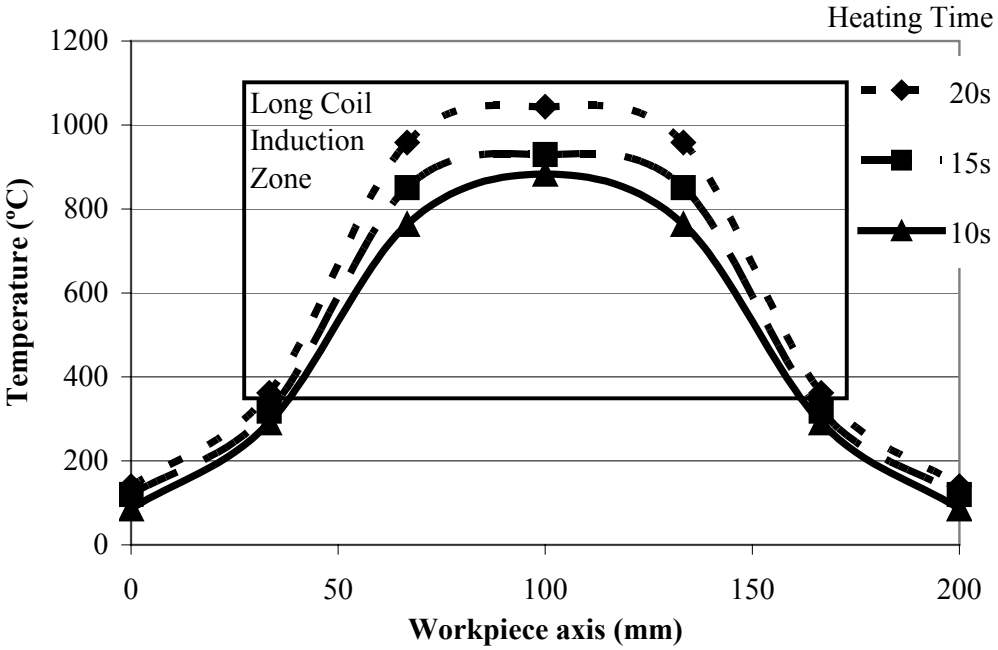

Figure 5.10 Temperature distribution in the body with different heating times
l_0 = 200 mm, d_0 = 30 mm, material: 16MnCr5

5.4 Forming Experiments

These experiments include forming with die. The equipment used in the experiments was explained in detail at the beginning of this chapter. The forming type is open die forging at the middle part of the workpiece. At the closed end of the dies, cold forward rod extrusion is achieved (Figure 5.5) while hot forging is done at the middle of the workpiece. The percent reduction in the extrusion is 11.8%. Both hot and cold forging have been made simultaneously. The main purpose in hot forging section is to form a bulge with the largest possible diameter within the

limits of the process. The main problem in the process is the buckling tendency of the workpiece after a certain critical free length to diameter ratio is exceeded. There are two empiric equations describing the buckling problem, [4]:

$$s = \frac{l_0}{d_0} \leq 2.3 \tag{5.1}$$

$$s = \frac{l_0}{d_0} = 2.3 + d_0 \times 0.01 \leq 3 \tag{5.2}$$

Where s, d_0 and l_0 are slenderness ratio, initial workpiece length and initial workpiece, respectively.

The slenderness ratio s is defined as the ratio of free initial length of the workpiece to initial diameter of it. Both of the equations above are for a body with uniform temperature. In the experiments as explained before partially heated workpieces are used. Therefore these equations are not valid for this case. Thus in the experiments the buckling tendency has been carefully observed. Figure 5.11 shows one type of buckling behavior and its counterpart as obtained by FE simulation.

The parameters controlled in the experiments are:

1. Workpiece body temperature
2. Workpiece length
3. The length of the partially heated zone
4. Material type

In the coming subsections, the effect of these parameters will be discussed.

5.4.1 Effect of Body Temperature on the Process

The temperature effect the process in such a way that it changes the mechanical behavior of the material. As the temperature goes up, the internal energy of the material also increases. This fact enlarges the distance between atoms and the material becomes softer since dislocations can move more easily. This leads to a lower yield strength and ultimate tensile strength.

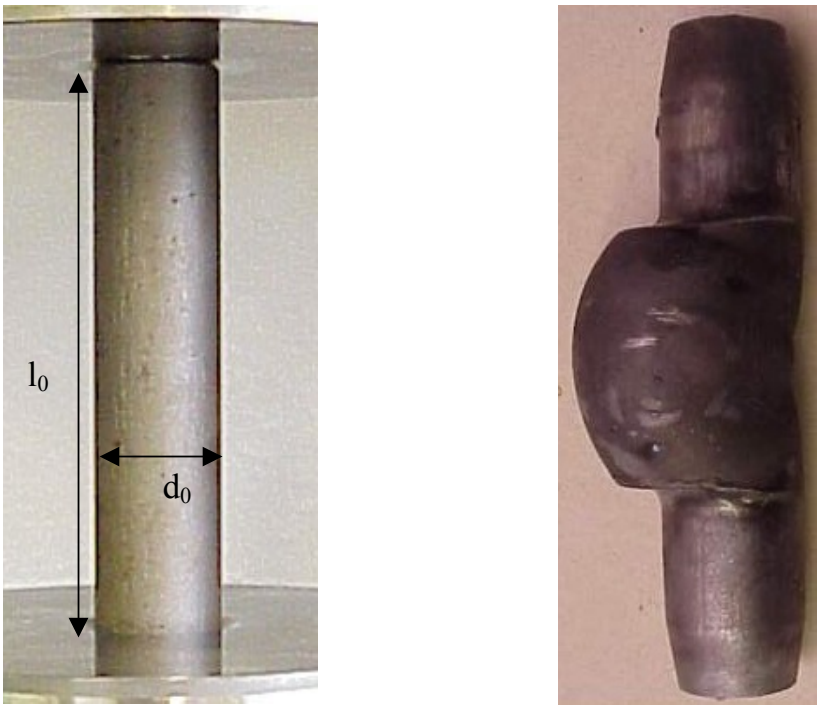

a) **b)**

Figure 5.11 Buckled workpiece.

a) Initial workpiece b) after buckling

Experimental model: 50CrV4, l_0 = 210 mm, Heating voltage: 350 V

There is one advantage of this from metal forming point of view: after some temperature named re-crystallization temperature material does not show any strain hardening. Hardening is the increase of the flow stress after the plastic deformation. This means that the material will not exhibit any deformation history at temperature above re-crystallization temperature. This is good for extreme deformations, which the material does not permit, for instance in cold forming. Because of this fact in the experiment, a temperature above re-crystallization temperature is used. The purpose is to achieve the maximum possible diameter. The deformation degree in the bulge area is above the limits of cold forming. The workpiece in Figure 5.11 has l_0 = 210 mm. This workpiece was heated at 350V. Figure 5.12 shows the initial workpiece and a final workpiece formed a proper flange. Figure 5.12 helps to visualize the extensive deformation in the bulge. T.

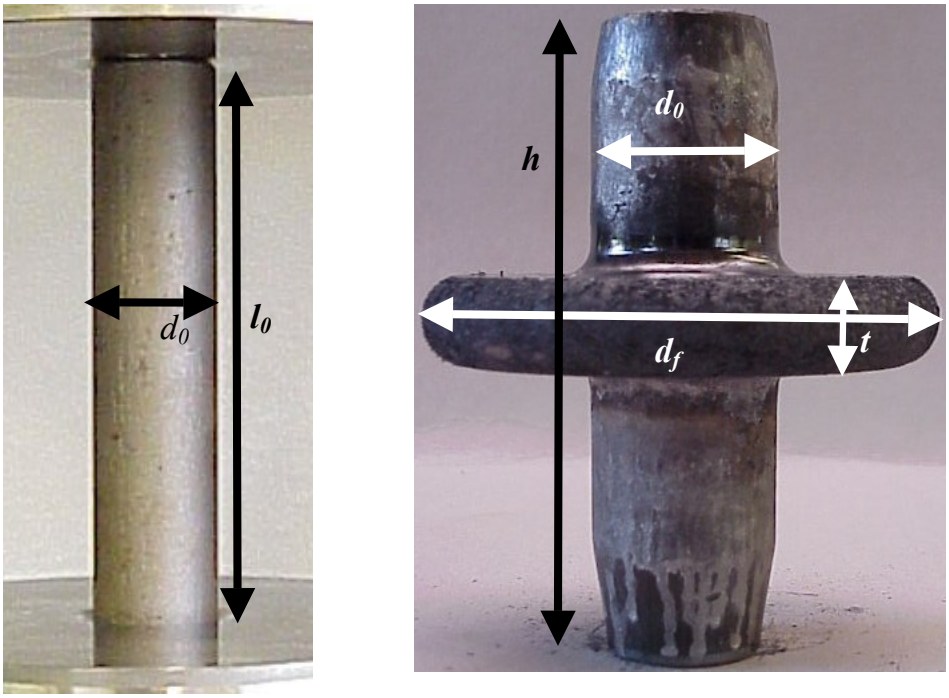

a) **b)**

Figure 5.12 Extensively deformed bulge area

Material**:**16MnCr5, l_0 = 210 mm, Heating voltage: 450 V

d_f=84 mm, t=18.4 mm and h=131.6 mm

The initial slenderness ratio s of the workpieces is below the buckling limit. At the end of the process the flange diameter was about twice of the initial workpiece diameter, which is a good value for cold forming. Then the temperature is increased at the middle zone of the workpiece. The method to heat up the workpiece was described in the previous sections. It is seen that as the average temperature of the flange zone increases, the final flange diameter is also increased (Figure 5.13). The average temperature of the flange zone is directly proportional to heating voltage. This is because of the high formability of the material at high temperatures as described above. The ratio of flange diameter to initial diameter increases as the heating voltage increases. It makes an extremum when heating voltage is about 450V (Figure 5.13). This data is for a workpiece with a length of 168 mm and 30

mm diameter. This fact leads to a conclusion that high temperatures are better for the process to form a big flange. However, increasing the temperature at the flange has an effect on the cooling rate. This is an important parameter because of the cracks introduced by rapid cooling. Generally, forming dies are at a much lower temperature than the flange zone. When they come into contact, the flange cannot withstand a high cooling rate and it is simply cracks.

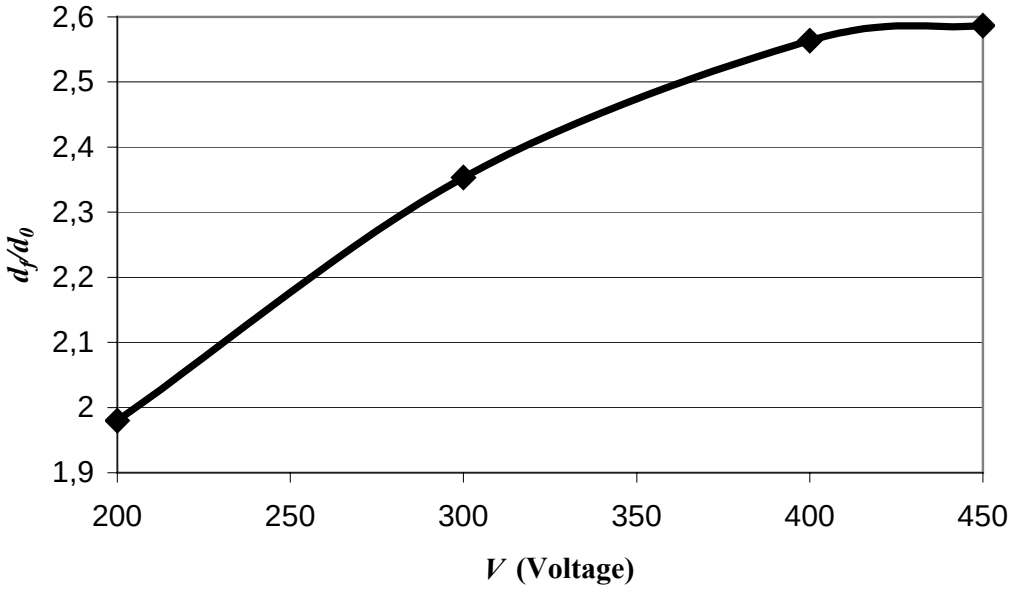

Figure 5.13 Effect of Heating Voltage on Final Flange Diameter over Initial workpiece Diameter

This cracking can be severe (Figure 5.14). The solution for this type of cracking is to reduce the contact time between workpiece and the die. So that the workpiece flange temperature will not drop dramatically causing cracks. Reducing contact time is possible by using a press with a higher velocity at the expense of maximum force because of the increased strain rates.

5.4.2 Effect of Workpiece Length on the Process

The workpiece lengths used in the experiments varied from 120 mm up to 330 mm. Buckling behavior can be detected by using Eqns. (5.1) or (5.2) if the workpiece is

at uniform temperature. For a body with uniform temperature this ratio should be below the value calculated from Equations (5.1) or (5.2). The high temperature zone at the middle of the workpiece changes the buckling behavior of the workpiece. Heating the middle of the workpiece divides the workpiece into three zones (Cold area, hot area and again cold area). Thus, the workpiece is behaving as three different workpieces glued to each other. Therefore, it is possible to form a workpiece that is longer than the limits stated in the Eqns. (5.1) and (5.2) (Figure 5.16). Slenderness ratios (*s*) up to 4.3 are investigated and as the ratio *s* increases, the final flange diameter to initial workpiece diameter is increased. This is due to increased volume available for the flange zone and undergoing excessive deformation. It is seen that after a critical *s* ratio of 3, some defects can be seen in the workpiece. These are, for example necking of the flange because of excessive bulging and some kind of buckling. The necking of the flange is also seen in the finite element simulations. When there is excessive material in the bulge area the bulge starts necking and this neck will not disappear in the final product (Figure 5.17). The products with acceptable quality are obtained up to *s* ratio of 3. Depending on the temperature and other variables maximum flange diameter is about 2.6 times the initial diameter of the workpiece. Another failure type is the internal defect. These defects are critical because they cannot be detected by classical inspection methods. The defective product will have a low fatigue life, (Figure 5.14).

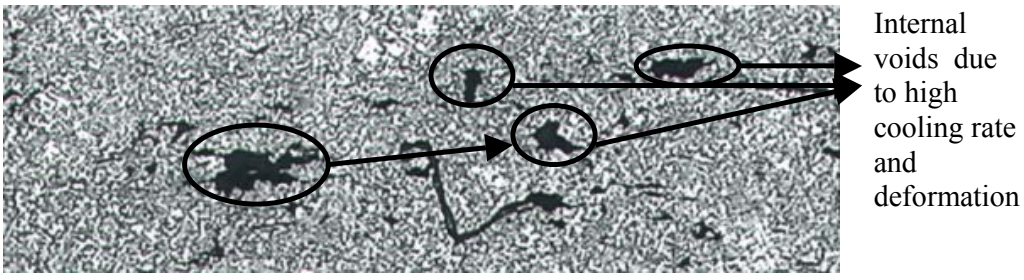

Figure 5.14 Internal defects occurred by excessive deformation (50X Microstructure film at the flange center)

Figure 5.15 Severe cracks in the flange

5.4.3 Effect of Heated Zone Length on the Flange Formation

As discussed previously, three different coils are used in the experiments. The heated zone length can be simply changed by only changing the coil. This parameter shows a similar behavior as the parameter workpiece length. The difference is that at the same workpiece length a thinner but a larger flange is obtained.

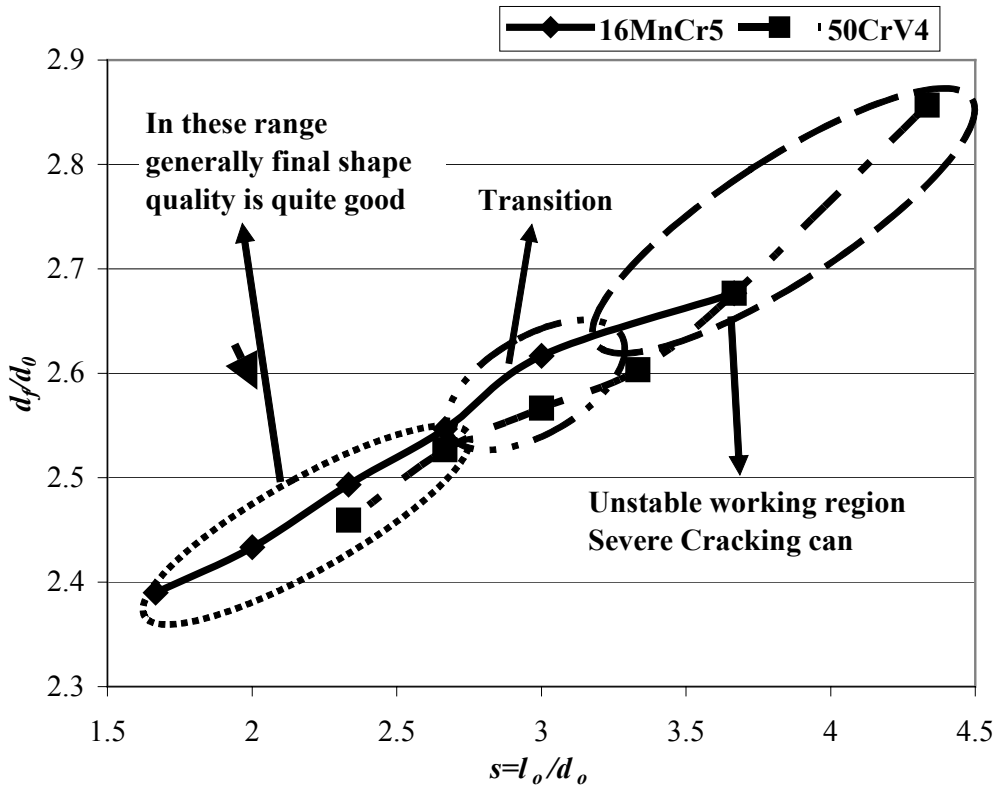

Figure 5.16 Buckling behaviors for partially heated workpieces.

Increasing heated zone length increases the percent volume of the material with temperature over the re-crystallization temperature. Thus it is easier to form a flange. In Figure 5.18, the graph of final flange diameter vs. coil length graph is almost linear. Only an irregular point occurred with material 16MnCr5. This is because the cold extrusion at the ends of the workpiece is not completed. Thus, this causes a bigger volume for flange and a larger final flange radius (Figure 5.18). The important point here is that as the heated zone length increases, this zone tends to be more sensitive to some parameters like unsymmetrical heating and circularity of the workpiece geometry. These cause more deformation to one side of the workpiece thus causing a cam like shape. It can be called as plastic buckling because it is somewhat different from elastic buckling (Figure 5.19).

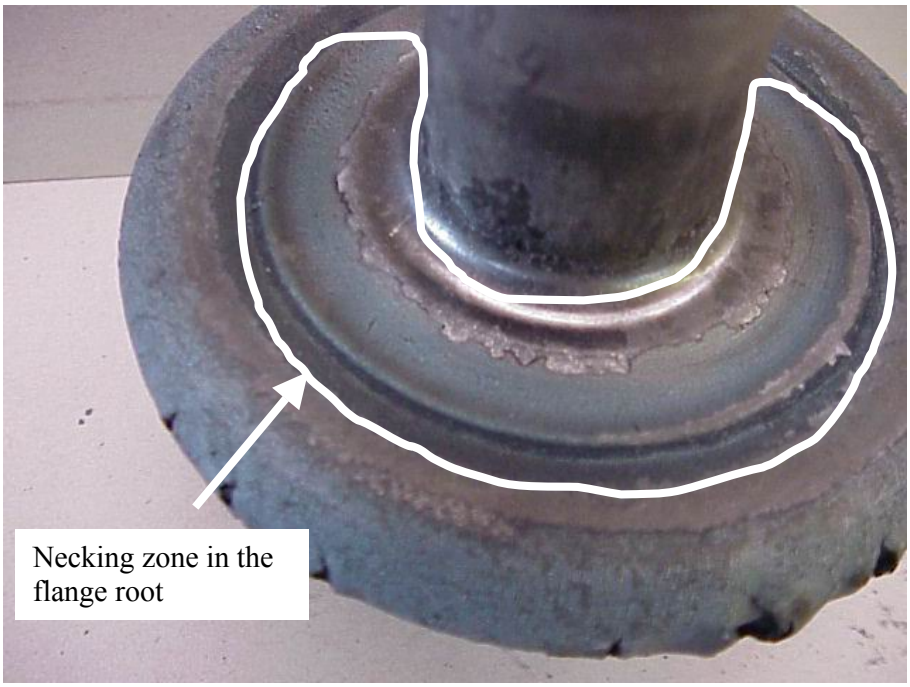

Figure 5.17 Unfilled flange area

In plastic buckling the material buckles during the process plastically forming irregular shapes while elastic buckling is buckling of a column under excessive loading and it is instantaneous. If the final shape for the cam can be calculated this process can be beneficial to produce camshafts over the classical methods. First, all the disturbances, for example unsymmetrical heating, circularity and unsymmetrical cooling, affecting this kind of failure must be identified and suitable mechanism to control these parameters should be developed. The unsymmetrical heating is avoided by using a simple turning table underneath the workpiece. The unsymmetrical cooling can be avoided by making production in environment where the air is still. Circularity tolerance of the stock workpiece should assured by the producer of the stock workpiece.

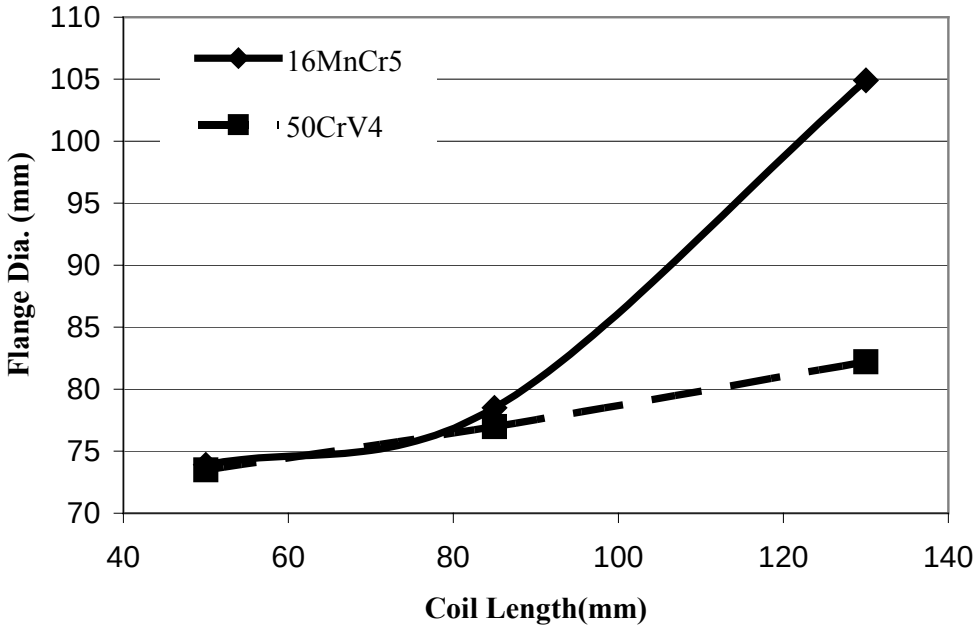

Figure 5.18 Effect of coil length on flange diameter

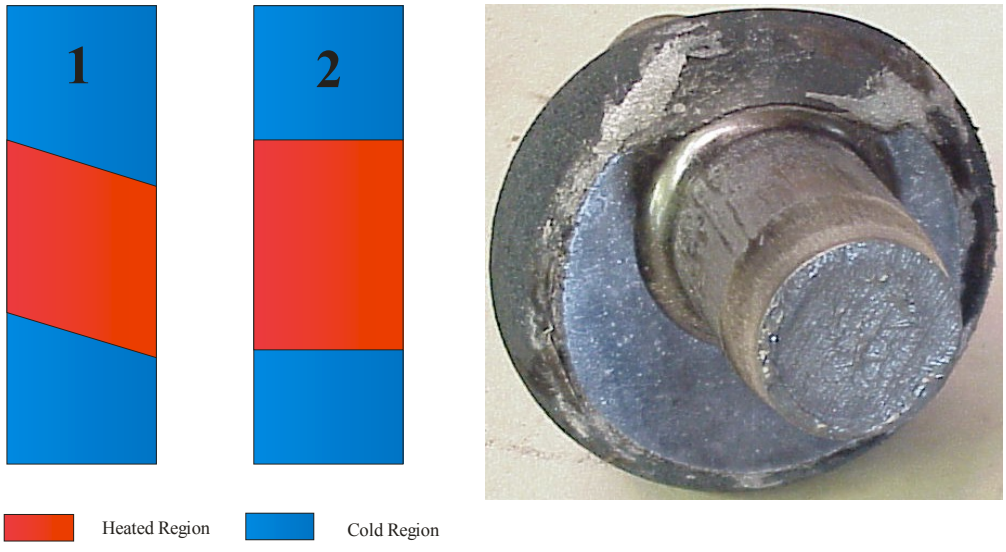

Figure 5.19 Unsymmetrical heating effect.

5.4.4 Effect of Material on the process

Material type influences the metal forming process. Changing the flow curve changes the response of the material for a given strain. One other effect is that different materials have different melting temperatures. This leads to a conclusion that same temperature profiles on different material will behave differently. All above reasons require testing of different materials under same conditions. Figure 5.20 shows that the force displacement curve for 16MnCr5 is slightly lower than 50CrV4. They have approximately 10 tons difference (Figure 5.20). The material type also affects the final product shape. The same punch force with material 16MnCr5 produce a thinner flange. One other fact is one material have more tendency to have an eccentric flange (Figure 5.22). 50CrV4 material has more cracks produced than 16MnCr5. But this behavior may be because of their response to cooling are different. This will be explained in detail in chapter 6 metallurgical investigations.

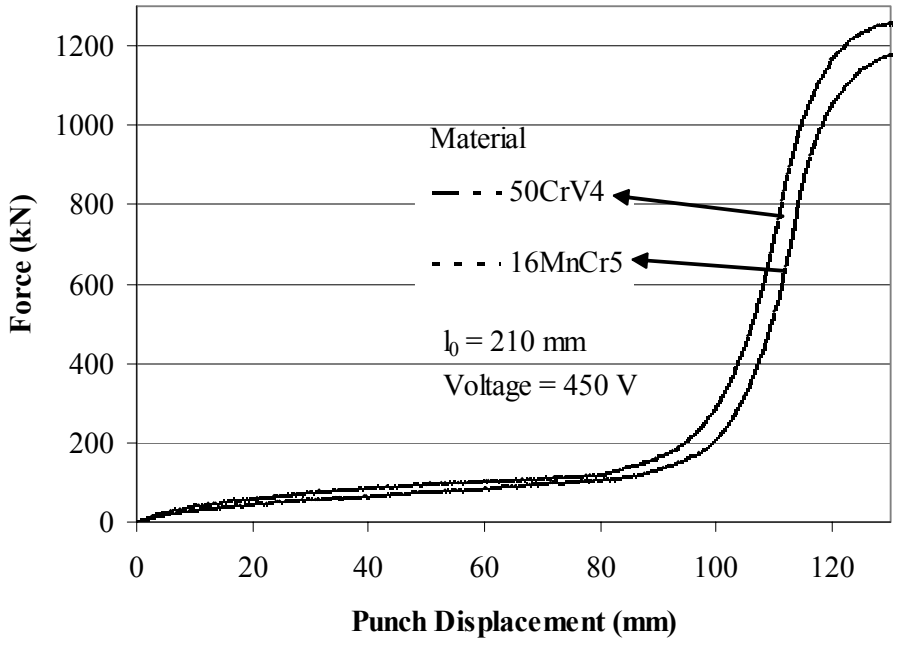

Figure 5.20 Force Displacement curves of the experiments.

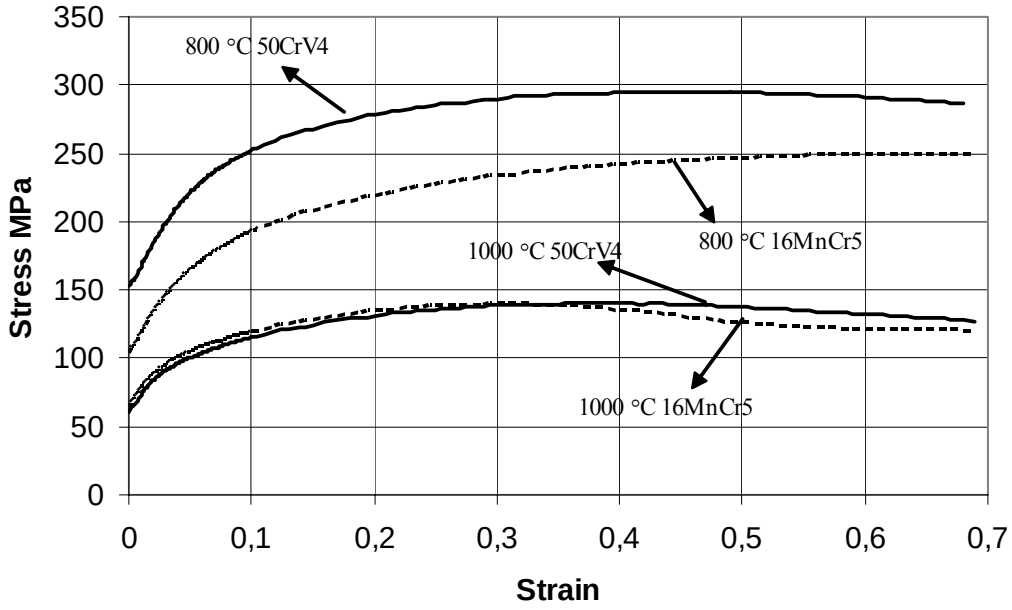

Figure 5.21 Flow curves of 16MnCr5 and 50CrV4 at strain rate 2.

The flow curves of the two materials shown in Figure 5.21. According to the figure 50CrV4 has higher stress values at the same strain compared to 16MnCr5. This means that 50CrV4 requires more force to form than 16MnCr5.

5.5 Conclusions

A brief summary of experiments done can be found in Table 5.5. Experiments showed that the simultaneous hot and cold forging is promising. However, the parameters of the process should be carefully analyzed. The forging process in the experiments begins with extrusion at the ends of the workpiece with 30% reduction in area. At the start of the process the force acting on the workpiece increases slightly in extrusion. In extrusion when the punch force reaches a value about 10 tons a bulge will start to form at the middle of the workpiece. This point is the critical because of Euler buckling can occur at this stage.

a) 16MnCr5 **b)** 50CrV4

Figure 5.22 Comparison of two different materials

Euler buckling is the elastic buckling and it will occur instantaneously at the start of the bulge forming. If this type of buckling did not occur then the next possible failure mode is plastic buckling. Plastic buckling occurs slowly like forming of a non-symmetric flange. The initial bulge form without any problem but the bulge will grow non-symmetrically during forming which is the plastic buckling problem. The buckling is affected by several parameters like the initial length over initial diameter, strain rate, temperature etc. The simultaneous hot and cold forging provides a trick to overcome the initial length over initial diameter ratio. In the literature the limit is given as $s = 2$ (slenderness ratio) [4]. The simultaneous hot and cold forging process can form workpieces with $s = 3$.

The results obtained from experiments showed that special shapes can be obtained with this process e.g. special cam shapes. One more benefit of the process is the increased diameter of the flange. The simultaneous hot and cold forging can form a maximum flange radius 2.6 times the initial diameter without any failure in the

workpiece. The cold forging can produce a maximum flange diameter 2 times the initial diameter without failure. The simultaneous hot and cold forging benefits 30% increase in diameter in the process limits of cold forging. Utilizing induction heating with simultaneous hot & cold forging, special shapes can be forged that can not be done with the classical methods.

Table 5.5 Overview of experiments

Voltage (V)	Material	l_0/d_0	d_f/d_0	Coil	Comments
650	16MnCr5	7	2.93	Large	Necking in the flange root, cracks in the flange and non-symmetric flange
650	16MnCr5	7.6	3.17	Large	Necking in the flange root, cracks in the flange and non-symmetric flange
640	16MnCr5	7.3	2.92	Long	Necking in the flange root, cracks in the flange and non-symmetric flange
640	50CrV4	8	3.13	Long	Necking in the flange root, cracks in the flange and non-symmetric flange
640	50CrV4	7.3	3.04	Long	Necking in the flange root, cracks in the flange and non-symmetric flange
640	50CrV4	6.6	2.80	Long	Necking in the flange root and non-symmetric flange
640	16MnCr5	6.6	2.87	Long	Necking in the flange root
540	50CrV4	8.3	3.13	Medium	Necking in the flange root, cracks in the flange and non-symmetric flange
540	50CrV4	7.6	2.95	Medium	Necking in the flange root, cracks in the flange and non-symmetric flange

Table 5.5 Overview of experiments (Contiuned)

540	50CrV4	7	2.92	Medium	Necking in the flange root and cracks in the flange
540	50CrV4	6.3	2.67	Medium	Necking in the flange root
530	16MnCr5	7.3	2.92	Medium	Necking in the flange root, cracks in the flange and non-symmetric flange
530	16MnCr5	6.6	2.78	Medium	Necking in the flange root and cracks in the flange
450	16MnCr5	6.6	2.68	Medium	Cracks in the flange
450	16MnCr5	6	2.62	Medium	Cracks in the flange
450	16MnCr5	5.6	2.55	Medium	Cracks in the flange
450	16MnCr5	5.3	2.49	Medium	Successful
450	16MnCr5	5	2.43	Medium	Successful
450	16MnCr5	4.6	2.40	Medium	Successful
450	16MnCr5	4.3	2.41	Medium	Successful
450	50CrV4	6.6	2.67	Medium	Necking in the flange root, cracks in the flange and non-symmetric flange
450	50CrV4	6.6	2.67	Large	Necking in the flange root and cracks in the flange
450	50CrV4	5	2.41	Medium	Successful
450	50CrV4	4.6	2.38	Medium	Successful
450	50CrV4	4.3	2.38	Medium	Successful
450	50CrV4	5.6	2.59	Medium	Successful
410	16MnCr5	6.6	2.73	Small	Necking in the flange root and cracks in the flange
400	16MnCr5	6.6	2.7	Medium	Necking in the flange root and cracks in the flange
400	16MnCr5	5.6	2.56	Medium	Successful
400	50CrV4	6.6	2.63	Medium	Necking in the flange root, cracks in the flange and non-symmetric flange
400	50CrV4	5.6	2.48	Medium	Successful

Table 5.5 Overview of experiments (Contiuned)

350	16MnCr5	5	2.28	Medium	Successful
350	16MnCr5	4.6	2.22	Medium	Successful
300	16MnCr5	6.6	-	Medium	Euler buckling
300	16MnCr5	5.6	2.35	Medium	Successful
200	16MnCr5	5.6	1.98	Medium	Successful
0	16MnCr5	6.6	-	-	Buckled

CHAPTER 6

METALLURGICAL INVESTIGATIONS

6.1 Introduction

In this chapter, first some fundamental knowledge about hardness tests and microstructure analysis will be given in Section 6.2 and 6.3, respectively, then our own results will be presented is Sections 6.4 and 6.5. Metallurgical investigations are made to find if the final product properties satisfy the requirements. Depending on the application area today, some percent of the production are analyzed. The investigation can be destructive or non-destructive. Destructive tests give more information but after a destructive test, the part cannot be used. Two different methods were used in this work:

1- Hardness test
2- Microstructure analysis

6.2 Hardness Tests

Hardness by definition is the measure of a materials resistance to deformation by surface indentation or by abrasion. The hardness measurement is taken from a small indent or a scratch. In the beginning, hardness tests were based on qualitative

approach rather than quantitative. The scale based on the ability of a hard material to scratch soft material. Mohs scale is built up with this method and in this scale, 1 is the soft end, which is talc. The hard end is 10 that is diamond [7]. Quantitative methods developed than after. A small indenter under controlled load deforms material surface. Indentation depth and size are measured and then related to a hardness number.

Hardness tests are made more frequently than any other mechanical tests [16]:

1- The experimental setup is inexpensive.
2- The test is non-destructive if the hardness is measured only on the surface.
3- Other mechanical properties of the material can be calculated from hardness measurements.

Basic types of hardness tests are[7]:

1- Rockwell hardness tests
2- Brinell hardness tests
3- Vickers hardness tests

6.2.1 Rockwell hardness test

In Rockwell, test hardness value is determined from an indentation produced under a static load. The indenter used is a steel ball or diamond tipped cone. The measurement is done in two steps. In the first step, surface of the material is penetrated with a load of 10 kg [7]. This penetration usually creates an elastic deformation. Finally, a major load is applied to produce a deeper plastic deformation. The Rockwell hardness is then measured from the difference of depth of penetration from the major load and the minor load. In this test there are many combinations of major load and the indenter. There are many scales related with these combinations for different kind of materials. The B and C scales are the most commonly used, B being common for copper, and aluminum and C being common for steels. The notation for Rockwell hardness is for example RC60 (Rockwell hardness of 60 in scale C).

6.2.2 Brinell hardness test

Brinell hardness test is somewhat similar to Rockwell hardness test. Brinell hardness test achieved by pressing a tungsten carbide or hardened ball 1 cm in diameter on to the test surface. The standard load applied can be 500, 1500 or 3000 kg and the load is maintained 10-30 seconds. The indentation area is then calculated by using a special grid or traveling microscope. The Brinell hardness number is calculated by:

$$BHN = \frac{load}{surface\ area\ of\ \ indentation} \tag{6.1}$$

6.2.3 Vickers hardness test

Vickers hardness test use pyramid shaped indenter. The advantage of this indenter is even light load can create deformations and also the increased accuracy in determining the deformed area. Vickers hardness test has superior resolution as compared to hardness test made by spherical indenters. Vickers hardness test is self similar where the hardness is ideally independent of the indentation load and indentation depth[7]. Applied loads are much than for Rockwell and Brinell ranging between 1 and 1000 g.

6.3 Microstructural analysis

Internal structure of the material is important because there can be some internal cracks, voids or unwanted type of structure. The type of internal structure also determines the strength and hardness of the material and deformation behavior. Voids inside the material will affect the strength of the material but mainly voids cause undetermined fracture of the material. The internal structure of the material is affected by the heat transfer rates during forming.

Types of microstructures

1- Pearlite

2- Spheroidite
3- Bainite
4- Martensite

These will be discussed briefly in the following sections

6.3.1 Pearlite

Pearlite is a two phased microstructure and it results from the transformation of austenite of eutectoid composition and consists of alternating layers of α-ferrite and cementite (Fe_3C). For steel compositions having over 6.7 wt% C, the intermediate compound formed is cementite (Fe_3C), similarly steels with 0.022 wt% C, the intermediate compound formed is ferrite (α) and austenite (γ), is a steel phase with 0.76 wt% C. Temperature plays an important role in the rate of the austenite-to-pearlite transformation. The pearlite structure is formed by alternating ferrite (α) and cementite (Fe_3C) lamellae by Equation (6.2). For steel compositions having over 6.7 wt% C, the intermediate compound formed is cementite (Fe_3C), similarly steels with 0.022 wt% C, the intermediate compound formed is ferrite (α).

$$\gamma(0.76wt\%C) \overset{cooling}{\underset{heating}{\rightleftharpoons}} \alpha(0.022wt\%C) + Fe_3C(6.70wt\%C) \tag{6.2}$$

The lamellae structure can be seen in Figure (6.1). The cementite (Fe_3C) phase in the structure is much harder but also more brittle than the ferrite phase (α). Increasing the cementite (Fe_3C) fraction inside the material will result in a harder and a stronger material. At the same time, the ductility and the toughness of the material will be decreased [7]. The layer thicknesses of ferrite and cementite (Fe_3C) phases also affect the mechanical behavior of the workpiece. Fine pearlite is harder and stronger than the coarse pearlite (Figure 6.2). The reason is simple the reinforcement degree in fine pearlite is higher because the boundary area is bigger than that in the coarse pearlite.

6.3.2 Spheroidite

The spheroidite structure is a special structure and it is formed by heating either pearlitic or bainitic microstructures to a temperature below the materials eutectoid temperature. Keeping the temperature constant about 18h – 24h will form a spheroidite structure. The Fe_3C phase appears as sphere like particles embedded in a continuous α phase matrix [7]. The sample microstructure can be seen in Figure 6.3. The spheroidite structure is the softest structure and the most ductile one. In the spheroidite structure there is less area between phases per unit volume. This leads to relatively soft and ductile material. In fact, the weakest and softest steels are those having spheroidite microstructure.

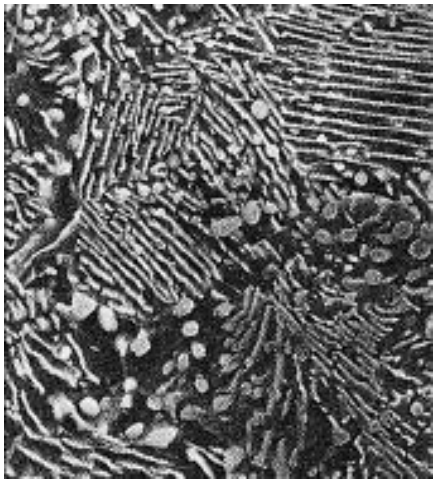

The continuous phase is ferrite (α). The needle like shapes are cementite (Fe_3C) phase.

Figure 6.1 The microstructure of pearlite body formed at 534 °C [13]

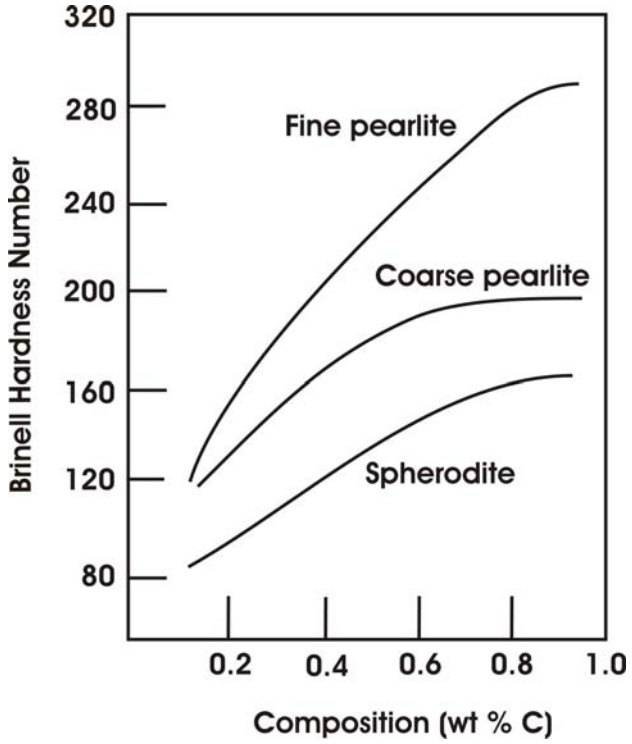

Figure 6.2 Brinell Hardness values of Pearlite and Spherodite [7]

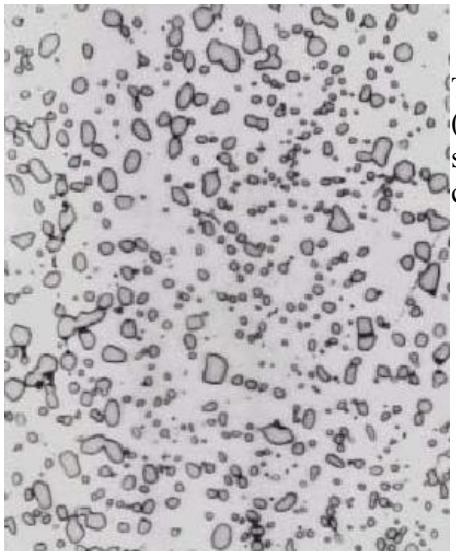

The continuous phase is ferrite (α). The ball shaped structure is spheroidite and its phase is cementite (Fe_3C)

Figure 6.3 The microstructure of spherodite body [7]

6.3.3 Bainite

The microstructure of bainite consists of ferrite and cementite phases, and thus diffusional processes are involved in its formation process. Bainite forms as needles or plates, depending on the temperature of the transformation; the microstructural details are so fine that their resolution is possible only using electron microscopy (Figure 6.4). The phase around needles is martensite, which differentiates bainite from pearlite. The bainite transformation occurs at temperatures below which pearlite forms. Bainitic steels have a finer structure compared to pearlitic structure. Fine structures exhibit a high degree of reinforcement. Generally, bainitic steels stronger and harder than the pearlitic steels. They also show good combination of ductility and strength.

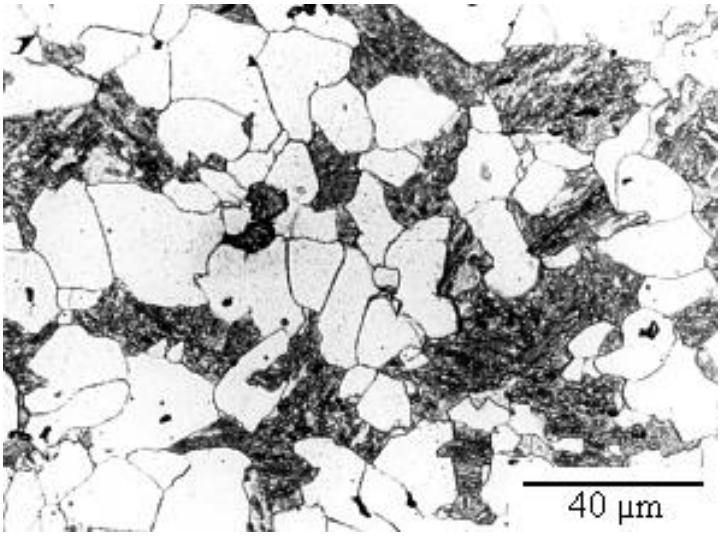

Figure 6.4 The microstructure of bainite body [7].

6.3.4 Martensite

Martensite structure is the hardest, strongest and the most brittle. Rapidly cooling austenized iron-carbon alloys to room temperatures form the martensite structure. Martensite is a nonequilibrium single-phase structure that results from diffusion less transformation of austenite. The hardness of the martensite structure is dependent on carbon content up to 0.6 wt%. Mainly their strength and hardness is related to

interstitial carbon atoms in hindering the dislocation motion and also the few slip systems for BCT structure. The austenite state is denser than the martensite phase. So there is a net volume increase during transformation. This behavior can cause cracks as a result of internal stresses. This behavior becomes important in steels with carbon content greater than 0.5 wt% [7]. The microstructure is like needles that are creating resistance to dislocation motion (Figure 6.5).

Figure 6.5 The microstructure of martensite body [7].

6.4 Results of Microstructure Analysis

First parts that formed properly were etched in order to see the flow lines and microstructure. The etching is done by cutting slices form the workpiece then the slices are furnished. After furnishing the slices, these slices kept in a solution after this process etching process is finished. Also hardness tests are made on some parts. The flange area of the workpiece comes out to be martensite structure showing that we have very high cooling rates in this area (area B) (Figure 6.6). In this area as can be seen from representation on the left hand side (Figure 6.6), the temperatures are as high as 900 ºC. The high cooling rates are because of the interaction between the cold die and the hot material. The dark needles in the microstructure film can identify the martensite structure (Figure 6.6). The martensite structure in these areas also causes some defects as mentioned before the austenite phase is denser than the martensite phase. So there is a net volume increase during transformation which

causes high stresses in the body. This leads to cracking on the flange area. This behavior can be seen in Figure (6.7). There is a sharp boundary between area C and area B (Figure 6.6). The body temperature of the material in area C is at room temperature at the start of the forging while the body temperature of the material in area B is above 800 ºC. In region C (Figure 6.6) we observe bainitic structure, because of few light colored needled like shapes. This structure is favorable because of the good combination of strength and ductility.

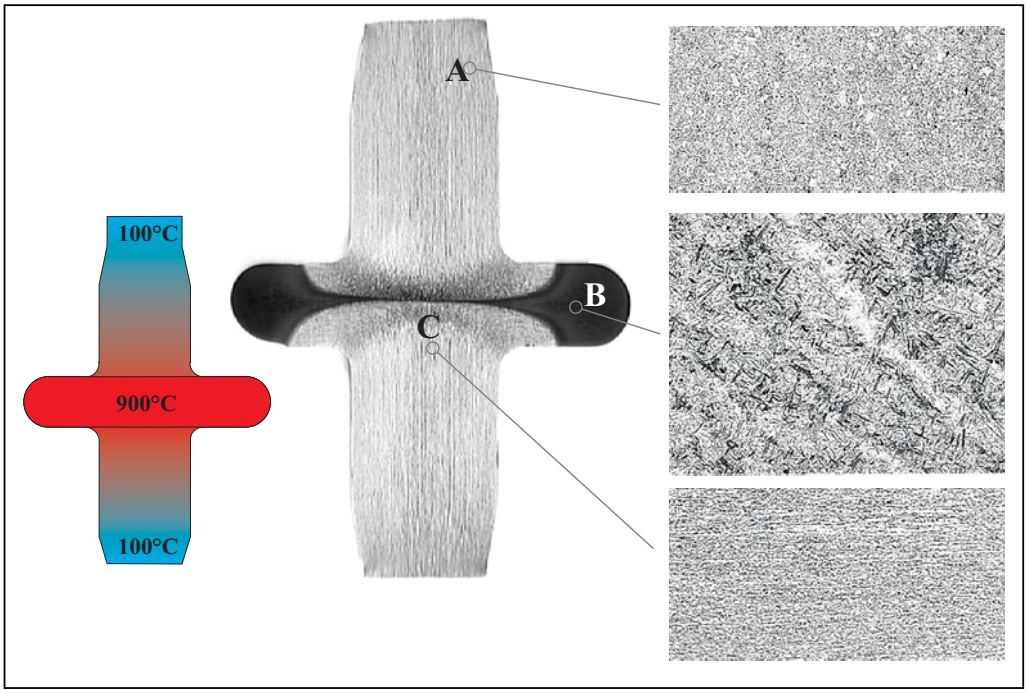

Figure 6.6 Microstructural results of 50CrV4 Steel.
(Left most diagram show the temperature distribution. Middle photo shows the overview of the workpiece. The right most photos show detailed microstructure.)

50CrV4
l_0 = 200 mm
Heating Voltage:
400V

Figure 6.7 Microstructural results of 50CrV4 Stee

The area A is in spherodite or pearlite structure and this area is not affected by the heating or any cooling operation because this area never come close to eutectoid temperatures that is very important for phase transformations. The hardness values can be seen in Figure 6.8.

6.5 Results of Hardness Tests

The hardness values at the edges of the flange are very high due to dominant martensite structure. However, at the center of the flange which is also a transition zone between bainitic and martensite structure the hardness values are nearly half of the hardness values that are on the edges of the flange. As seen in the figure we have relatively hard material in the flange and soft material outside of the flange. The workpiece body has very large range of hardness values, which may be undesirable for some products. The part in Figure 6.8 is heat-treated to homogenize the hardness values and again hardness values were measured. The hardness values of the heat-treated workpiece can be seen in Figure 6.9.

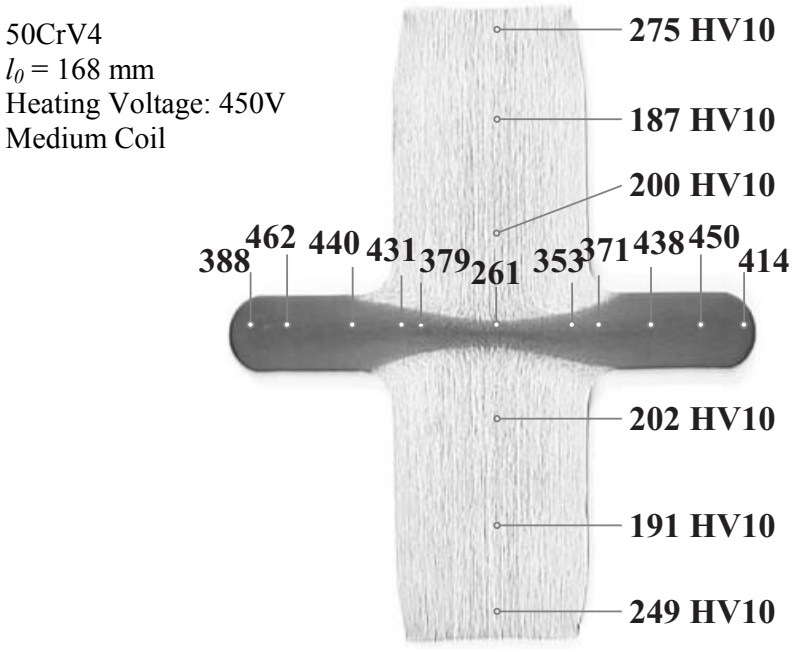

Figure 6.8 Hardness values of 50CrV4 Steel after forming

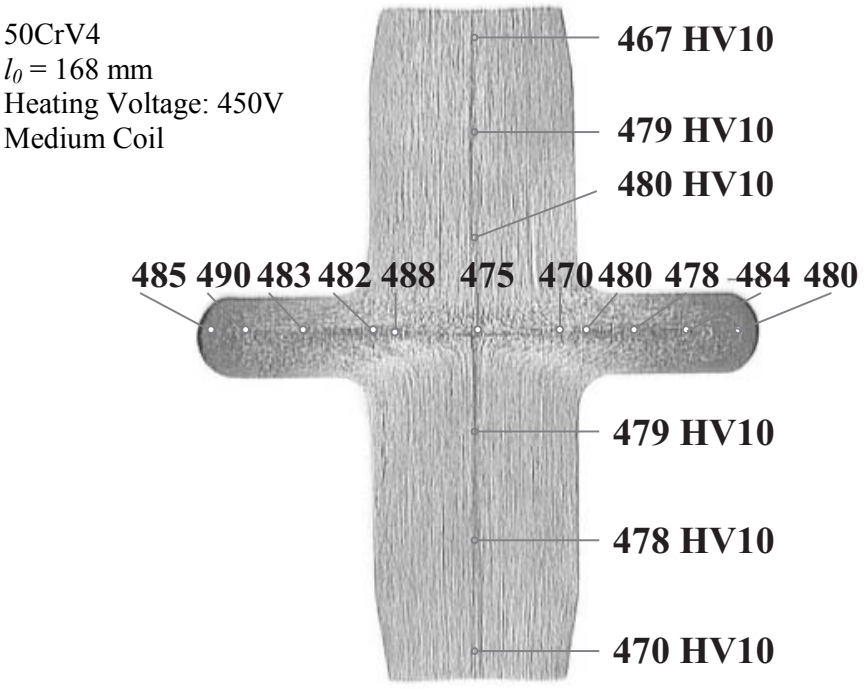

Figure 6.9 Hardness values of 50CrV4 Steel after heat treatment

After heat treatment, the workpiece has uniform and high hardness values. Normally in hot forming low hardness, values are expected but above results show that high hardening values can be obtained with the help of heat treatment

The 16MnCr5 (Figure 6.10) which is a cold forging steel gives a different result. The area C (Figure 6.10) which was very critical for material 50CrV4 is not critical. There is no martensite microstructure inside the flange body. The body of the whole workpiece seems to be in pearlitic structure. Nevertheless, the thickness of the ferrite and the cementite layers is not the same in different areas. As mentioned before layer thickness has important effects on mechanical properties of the workpiece. The flange center has the minimum layer thicknesses. The maximum hardness values are expected in the flange center according to microstructure films. Then the area C (Figure 6.10) should have highest hardness values. Since the workpiece have quite uniform and good microstructure, heat treatment may not be needed unless high hardness values are desired.

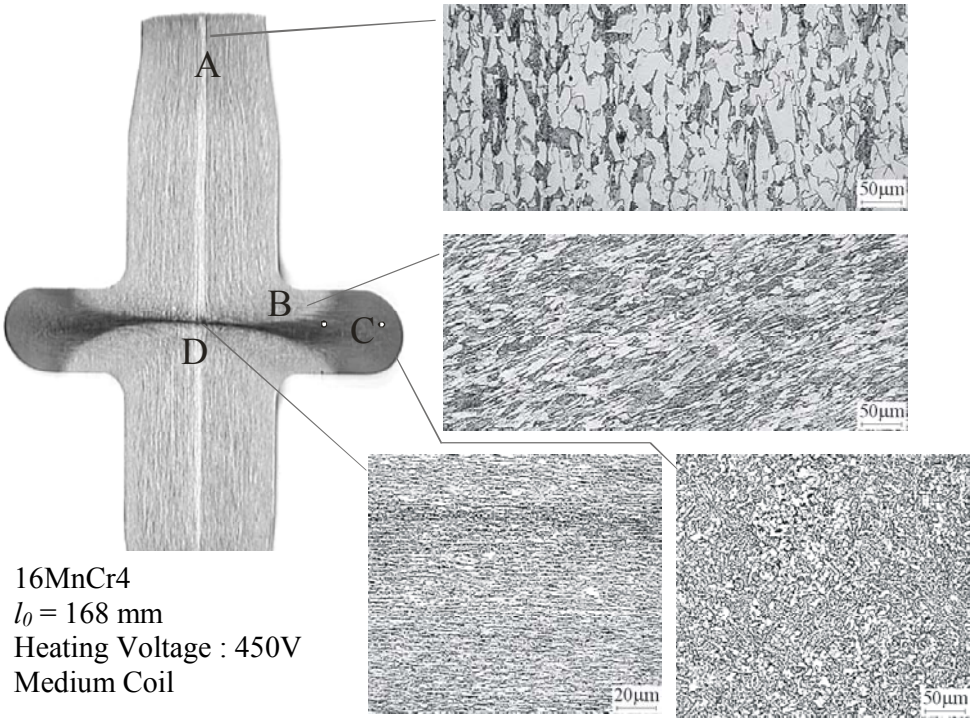

Figure 6.10 Microstructural results of 16MnCr5 Steel

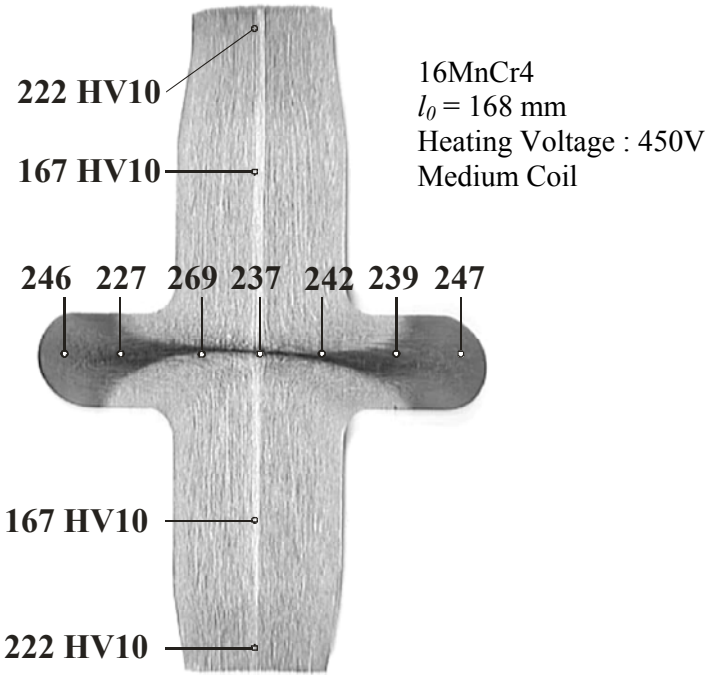

Figure 6.11 Hardness values of 16MnCr5 Steel after forming

The hardness measurements shown in figure 6.11 are satisfying the results of the microstructure films. The highest hardness value is near the center of the flange. The second highest hardness value is at the edge of the flange. In area A again we have strain hardening because of the cold extrusion at the ends like 50CrV4. However, behaviors of the two materials are different from each other. These differences may come from their response to high cooling rates. The idea that 16MnCr4 have withstand higher cooling rates than 50CrV4 steel can be claimed. We can say that 16MnCr4 is better for simultaneous hot and cold forging. One cold forged 16MnCr4 workpiece was also examined. Nevertheless, it was not possible to achieve this high deformability with cold forging. In Figure 6.12 the hardness values of cold forged 16MnCr5 can be seen. The hardness values are similar even they have different forms. The simultaneously hot and cold produced workpiece have nearly the same hardness values with a bigger flange radius. In addition, this method can produce products without any faults if the parameters are correctly set. These parameters are temperature, length, radius and the speed of the die.

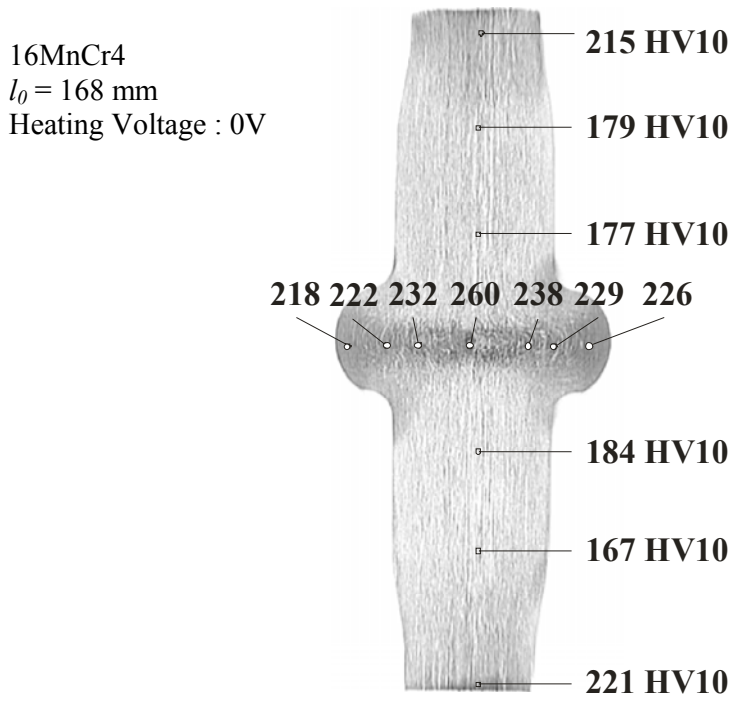

Figure 6.12 Hardness values of 16MnCr5 Steel after forming

6.5 Conclusion

The parts formed with simultaneous hot and cold forming show hardening behavior at the flange area. The measurements showed that the hardness values in the flange zone are as high as 400 HV10. This hardness is comparable to the hardness values that are obtained from cold forging

There is wide range between hardness values in different areas of the workpiece body. This would appropriate for most of the products. If desired heat treatment after forming makes it better. The hardness values after heat treatment are about 470 HV10 and they are uniform all over the workpiece body. The heat treatment also has one more benefit. In the flange region martensite structure can be transformed into other structure like bainite and spherodite so resulting structure will be tougher.

The cooling behavior of the workpieces should be controlled carefully. If the flange is still above re-crystallization temperature after formation of the flange then the

body will still be in austenite phase. At this stage the die temperatures are very important because if the body cools down fast then the structure will change to martensite structure. Martensite structure is less dense then the austenite structure so there will be net volume increase. Depending on the severity of the net volume increase there will be cracks introduced in the body.

If the yield strength distribution is wanted to be found then the Modified Tabor's approach [19] can be used in untransformed material region to predict yield stress values. These values will be compared with the values found from FE simulations. These will included in Chapter 7.

The results show that the workpieces produced with this technique can compete with the products produced with conventional techniques. Hardness values, internal structure and product quality is better than expected. The hot forged regions can form mirror surfaces that can be found in cold forging. The method has the advantages of both cold and hot forming.

CHAPTER 7

FEM ANALYSIS

7.1 Introduction

Finite element analysis is favored today because of the reduced cost of testing and experiments. Finite element method (FEM) provides a systematic way to reduce the number of tests being done to produce a new product. This method is generally very simple with the use of commercial FEM software available. The use of these commercial softwares automate the setup of the experiment in computer environment. However, the user still should do modeling, simplification and input of the data. This fact requires some qualifications of the user. The user should have the basic understanding of FEM. In addition, the user should also know about the parameters that are included in the analysis. The modeling includes the appropriate meshing of the geometry (elements in the mesh must conform to restrictions such as the use of near-square shape elements in 2-D). The simplifications are the boundary conditions and the initial conditions that are idealized but at the same time resemble the real process. The data input is the flow curve of the material, initial temperature or forces acting on the body. If any of these contains errors then the analysis will lead to a wrong solution. The finite element solution procedure for any problem is shown in Figure 7.1. In the following sections, the FEM modeling of the simultaneous hot and cold forging will be described. In addition, the outcome of the results will be discussed such as failure types of the process.

7.2 Modeling

The process was conceptualized as an elasto-plastic, large strain and large displacement problem. The concept also includes heat transfer calculations because of the coupled analysis type. The model was made axisymmetrically at the start because of the cylindrical shape and the cylindrical loading. In an axisymmetric model, a section of the workpiece is picked up and when this slice is rotated 360° then the model will give the original geometry. The advantage of this kind of model over a full 3-D model is the time required to finish the analysis and the robustness in the analysis due to the symmetry boundary conditions.

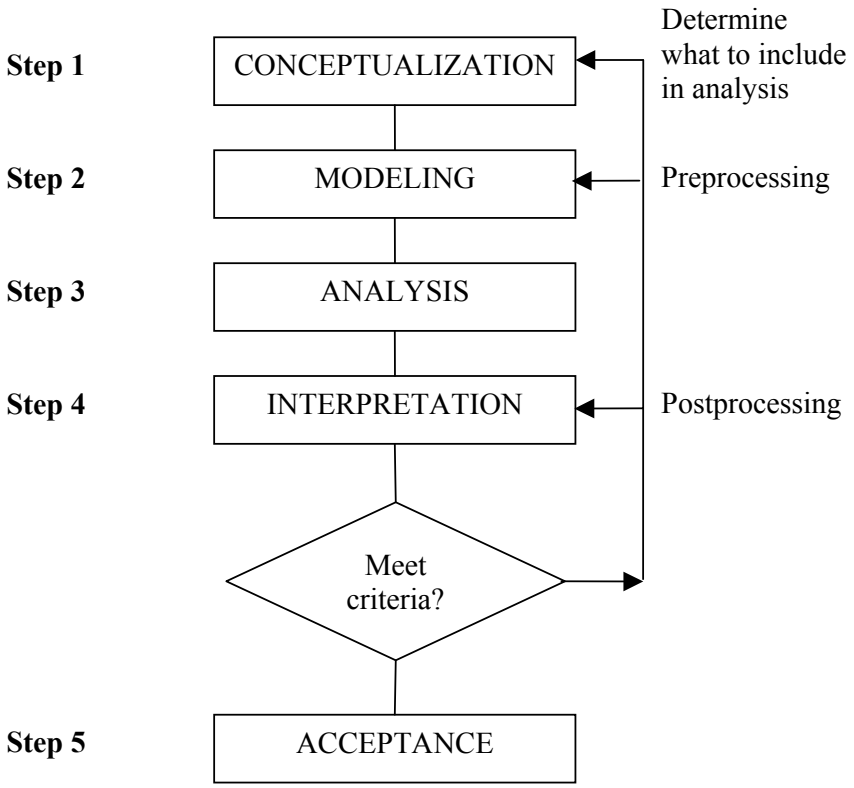

Figure 7.1 Finite Element Analysis Flow Chart [10]

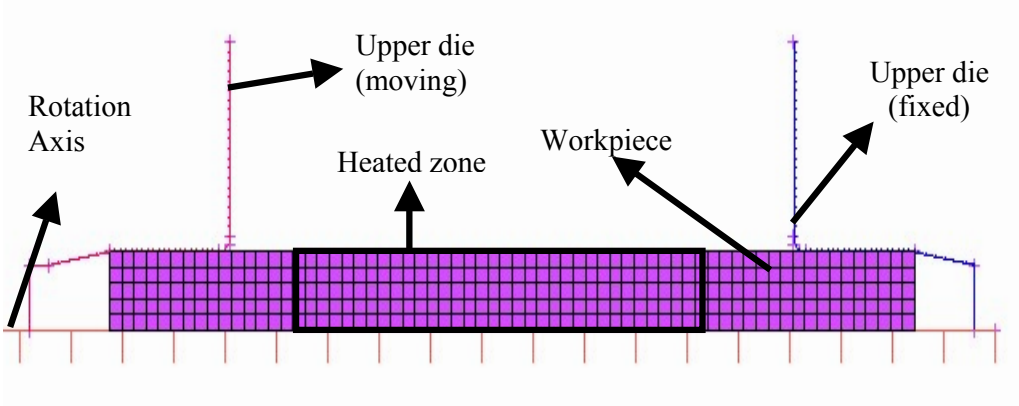

Figure 7.2 Axisymmetric model

On the other hand, axis-symmetric solution has some shortcomings. For example buckling cannot be determined with axis-symmetric modeling (Figure 7.2). The model in Figure 7.2 has to be rotated 360º. This means that any deformation occuring in radial direction represents a deformation occurring at every location with the same radius. But in buckling problem the deformation is influenced in one direction. In a 3-D model, buckling forms can be simulated at the expense of the processing time. In addition, 3-D models are difficult to pre-process.

7.2.1 Geometric modeling (Mesh Generation)

The geometry of the dies is drawn with MENTAT pre-processor. For the 3-D models and 2-D models initial mesh size with the edge length of 2 mm is used. In the 3-D models, one symmetry plane is used. The use of the symmetry planes helped to reduce the amount of processing power required. In Figure 7.3, a 3-D model is seen with one symmetry plane. In addition, the buckling of the workpiece is forced to occur either in direction one or direction two by the use of the symmetry plane. This usage of symmetry plane is appropriate because the model does not lose its ability to buckle. Every symmetry plane helps to reduce number elements by a factor of two. Remeshing is also important for geometric modeling because it does intermediate meshing between steps. The remeshing criteria used for 3-D models overlay hex because it was the only remeshing technique for hexaheadral elements in MSC.Marc. 2-D models are remeshed by using advanced front meshing. This remeshing technique is suggested by MSC.Marc because it gives better results.

7.2.2 Boundary Conditions

The boundary conditions in MSC.Superform (MSC.Autoforge) generally are generated by the use of contact bodies (dies) and the symmetry planes (Figure 7.3). A moving die and a fixed die are used. For 3-D models, symmetry bodies are used to decrease number of elements in the model thus reducing the solution time.

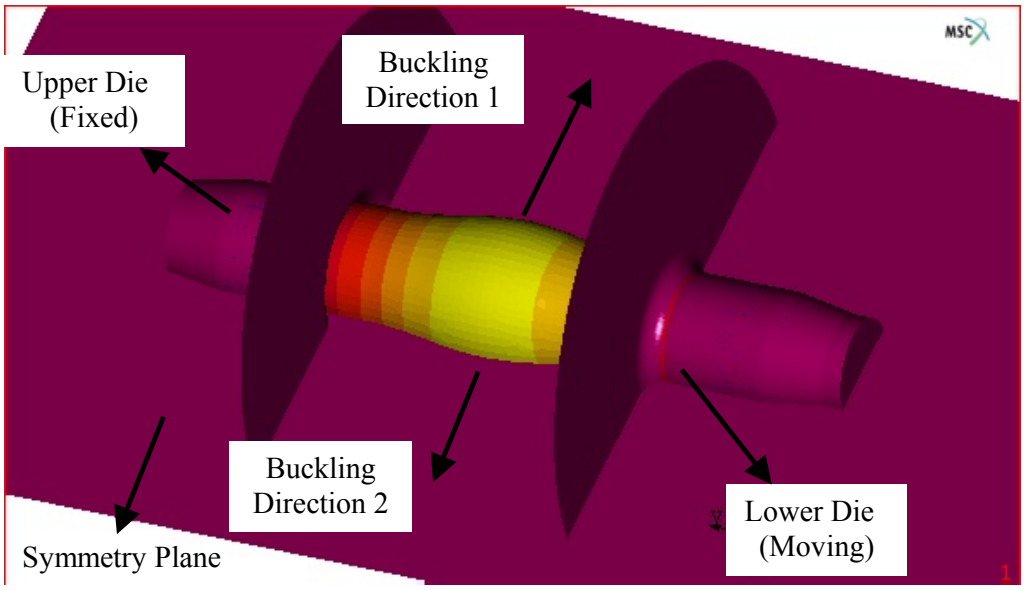

Figure 7.3 3-D model of the experiments

7.2.3 Initial Conditions

The initial conditions for the models are very important due to coupled thermo-mechanical analysis. In the real process, the middle of the workpiece is heated by induction heating to very high temperature just below the materials melting point. The workpiece then have some time before the process starts. This is critical because the heat flows into the cold zone of the workpiece and to the environment. The induction heater also does not heat the volume to a uniform temperature. So to create the effect of both cooling and the non-uniform heating of the induction heater, a prior analysis is made to have the same heating profile as the real one. In this analysis, the workpiece is left to cool after uniform heating of the mid-part. The heat transfer by convection is not easy to compute. Several convection coefficients are used in the analysis in a trial & error method to find right coefficient. So the

convection coefficient is simply guessed. The following temperature profiles are obtained for a 210 mm long workpiece with a heat convection coefficient h = 0.3 W/m²·K. The longitudinal surface temperature profile of the workpiece is shown in Figure 7.4. This resembles the experimentally measured one which will be compared in the forth-coming chapters. The radial temperature profile is shown in Figure 7.5. Both graphs are obtained at the end of the cooling analysis. The initial temperature at the hot zone at the start of the cooling loadcase is set to 1300 ºC and the cold zone is at 25 ºC. The coefficient of conduction is selected from the MSC.Marc material database. The workpiece is allowed to cool down for thirty seconds. At the cold ends, temperature rises above 100 ºC and at the middle temperature drops below 1100 ºC. The total cooling time was about thirty seconds. The result shows that the cold region does heat up to high temperature. Therefore, at the ends of the workpiece, forming is cold forming. This is also the case in the real process.

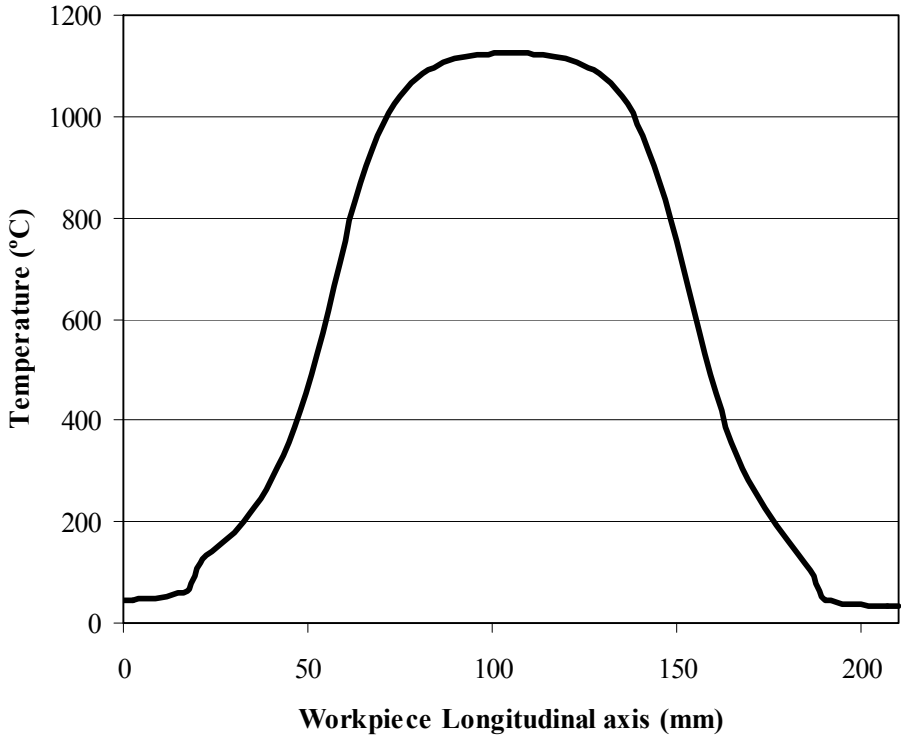

Figure 7.4 The longitudinal surface temperature profile found by FEM. (At end of cooling process)

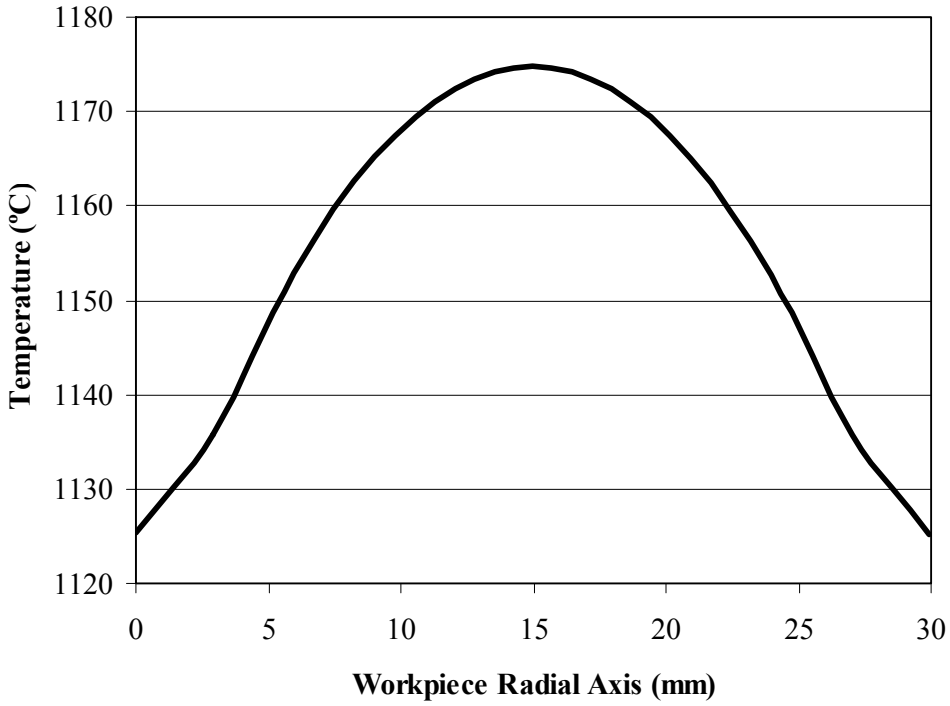

Figure 7.5 The radial internal temperature profile found by FEM. (At end of cooling process)

7.2.4 Materials

The materials used in the simulation are 16MnCr5 and 41Cr4. 41Cr4 material was not used in the experiments. The existing material at RUAG components division was also sent to Zurich University to obtain the real flow curves but the results could not met requirements of the MSC.Marc software. MSC.Marc requires same strain rate values at all temperatures for which the flow curve is measured. In the experiments, the material 50CrV4 was used and the flow curves obtained from Zurich University did not work for MSC.Marc. 41Cr4 was selected because its behavior is nearest to 50CrV4 (Figure 7.24). The material flow curves, conduction coefficients, thermal expansion coefficients, specific heat, Poisson's ratios and mass densities are used from the material of the commercial software database. The two materials have been selected specifically to see the difference between cold forging

steel and the hot forging steel in the process. 16MnCr5 is being a cold forging steel while 41Cr4 is a hot forging steel.

7.3 Forming Simulations & Failure Modes

The forming loadcase starts right after the cooling analysis finishes. The moving die has a velocity of 3.6 mm/sec, which is obtained from the press manual. The die on the other end is a fixed die. The model is remeshed during simulation when high deformation and/or distortion occurred in the elements.

The finite element simulations are highly useful to detect failures in the process. Such as buckling or overlapping. The buckling is the most severe type of failure in this process. Another failure type is the necking at the root of the flange zone. There is one more failure that cannot be simulated in MSC.Autoforge (specialized MSC.Marc for metal forming) that is cracking in the flange zone due high cooling rate.

There are two types of buckling:

1- Euler buckling
2- Plastic buckling

Euler buckling will be called buckling of the first kind from now on. It is the buckling occurring instantaneously and elastically. Buckling of the first kind is also called as elastic buckling. Plastic buckling will be called buckling of the second kind. It is buckling occurs during plastic deformation. In Figure 7.6, 210 mm long workpiece has been forged. The cooling time was 25 s with initial temperature of 1300 °C. The initial step size is 2200 (0.0342 s). The buckling seen in the Figure 7.6 is of the second kind. The part buckles like swallowing to one side after a high degree of deformation is reached. Nevertheless, this situation is not easy to capture as demonstrated in Figure 7.7. Here the model is the same as the one in Figure 7.6 but with bigger step size. The initial step size is 1800 (0.0410 s). The reason is believed to be that the instability point is missed between two time steps in the second model. When the length of the model shown in Figure 7.6 reduced from 210

mm to 168 mm., the buckling behavior cannot be observed in the results with the same initial step size of 2200 (Figure 7.8). This result is natural because for the 168 mm long workpiece the slenderness ratio s is at the limits given in the literature [4]: $s = l_o/d = 2.66$.

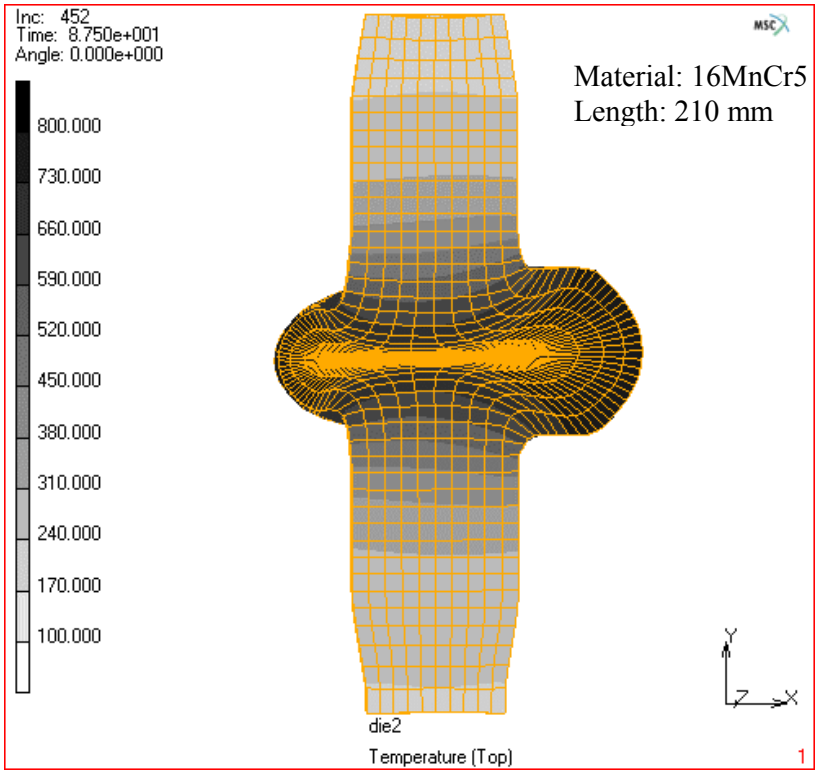

Figure 7.6 Plastic Buckling

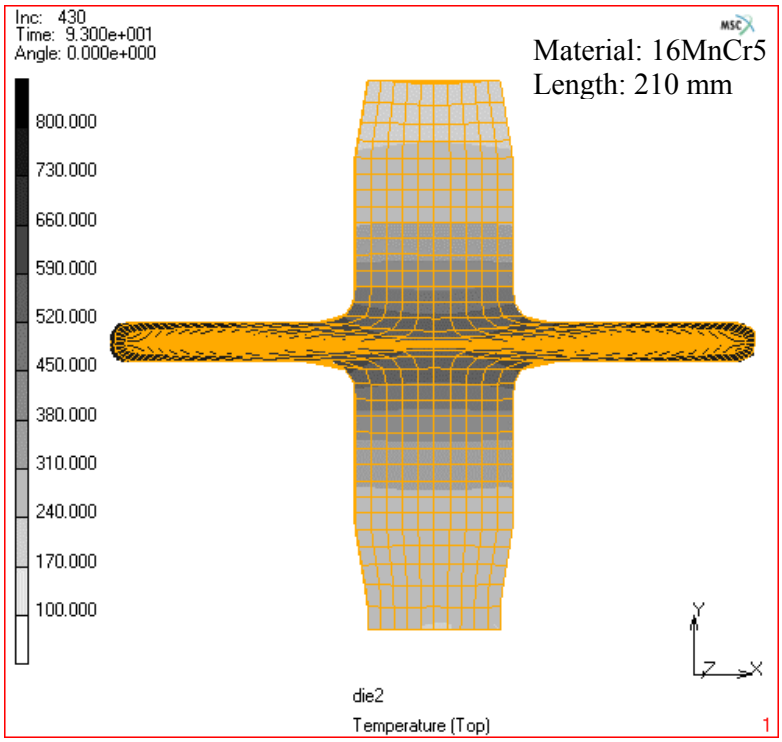

Figure 7.7 The model in Figure 7.6 solved with 1.22 times bigger step size

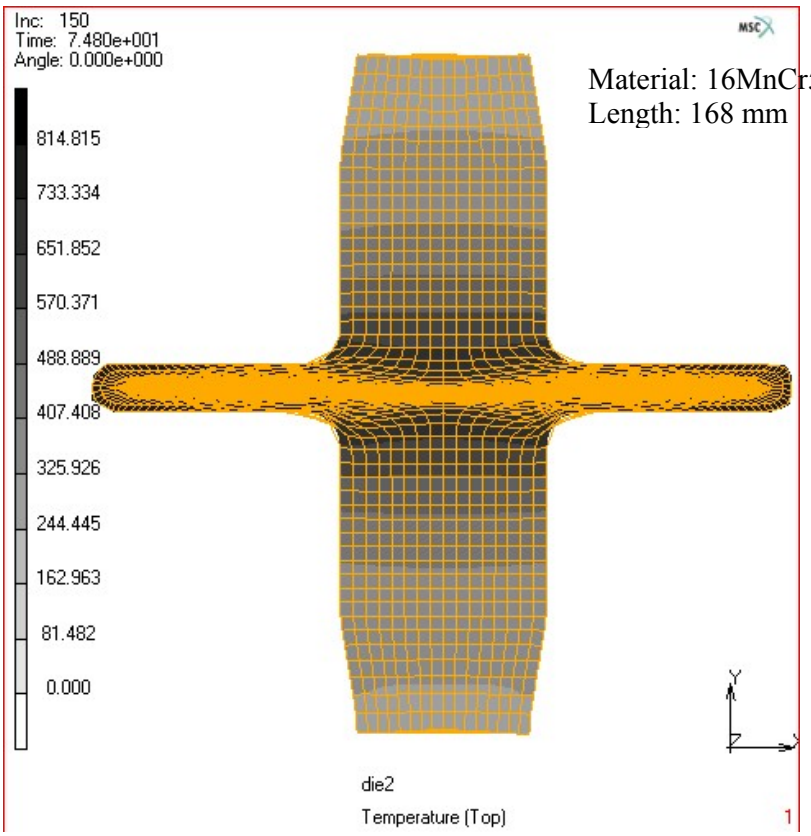

Figure 7.8 The model in Figure 7.6 formed with 42 mm smaller stock part

Figure 7.6 and 7.7 shows that the step size is an important parameter to simulate buckling in a FEM environment. Step size affects the convergence behavior of the job but also solution can be affected as explained above. The step size can cause solver to miss the point where buckling occurs. Where the ratio of l_o/d ratio is equal to 5.6. This model seems to be fine and there is no necking in the flange root.

For annealed 41Cr4 buckling of the first kind occurs nearly at the start of the process. This kind of buckling resembles to Euler buckling (Figure 7.9). The cause can be the material behavior. It can be stated that the force required to form the hot middle zone exceeds the critical force for buckling of the workpiece with material 41Cr4. The model (Figure 7.9) for this material was the same with the model in Figure 7.6 except this has material 41Cr4 instead of 16MnCr5.

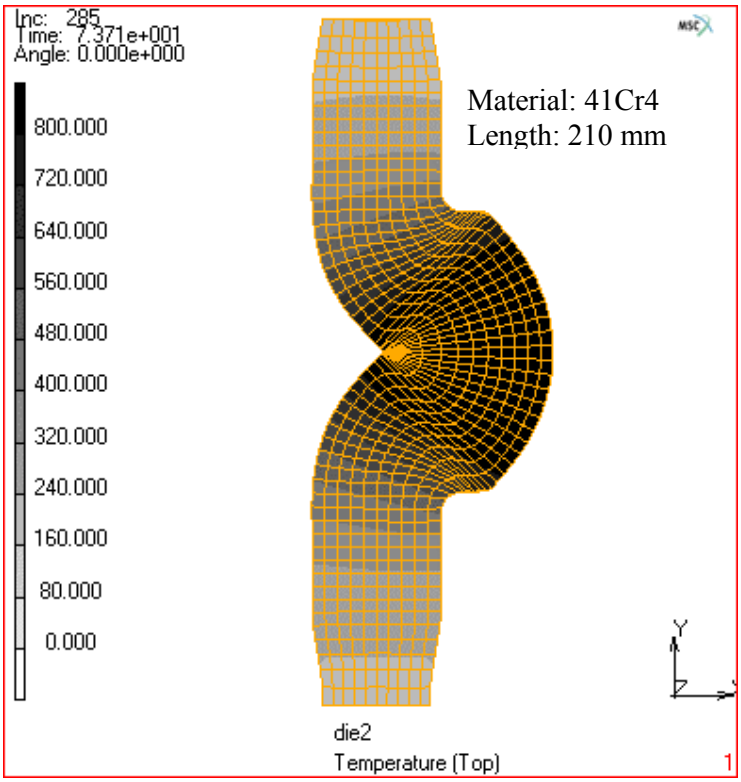

Figure 7.9 Euler buckling of 41Cr4 specimen (Same model as in Figure 7.6)

The other failures included in the process are necking in the flange root and overlapping of the material on to itself. Necking is mainly caused because of the ratio of the heated zone length to total workpiece length. The necking occurs at the border between hot and the warm material. The hot material forms a bulge in the flange zone leaving a smaller section near the flange root. This is called the neck region. A small canal surrounding the flange root can identify this failure (Figure 7.10). One case of necking is, if one of the dies hit the workpieces before the other die hits then the first die bends the flange to the other side causing failure in the flange (Figure 7.11). This behavior called overlapping, because the material tends to overlap onto itself due to bending. If the problem is not recognized there will a discontinuity inside the flange. This problem is mainly caused by placement of the hot zone. Necking failure of this kind can be avoided by adjusting the center of the heated zone area such that both dies hit at the same time.

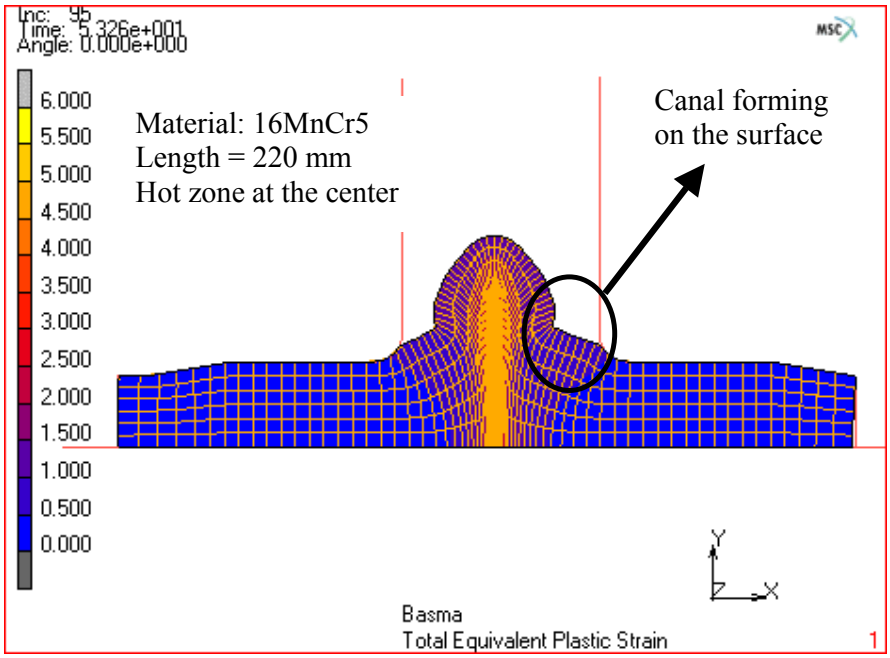

Figure 7.10 Necking problem

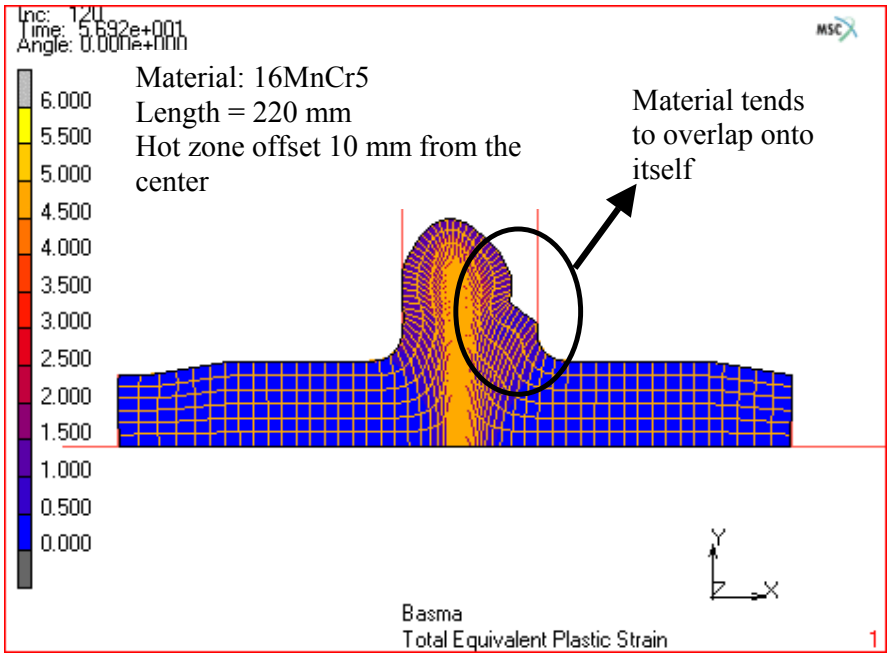

Figure 7.11 Overlap defect

7.4 Parametrical FEM Study

There are several parameters analyzed by finite element simulation that have not been analyzed in experiments. The main cause is the cost, time and equipment required for these experiments. So only, some of the simulations have been repeated with experiments.

In this section, FEM results for the following parameters will be presented:

1. The effect of the convection coefficient
2. The effect of workpiece length
3. The effect of punch velocity
4. The effect of material
5. The effect of die friction
6. The effect of heated zone length

7.4.1 The Effect of Convection Coefficient and Cooling Time

The convection coefficient mainly controls the heat loss to the environment. This parameter is important because the heat flow affects the temperature of the workpiece. The temperature affects the flow curve of the material and this goes on like a chain reaction. The flow curve affects the deformation behavior of the material. However, another aspect is the temperature regime for hot and cold forging. For example, if the hot region of workpiece is excessively cooled than the whole body will be at uniform temperature before the forging process begins. Then this fact leads to buckling because uniform body temperature causes workpiece to behave as one rigid body with a length that exceeds the limit of buckling given 2.6 in the literature. If the material has one hot region and two cold regions (Figure 7.12) at the end then these regions act independently. It can be simply thought that if the hot zone is above re-crystallization temperature it will act as if it is another workpiece that is hinged at the ends. Therefore, the whole process will be as if hot zone is forming between two rigid dies those are the cold zones with a shorter effective slenderness ratio.

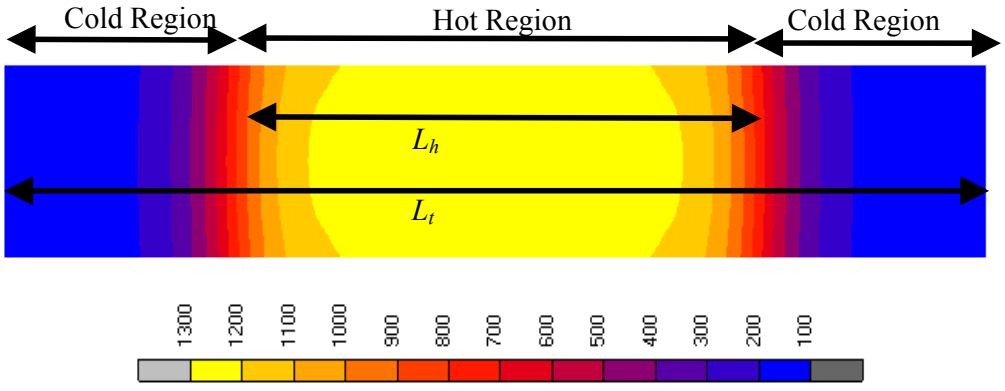

Figure 7.12 Temperature profile of the workpiece after cooling.

Table 7.1 Simulation Parameters for Simulations for Effect of Convection Coefficient

Materials Used	16MnCr5 (Marc Database)
Initial Conditions	1300 ºC Zone (L_h=98 mm) and all remaining parts are at 25 ºC
Contact Friction (Shear)	m = 0.2
Workpiece Length	210 mm
Element Edge Length Seed for 3-D remesher	X: 3 Y: 3 Z: 3 mm
Cooling time	5, 10, 15, 25, 35 s
Convection Coefficients	0.17, 0.3, 0.5, 1.5 W/mm^2·K
Stepping Procedure	Adaptive Steps (Seed: 500)
Solution Control	Non-Positive Definite Systems Allowed Strict Convergence Test
Convergence Criteria	Relative Residual check (Relative Force Tolerance=0.1)
Boundary Condition Multiplier	10^{-12}
Solver Used	Direct Sparse Solver

If this is the case then one should consider s as $s=L_h/d_o$ ratio rather than the $s=L_t/d_o$ ratio for buckling. The parameters used in the simulation are listed in Table 7.1. The out coming results from the simulations show that if the workpiece is cooled fast or cooling is prolonged then the buckling is influenced. The main problem is the whole body temperature converges to a temperature as the time passes so there is no separate zone at that point. Then this leads to a higher s ratio exceeding the limit. Above s=2.6 buckling occurs in the workpiece. In Figure 7.13, simulations can be seen with different cooling times. Longer cooling times leads to buckling. The workpiece that cools 25 s before the forming process buckles excessively. While the other workpiece, which has been cooled down only 15 s has only small amount of buckling. The surface temperature profile of the workpieces should also be checked. Figure 7.14 shows the temperature profile of the workpiece at the beginning of the forging sequence. The total workpiece length used for this simulation is 210 mm. Also the convection coefficient used was 0.17 W/mm^2·K. Difference between

maximum temperatures of the workpieces with different cooling times can be as high as 100 ºC. 100 º C difference can be important especially when the forging should be done just above the re-crystallization temperature. The process should be finished in a shorter time with the higher convection coefficient. Otherwise, the body temperature will drop below re-crystallization temperature, which is not desired.

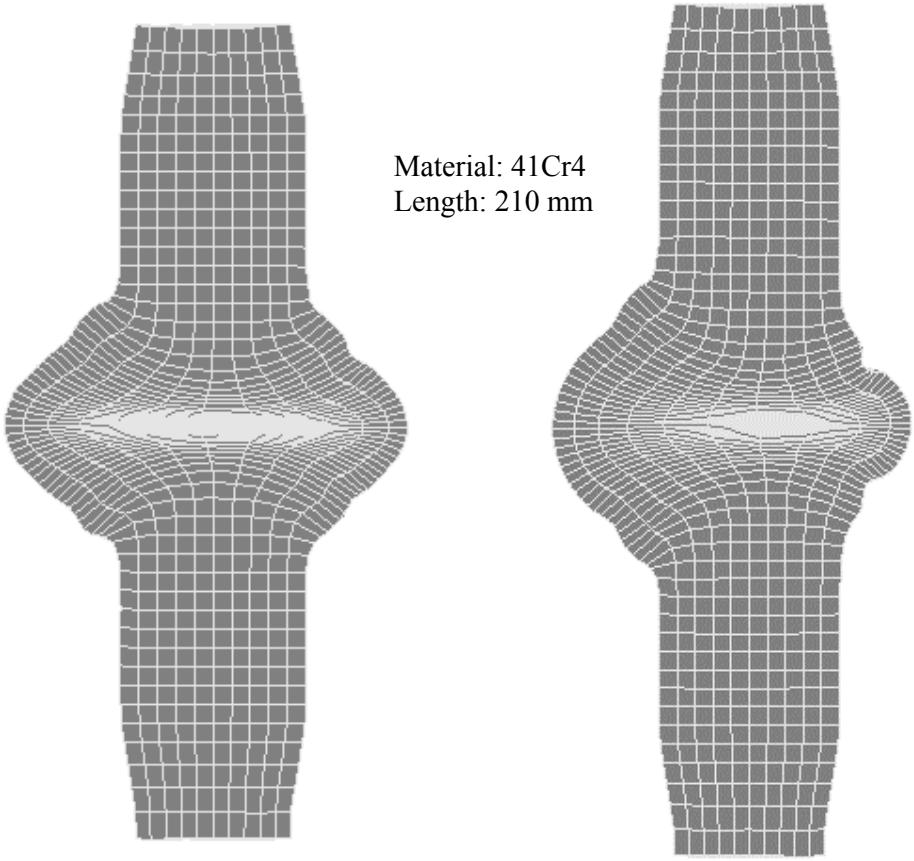

a) Cooling time t=15 s **b)** Cooling time t=25 s

Figure 7.13 Effect of cooling time on buckling

The temperature drop is also significant during the forging process because of the low punch velocity despite the energy input by the deformation. Forging process time can be as long as 40 up to 50 seconds. The convection coefficient affects the process adversely. the higher the convection coefficient the higher the cooling rate. The high temperature drop will result in that the body temperature drops below the re-crystallization temperature. The recrystallization temperature for 16MnC5 and 41Cr4 is about 800 °C [Metals Handbook, 2001]. Increasing the convection coefficient creates the same effect as long cooling times. Nevertheless, with one difference, the high convection coefficient causes more energy loss to the environment. When the Figures 7.14 and 7.15 are compared this can be easily seen. Figure 7.14 shows a more smooth transition of the temperatures while Figure 7.15 shows a sharp transition zones. For example, a convection coefficient of h=1.5 W/mm^2·K cools down the workpiece below 800 ºC before forging.

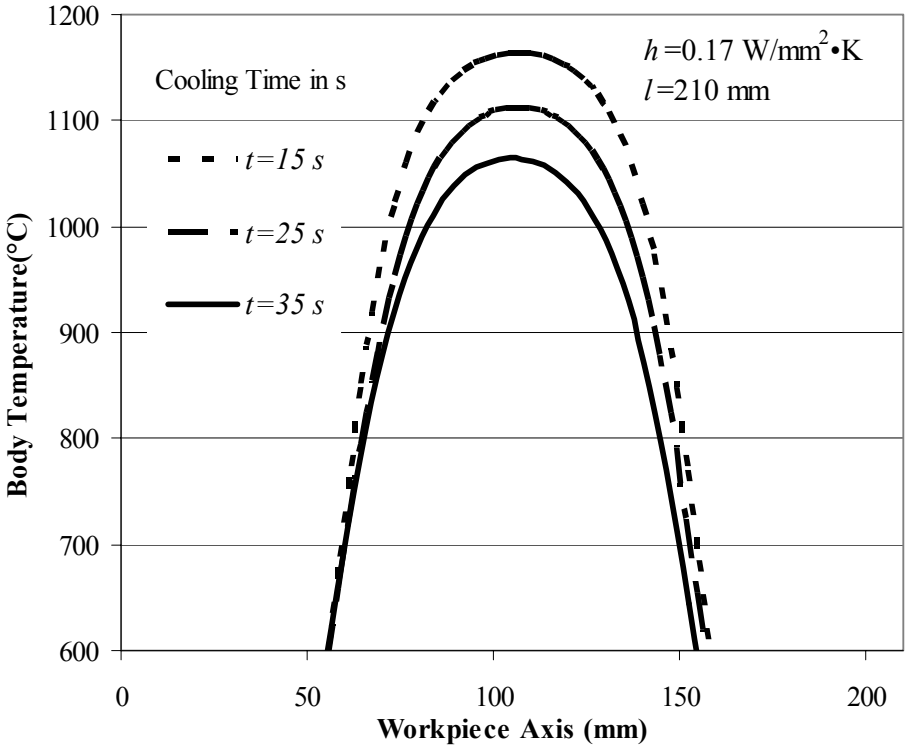

Figure 7.14 Temperature profiles before forging process with different cooling times.

The workpiece length shown in Figure 7.14 is over the limit for buckling given in the literature [4]. However, with the help of the hot zone in the middle the workpiece do not buckle if the following conditions are satisfied: The hot zone temperature should be above recrystallization temperature (800 °C) at the middle of the workpiece. This is satisfied during the finite element simulations. Figure 7.16 explains this condition. The workpiece which has a convection coefficient of h=1.5 W/m^2·K buckled (Figure 7.16c). Because during forging the workpiece cooled below 800 ºC and the workpiece acted as one rigid body. The workpiece (Figure 7.16b) which has a relatively low convection coefficient h=0.5 W/m^2·K is also buckled. However, its buckling is somewhat different from that of Figure 7.16c: The buckling in Figure 7.16c is Euler buckling. However, the buckling in Figure 7.16b is not that kind it plastic buckling. The workpiece with the lowest convection coefficient h=0.3 W/m^2·K is not buckled (Figure 7.16a). The workpiece is successfully formed with a symmetric flange.

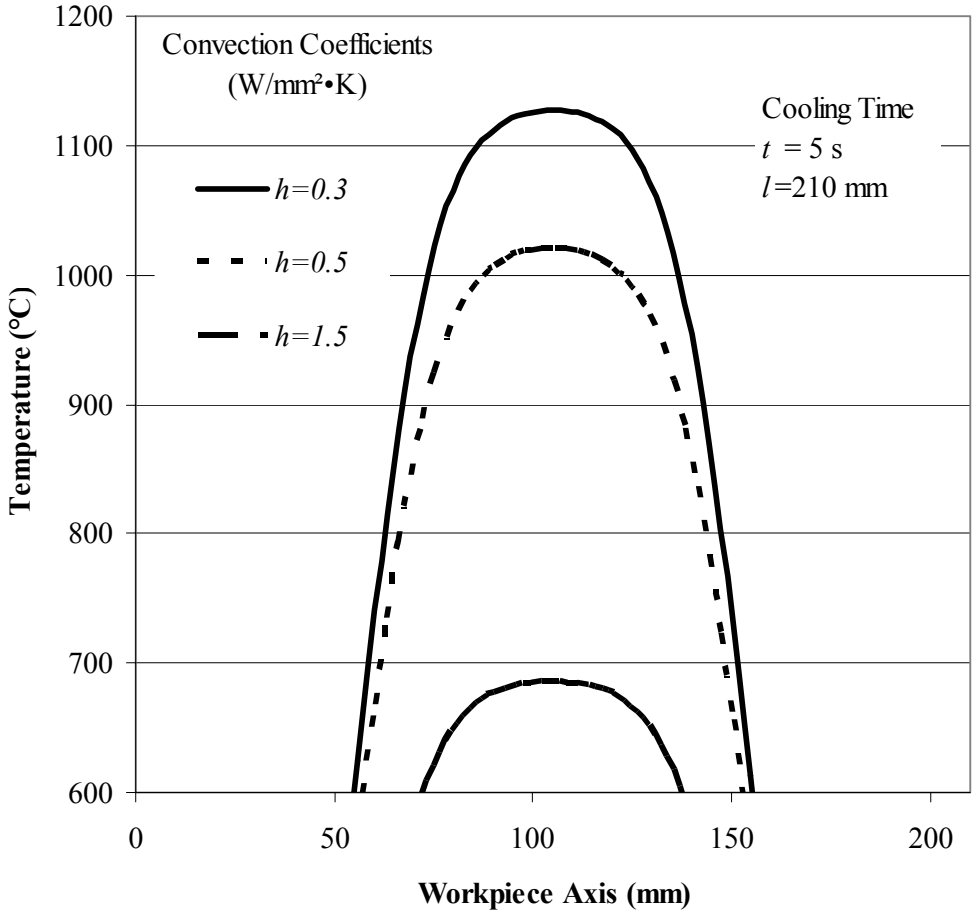

Figure 7.15 Temperature profiles on the surface of the workpiece before forging with different convection coefficient

The situation can be understood by analyzing Figure 7.15. The workpieces shown in Figure 7.16 are 210 mm long and the initial body temperatures are 1300 ºC. At the start of the forging (Figure 7.16c) the process has the highest temperature in the middle at about 650 ~ 700 ºC. The highest temperature of the workpiece shown in Figure 7.16c is about 480 ºC. The whole body at the start of the forming process is below re-crystallization temperature and the whole body is at uniform temperature. The buckling reason is now clear, if a uniform body exceeds the slenderness ratio of s = 2 the body will suffer under Euler buckling. The workpiece in Figure 7.16b started the process above 1000 ºC in the hot zone. However, due to the cooling during forming, temperature dropped below 750 ºC.

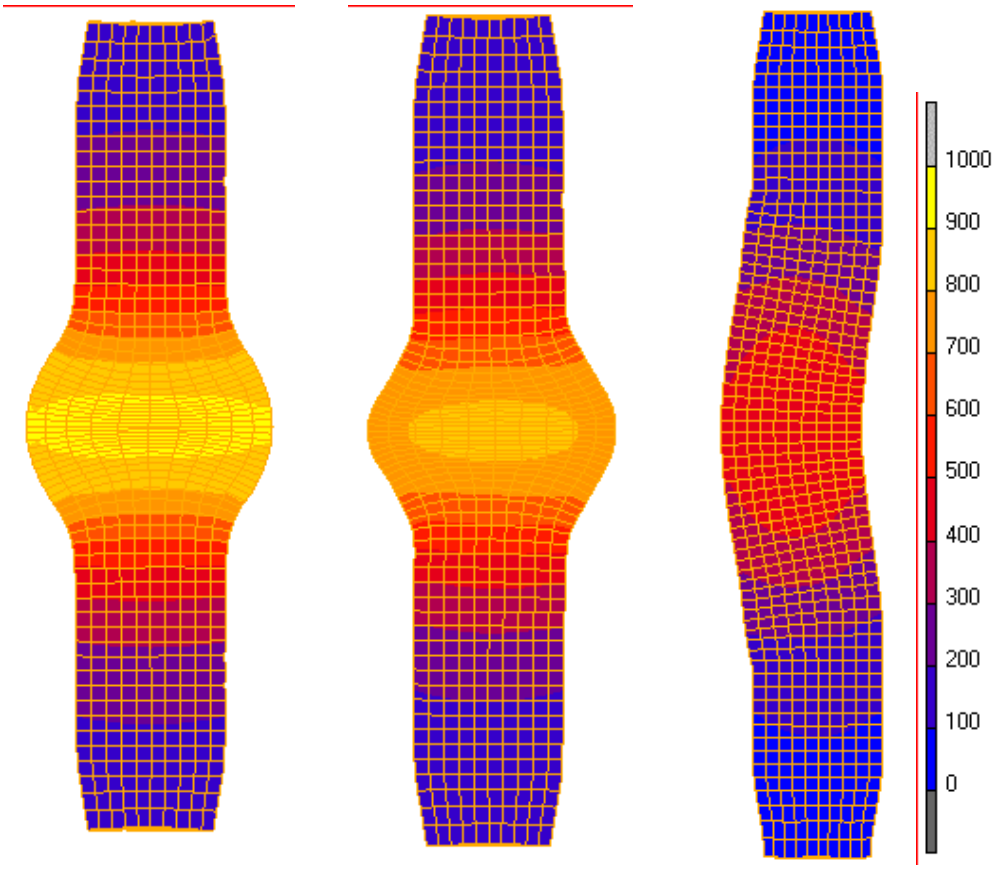

a) h=0.3 W/mm^2·K **b)** h=0.5 W/mm^2·K **c)** h= 1.5 W/mm^2·K

Figure 7.16 The effect of convection coefficient on forging (t=5 s cooling time)
Material: 16MnCr5, L_T = 210 mm
(Countour band is showing temperature profile in °C)

Buckling started when the distance between surfaces of two dies is about 90 mm and the bulge temperature was about 800 ºC. When this fact is compared with Figure 7.16a, the bulge temperature of this workpiece at the corresponding state is about 880 ºC. This could mean that for material 16MnCr5 below 800 ºC, buckling can occur. The problems here can be solved by using a high-speed punch but then a powerful drive is needed because when the strain-rate is increased the punch force will also increase. The workpiece in Figure 7.16c buckled under a load of 11 tons and similarly in Figure 7.16b. The workpiece in Figure 7.16a was under a load of 21 tons without buckling.

7.4.2 The Effect of Workpiece Length

The workpiece length is another parameter in the simulations. The buckling phenomenon is closely related to the workpiece length. Shortening the length of stock piece also means reducing the process time. Reduction in time means higher temperatures during deformation. This is important as mentioned before, since the hot zone will behave as a hinged body above 800 ºC.

Table 7.2 Simulation Parameters for Simulations for the Effect of Workpiece Length

Materials Used	16MnCr5-41Cr4 (Marc Database)
Initial Conditions	1300 ºC Zone (L_h=98 mm) and all remaining zone are at 25 ºC
Contact Friction	m = 0.2
Element Edge Length Seed for remesher	X: 3 Y: 3 Z: 3
Cooling time	5, 10, 15, 25, 35 s
Convection Coefficients	0.3 W/mm^2·K
Punch Velocity	3 mm/s
Solver Used	Direct Sparse Solver
Workpiece Length	210, 180 and 150 mm
Other properties are same with Table 7.1	

At critical s-ratios above (s>2.6) the workpiece starts to buckle after the body temperature drops below 700~800 ºC. The critical lengths for the workpiece used in the experiments are above 160~170 mm. Below this length the buckling is not a problem and the change in the temperature profile affects only the punch force. Table 7.2 shows the parameters that simulations were ran with. The simulations showed that the material 41Cr4 is highly sensitive to the temperature profile. The parameters used with 41Cr4 are cooling phase time 15~25 s and convection coefficient h=0.3 W/m^2·K These simulations end up with buckling for a workpiece length of 180 mm and 210 mm. The same parameters for 16MnCr5 did not lead to the same behavior unless the convection coefficient is changed to h=0.75 W/m^2·K. The s ratios for these workpiece lengths are respectively 2.86 and 3.86. The force

displacement curves (Figure 7.17) show that as the workpiece length increases the punch force will increase. The die velocity is constant at 3 mm/sec in Figure 7.17.

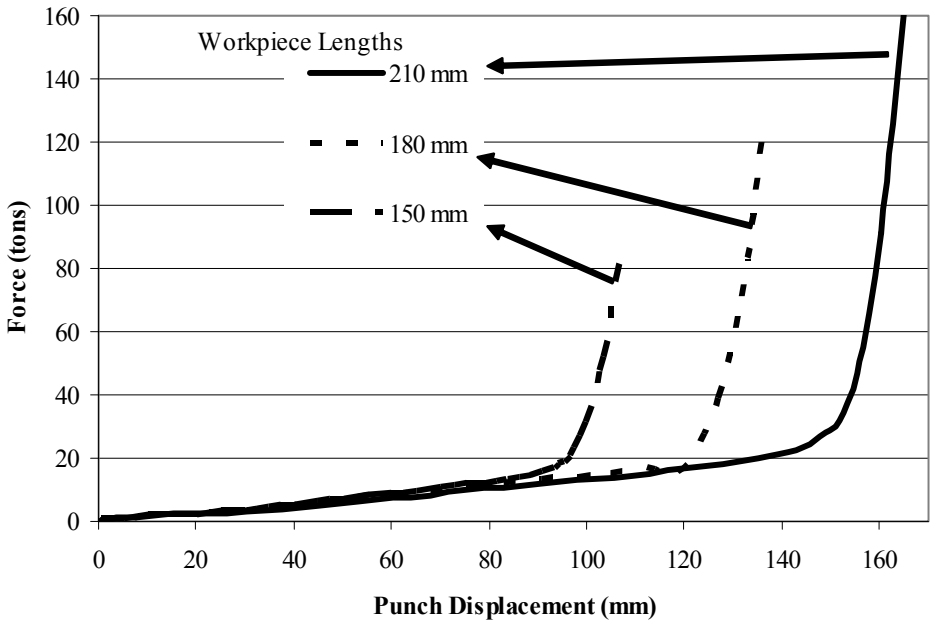

Figure 7.17 Force-displacement curve for different workpiece lengths

The reason for this is the larger material stock in the flange zone need to be flattened. In the force displacement curve (Figure 7.17), there is no significant force difference during the extrusion part of the process. Extrusion process starts at 25 mm punch displacement. Extrusion ends at 64 mm, 112 mm and 140 mm punch displacement for 150 mm, 180 mm and 210 mm long workpieces respectively. The difference begins while forming the flange. According to the graph (Figure 7.17), the force required to form a flange with 210 mm workpiece requires two times more force, than forming a flange with 150 mm workpiece. Forming process time periods are not same for 210 mm long workpiece and the 150 mm workpiece. The difference between two comes from the additional 60 mm distance that the punch required to move. The time required for this distance is about 20 s with 3 mm/s punch velocity. This time is very important because in every second the workpiece

is cooling down and the process is losing the advantage of simultaneous hot and cold forming. Higher punch velocities may help which will be investigated in the following sub-sections.

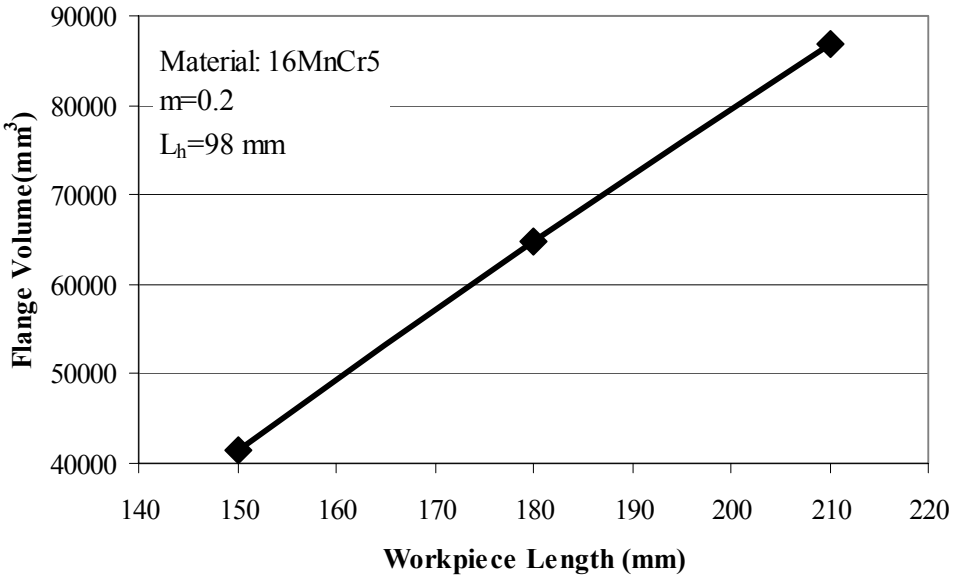

Figure 7.18 Maximum flange volume for different workpiece lengths

At the same time the workpiece length also determines the flange radius. The higher is the workpiece length, the bigger is the flange radius. In Figure 7.18, the workpiece length versus flange volume relation can be examined. The flange volume is linearly increasing with the increasing workpiece length. This type of behavior is expected because the volume added to the stock piece appears inside the flange. In addition, the strains go to extreme values, which the material cannot sustain. In the strain graphs (Figure 7.19 and Figure 7.20) it can be examined that the longer the workpieces, the larger is the total plastic strain. The workpiece can have voids, which will absolutely limit the process in the experiments. Above re-crystallization temperature, this is not significant but because of the physical contact with the die, the workpiece cools below re-crystallization temperature (about 800 °C).

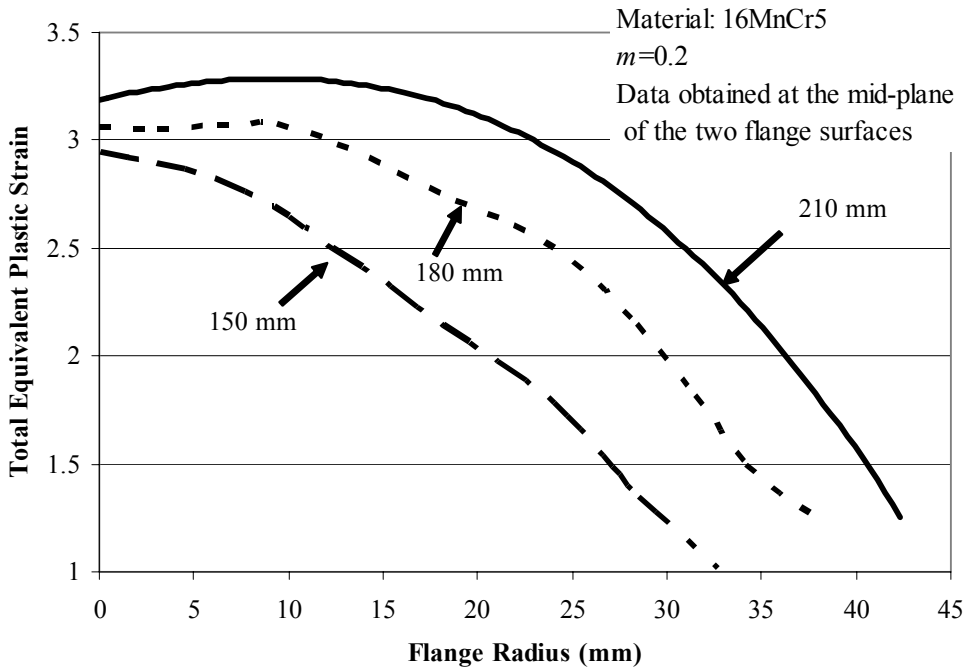

Figure 7.19 The total equivalent plastic strain at the centerline of the flange

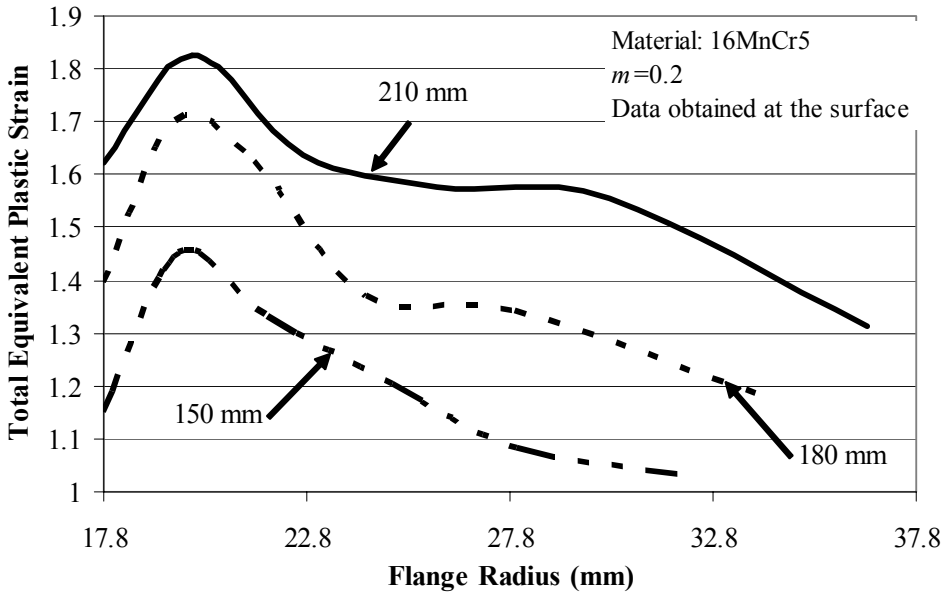

Figure 7.20 The total equivalent plastic strain at the surface of the flange

Also below recrystallization temperature, strain hardening will occur. The high strain hardening of the workpiece can lead to failure so that the part needs to be heat-treated before. On the surface of the flange, the effect of workpiece length can be seen easily. The strain value on the surface of the 210 mm and 150 mm long workpieces are 1.3 and 1 respectively at the end of the flange. At the centerline of flange of 210 mm workpiece, the total strain value goes above 3 from r=0 to r=28 mm radius. This radius value is nearly two times the original value with that much plastic strain. In addition, the constant strain zones seen in Figure 7.19 seem to be inclusion of cold zones in the flange. This type of behavior can only been seen in the 210 mm and 180 mm long workpieces. The 150 mm long workpiece does not show that kind of behavior. This is expected because the extra volume added is the cold volume in 210 and 180 mm long workpieces and as stated before this extra volume adds to the flange volume. These zones are also the highly hardened zones because of the degree of plastic deformation.

7.4.3 The Effect of Punch Velocity

The punch speed affects the total process time and the strain rate. Generally, cold forming is not strain rate sensitive. While hot forming is strain rate sensitive. Strain rate sensitivity means the increase in the flow stress when the strain rate increases. The strain rate will increase with punch velocity and the strain rate directly affects the flow curve of the material. As a result, the punch force will increase with the increasing punch velocity. Lowering the process time is beneficial when we consider that the workpiece body will cool down less. High temperatures in the hot zone will create the adverse effect of high strain rates. There are several simulations made with different punch velocities. The simulation parameters used for this investigation are listed in table 7.3. Another benefit of increasing punch velocity thought to be to prevent buckling. However, the simulations showed that this is not the fact. This was related to the fact that at high strain rates hot zones behave more rigid. The punch force displacement graph (Figure 7.21) shows that at high punch velocities the punch force will drop. When the punch force-displacement graph is

investigated it can be seen that in the cold extrusion part only the lowest punch velocity has some difference other velocity settings give identical results in cold extrusion force. On the other hand the forming of the flange makes the difference. At this stage the forces increase dramatically depending on the punch velocity with one exception. The punch velocities of 15 mm/s and 30 mm/s did not show any significant difference. The process time for the 30 mm/s is about 21 seconds while for 15 mm/s punch velocity that is about 28 seconds. The increase in the maximum force by decreasing the punch velocity %40 from 15 mm/s to 9 mm/s is about %50. The maximum force required for the same displacement of the punch is 93 tons and 63 tons for 9 mm/s and 15 mm/s respectively. When the punch velocity is lowered %66 percent from 9 mm/s to 3 mm/s. The punch force nearly increases %100 form 93 tons up to 165 tons.

Table 7.3 Simulation Parameters for Simulations for the Effect of Punch Velocity

Materials Used	16MnCr5 (Marc Database)
Initial Conditions	1300 ºC Zone (L_h=98 mm)
Contact Friction	m=0.2
Element Edge Length Seed for remesher	X: 3 Y: 3 Z: 3
Cooling time	15 s
Convection Coefficients	0.3 W/mm^2·K
Punch Velocity	3, 9, 15, 30 mm/s respectively
Solver Used	Direct Sparse Solver
Workpiece Length	210 mm
Other properties are same with Table 7.1	

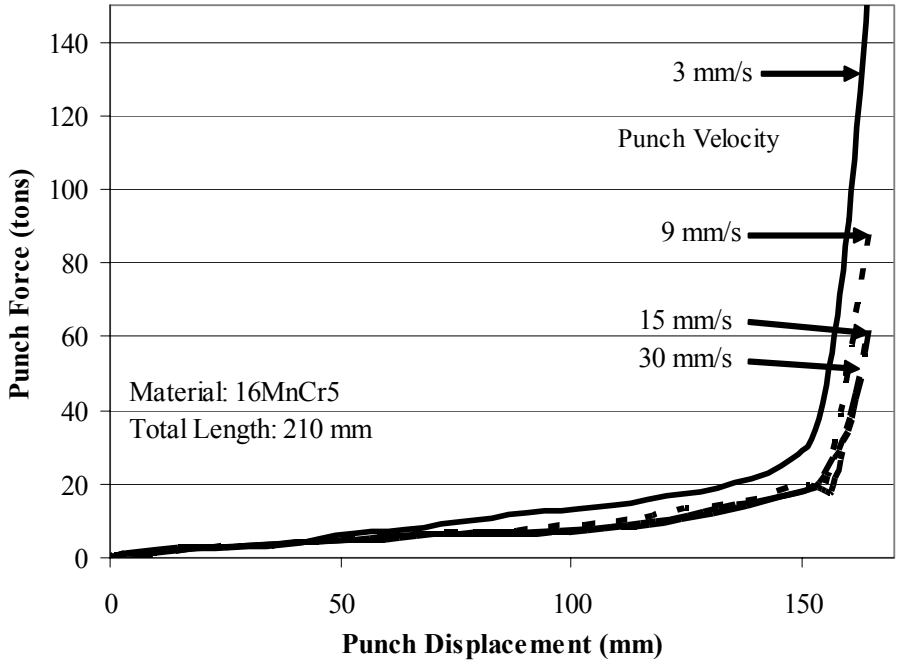

Figure 7.21 The Punch displacement vs. Punch force curve at different punch velocities

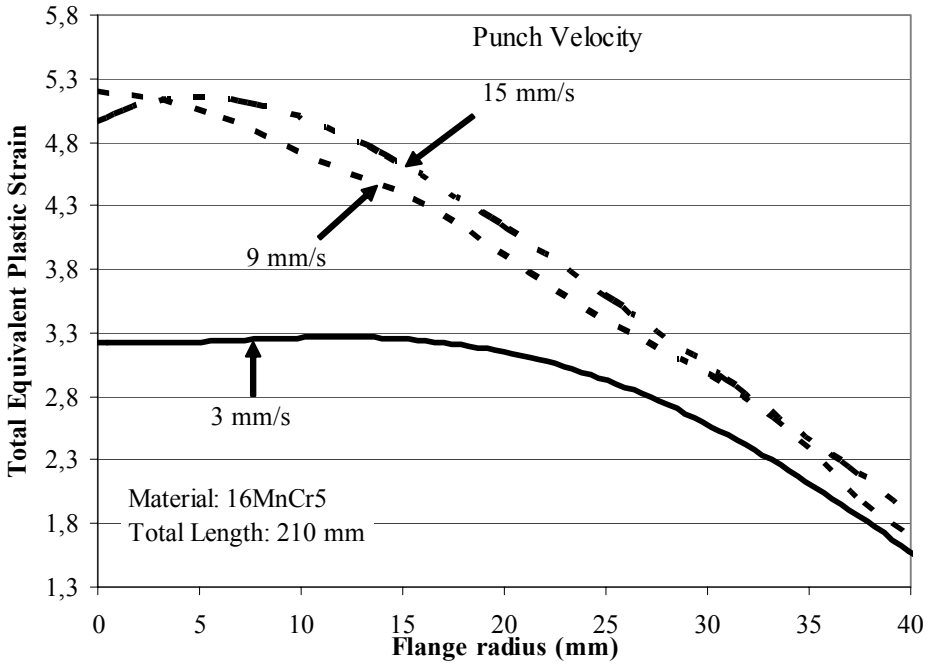

Figure 7.22 The total equivalent plastic strain at the center plane of the flange

This fact is closely related to the cooling phenomena. It needs much more effort to form a cold flange than to form a hot one. The simulations showed that the effect of the temperature of the body is dominant over the strain-rate effect. The graph of total equivalent plastic strain vs. flange radius (Figure 7.22) shows that as the punch velocity increases also the plastic strains at the mid-point of the flange increases. At high punch velocities the constant strain zone disappears. The equivalent plastic strains reach extreme values like 5 when compared with 3 at the flange root. The difference between the model with punch velocity of 3 mm/s and 9 mm/s comes from the difference in the formation process. Figure 7.23 shows that with the high punch velocity the end of the workpiece does not extrude correctly. This creates the difference in the total equivalent plastic strains. The punch velocities of 30 mm/s, 15 mm/sec and 9 mm/sec do not show a significant difference in plastic strains.

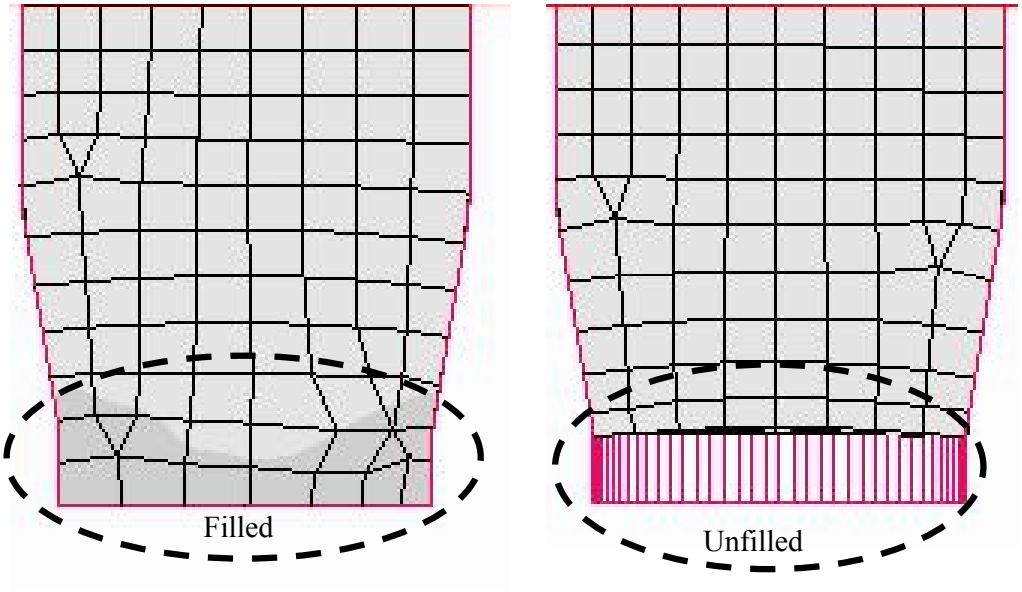

a) Punch Velocity=3 mm/sec b) Punch Velocity= 9mm/sec

Figure 7.23 The difference in the process with different punch velocities

7.4.4 The Effect of Material

The material type affects the process significantly. Material type change can change the whole process behavior. Two different materials were used in the simulations these were 16MnCr5 and 41Cr4. The material 41Cr4 is not used in the experiments instead 50CrV4 was used. The reason for that is the material data for 50CrV4 to input into the simulations could not be obtained. A similar material (41Cr4) is selected from the material database of MSC.Marc corresponds to 50CrV4 in the simulations. Figure 7.24 shows the flow curves for the materials 50CrV4 and 41Cr4. The strain-rate value at which the 50CrV4 flow curve is measured is 0.5 s^{-1} and the 41Cr4 in the database has the lowest strain rate of 1.6 s^{-1}. Flow curves at low temperatures do not change significantly with strain-rate so they can be compared. The flow curves of the two materials are similar (Figure 7.24). Even though there is 10% difference at 500 °C but this can because of the strain rates are different for two curves. As explained before at high temperature strain rate can affect the flow curve. The material selection done in order to have one cold forging steel

Table 7.4 Simulation Parameters for Simulations for the Effect of Material Type

Materials Used	16MnCr5, 41Cr4 (Marc Database)
Initial Conditions	1300 ºC Zone (L_h=98 mm) and all remaining zone are at 25 ºC
Contact Friction	m = 0.2
Cooling time	15 s
Convection Coefficient	0.3 W/mm^2·K
Punch Velocity	3 mm/s
Workpiece Length	150 mm
Other properties are same with Table 7.1	

that is 16MnCr5 and one hot forging steel that is 50CrV4 (in simulations 40Cr4). The 50CrV4 is called hot forging steel because it is not easy to form with cold forging. The loads required to form can have a negative impact on die life. Also a

larger forming machine is needed. Similarly, 16MnCr5 is called cold forging steel because the flow stresses are lower when compared to 50CrV4 (41Cr4) (Figure 7.26). Generally the workpieces with material 41Cr4 buckled even at a workpiece length of 180 mm where 16MnCr5 did not buckle with parameters listed in Table 7.4. Also with the material 16MnCr5 the extrusion at the end may not finish depending on several parameters like friction but workpieces with material 41Cr4 always forms at the ends before bulging. This behavior is similar to that shown in Figure 7.23. If the flow curve is examined carefully, the flow curve of 41Cr4 at 500 ºC has higher flow stress values than 16MnCr5 at 200 ºC at small plastic strains. The E_T (tangential elastic modulus) is also higher when compared to 16MnCr5 at 500 °C. This explains the reason that why this material is too stiff (high E_T value) even at high temperatures. Tangential elastic modulus (E_T) is measured by local inclination of the flow curve. This behavior shows that this type of materials should be used with care in this kind of process.

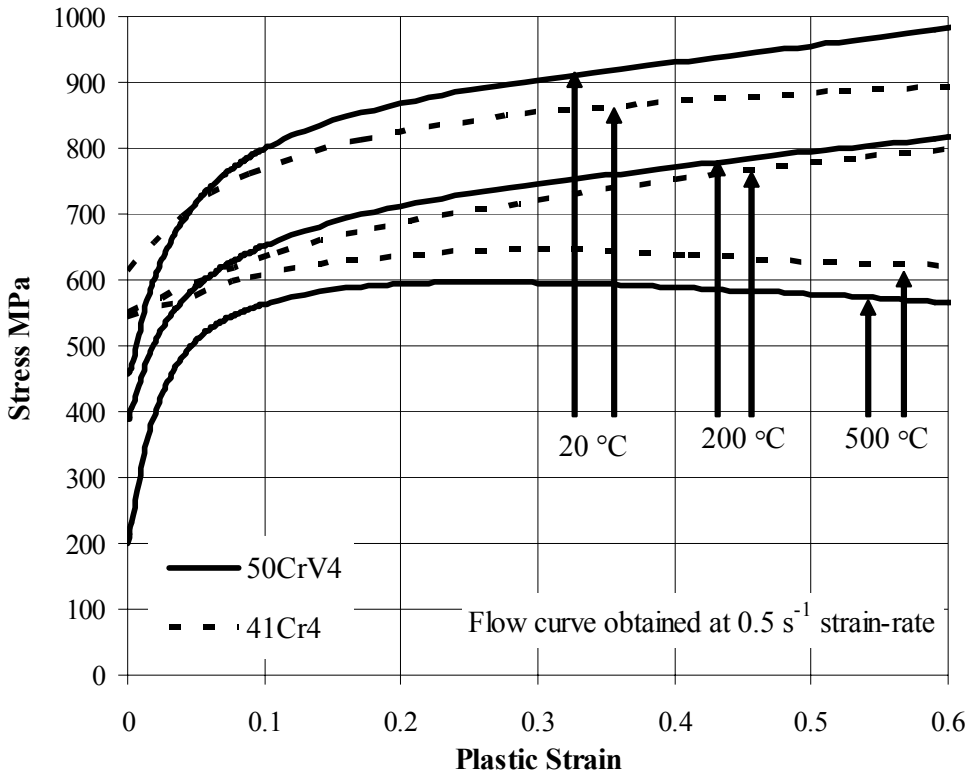

Figure 7.24 Flow curves of 41Cr4 and 50CrV4 ($\dot{\varepsilon} = 0.5$)

Changing the punch velocity did not help to prevent buckling of workpieces with material 41Cr4. As expected the force required to extrude and to form the bulge is higher for 41Cr4 (Figure 7.27). Both force displacement curves overlap at the start of the process but then after the 41Cr4 makes a big change in the slope. The slope for 41Cr4 is bigger then the slope for 16MnCr5. At the end of the process, punch forces of two materials tend to close each other because of the thin flange (10 mm). Forming forces jump as flange thickness decreases. The case is investigated analytically below.

Flow curve for hot materials [1]:

$$\sigma_f = K\dot{\varepsilon}^m \tag{7.1}$$

Assuming no friction [1]:

$$\sigma_f = \sigma_z \tag{7.2}$$

Punch force for upsetting without friction:

$$F = \sigma_f \cdot A \tag{7.3}$$

Combining Equations (7.1) and (7.2) gives:

$$F = K\dot{\varepsilon}^m A \tag{7.4}$$

Equivalent plastic strain-rate for upsetting is equal to [1]:

$$\dot{\varepsilon} = \frac{v_{punch}}{h} \tag{7.5}$$

Replacing Equation (7.5) in (7.4) will result:

$$F = K\left[\frac{v_{punch}}{h}\right]^m A \tag{7.6}$$

The punch force is found for upsetting without friction assumption in Equation (7.6). Assuming m=0.1 and K=70 N·s^m/mm^2 the punch displacement versus punch force curve calculated in Figure 7.25. As seen in Figure 7.25 the punch force jumps as the flange thickness decreases. In addition, the friction between the die surface and the flange surface restricts the material flow to the sides. Thus, it results in increased punch force required to finish the process. The buckling behavior of the 41Cr4 with longer workpieces can be linked to its stiffness and the change in the extrusion force after the extrusion process is started. The stiffness is the Elastic modulus (E) or Tangential modulus (E_T). Tangential modulus is defined in the plastic zone of the flow curve and $E_T = d\sigma/d\varepsilon$. The stiffness directly affects the Euler (elastic) buckling behaviour of the material.

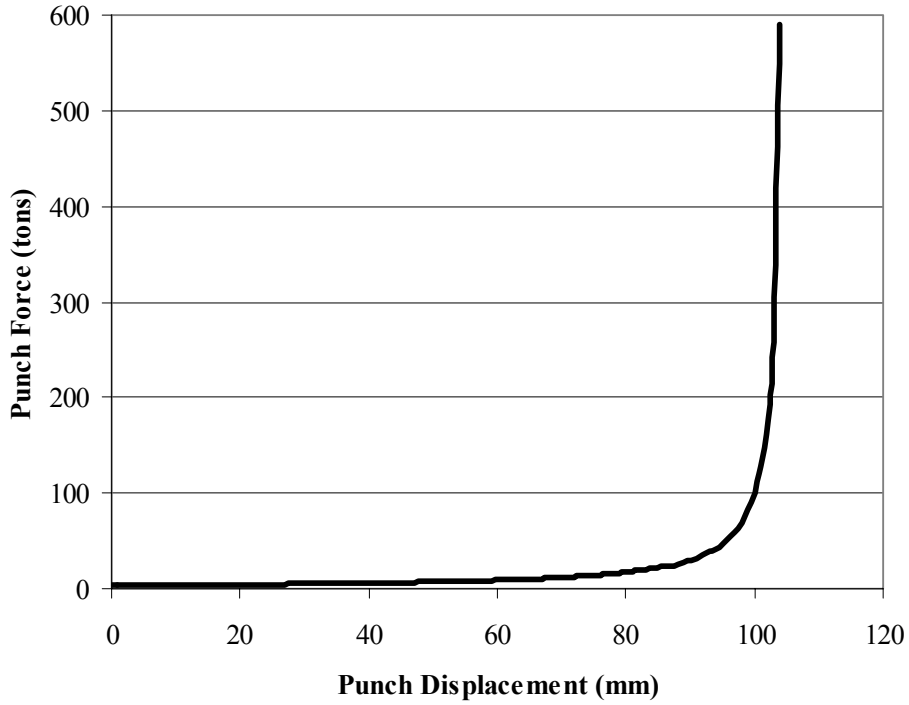

Figure 7.25 Punch force vs. Displacement
(Calculated analytically by using Equation 7.6)

7.4.5 The Effect of Die Friction

Die friction is an important phenomenon that has direct impact on the punch force. The friction in real life is unknown and it is non-uniform. The friction parameter is generally is a guessed value. In the simulations shear friction model is used. At high pressure levels, it has been suggested that τ is proportional of the flow stress of the material i.e., $\tau=m(\sigma_0/\sqrt{3})$, and is not proportional to the pressure. The proportionality factor m is called constant [2]. It is dependent on the two mating

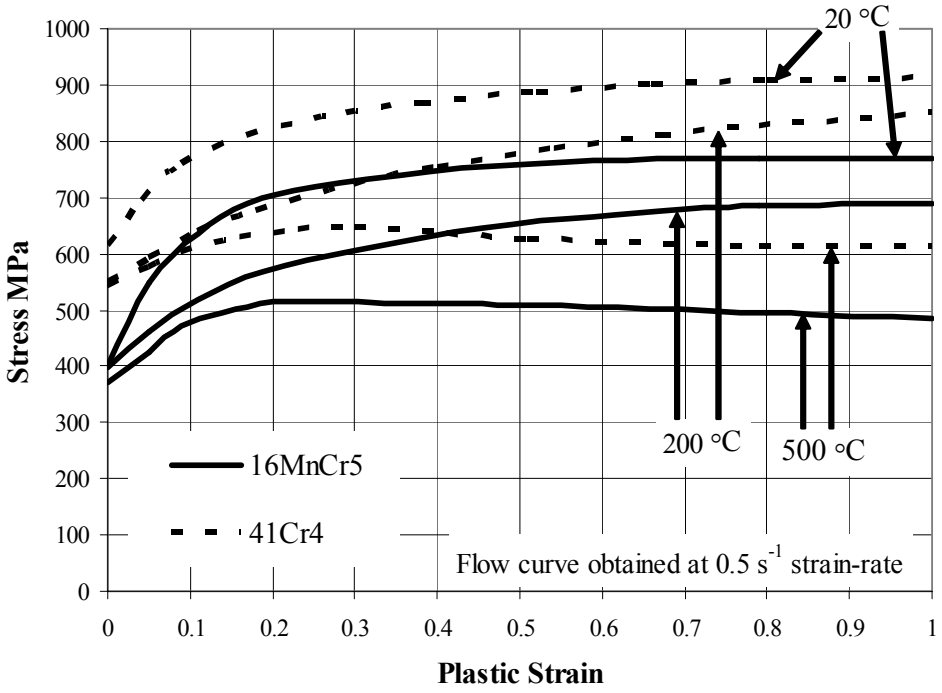

Figure 7.26 Flow curves of 16MnCr5 and 41Cr4

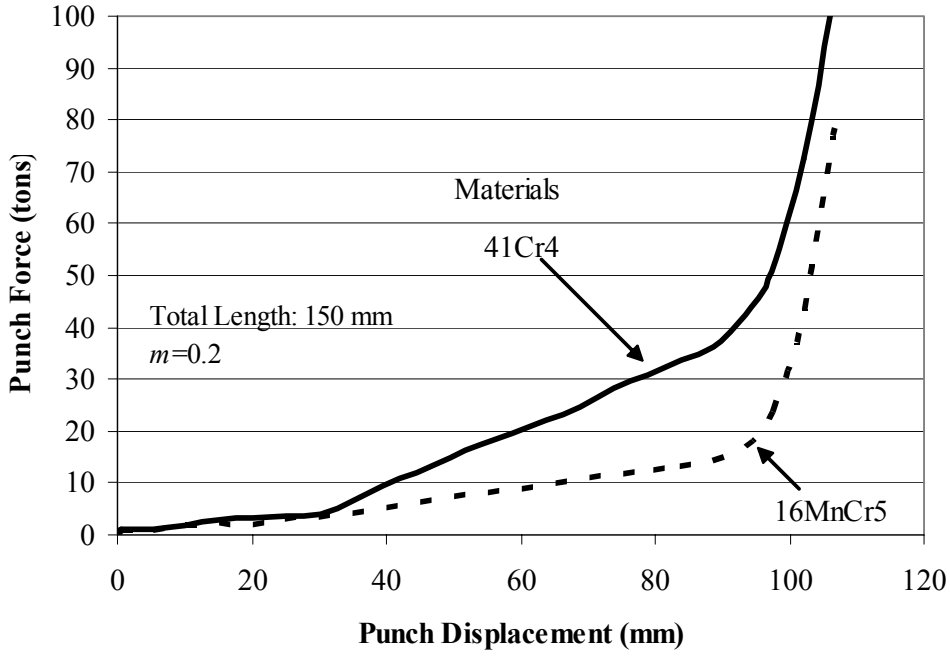

Figure 7.27 Punch displacement vs. Punch Force (Constant Velocity punch)

Table 7.5 Simulation Parameters for Simulations for the Effect of Die Friction

Materials Used	16MnCr5 (Marc Database)
Initial Conditions	1300 ºC Zone (L_h=98 mm) and all remaining zone are at 25 ºC
Convection coefficient	0.3 W/mm^2·K
Cooling time	15 s
Friction Coefficients	m=0.2, 0.1
Solution Control	Non-Positive Definite Systems Allowed Strict Convergence Test
Punch Velocity	3 mm/s
Solver Used	Direct Sparse Solver
Workpiece Length	150 mm
Other properties are same with Table 7.1	

surfaces and on the lubricant, and therefore also on the temperature. For high pressures such as those in metal forming, the assumption of a constant friction

factor *m* is more prevalent than the assumption of the Coulomb friction [2]. The friction factor for cold extrusion of steels is between 0.05 and 0.1 depending on the lubricant. The friction factor value for hot forging of steels is 0.2 with graphite lubricant [4]. MSC:Marc software has implemented a friction database in its code. According to this database 0.05 represents the good lubrication and 0.3 represents the worst case for cold forging of steels friction. Also friction values are given for hot forging of steels. These are 0.1, 0.2 and 0.6 representing good, medium and bad lubrication respectively. The friction values in the simulations are selected as 0.1 for good lubrication and 0.2 for inadequate lubrication. The punch displacement vs. punch force graph (Figure 7.28) shows no significant difference between two friction values. There is a slight difference in the extrusion process at the start. While forming the flange both curves overlap each other. However, after the flange thickness has reached a critical value the higher friction factor increases the punch force slightly more. In addition, the coulomb friction model is applied with the same coefficients to the model but no difference was observed in the punch force.

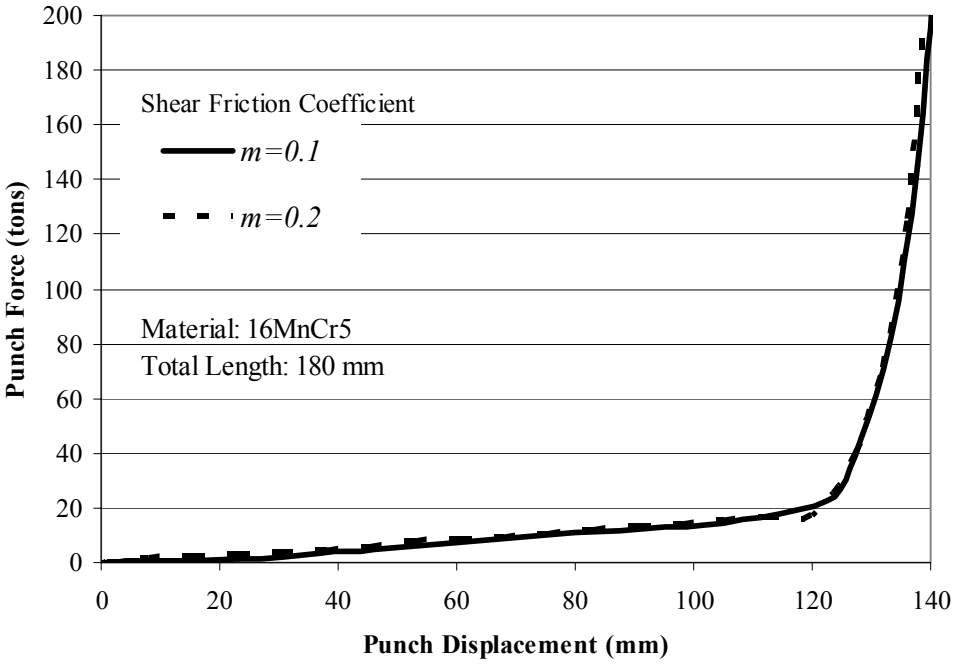

Figure 7.28 Effect of friction on Punch displacement vs. Punch force

7.4.6 The Effect of Heated Zone Length

The heated zone length changes the temperature profile of the workpiece body. The workpieces have a total length of 180 mm. The slenderness ratio *s* of the heated zone length is 2, 2.4, 3.26 and 4 for 60, 72, 98 and 120 mm long heated zones respectively. The workpiece with 120 mm heated zone simply buckled in the FEM simulation at the beginning of the process. The heated zone length of 120 mm is extremely long for upsetting and the body remaining between lower and the upper die is at uniform body temperature. As discussed before the body at uniform temperature will act as a single body naturally. However, the workpiece with 72 mm workpiece length has slight buckling behavior. The heated zone length of 72 mm is not very long for this process. The body remaining between two dies after end-extrusion has three distinct temperatures zone. These are cold region at the bottom, hot region at the middle and again cold region at the upper part. All these regions have small slenderness ratios. The simulation for the workpiece with 72 mm heated zone showed a slight buckling in the flange area. This buckling is in the form of an eccentric flange.

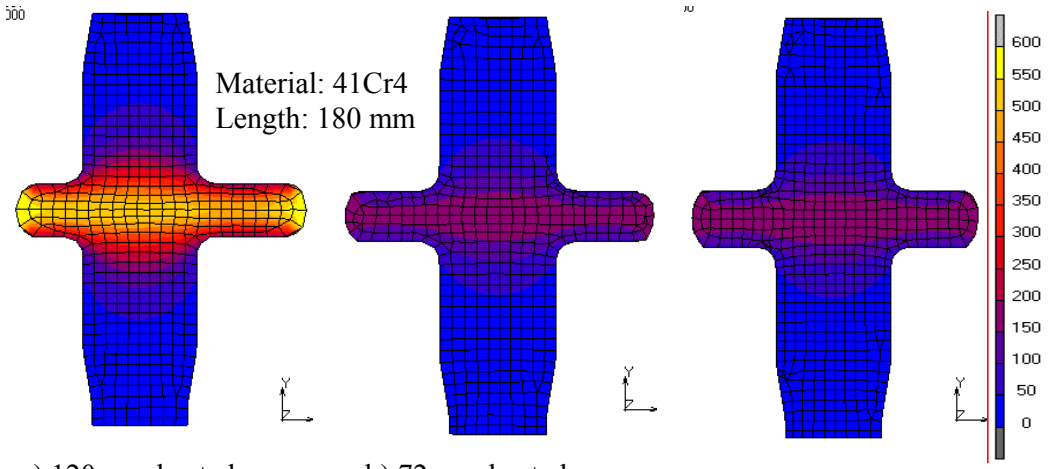

a) 120 mm heated zone b) 72 mm heated zone c) 60 mm heated zone

Figure 7.29 Effect of different heated zone lengths

(Contour shows the temperature profile in °C)

Table 7.6 Simulation Parameters for Simulations for the Effect of heated zone length

Materials Used	41Cr4 (Marc Database)
Initial Conditions	1300 ºC Zone (L_h=60, 72, 98, 120 mm) and all remaining zones are at 25 ºC
Contact Friction	m = 0.2
Cooling time	8 s
Friction Coefficients	m=0.2 (Shear Friction)
Punch Velocity	3 mm/sec
Solver Used	Direct Sparse Solver
Workpiece Length	180 mm
Other properties are same with Table 7.1	

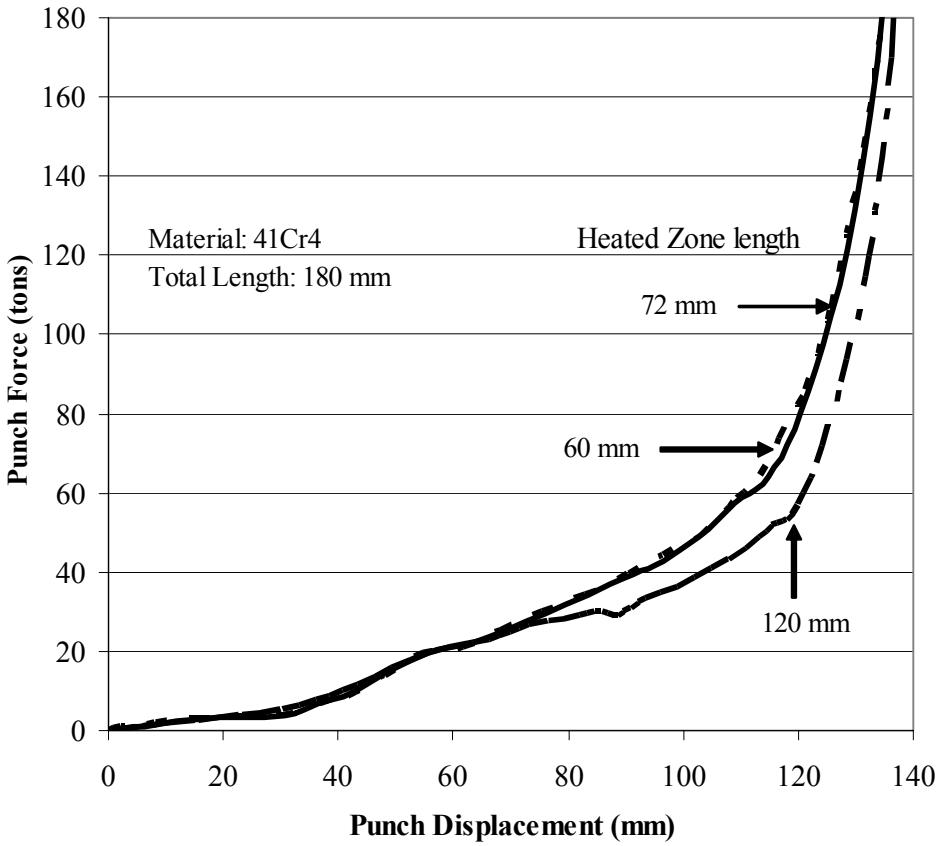

Figure 7.30 Effect of different heated zone lengths on Punch force vs. Punch Displacement

The best results were obtained from the workpiece with 60 mm heated zone length in the simulations. The workpiece with 60 mm heated zone has a symmetric flange. In addition, simulations are made with 16MnCr5 material. The buckling behavior of the 16MnCr5 is different than 41Cr4. None of the models with material 16MnCr5 has buckled. In Figure 7.29 the deformed shapes of the workpieces can be seen the in the middle of the forging process when their flange thicknesses are about 14 mm. Figure 7.30 shows the punch force vs. punch displacement graph. According to this graph as the heated zone length increases the punch force will decrease. This is expected because as the heated zone length is changed the inner temperature profile of the workpiece is also changed. A longer heated zone is a larger heat sink and stores more energy. Thus, the cooling of the workpiece lasts longer. As explained in Section 7.4.1 a high temperature will reduce the required punch force.

7.5 Conclusion

Simultaneous hot and cold forging idea is promising according to the results obtained from FE method. In this chapter, one can find the effect of the parameters on the process. These parameters are heat convection coefficient, cooling time, length of the workpiece, friction, material, heated zone length etc. Also possible failure types were presented that can render the process such as overlapping, necking at the flange root and the buckling.

Heat convection coefficient affects the process adversely. As the heat convection coefficient increases, the cooling rate also increases causing hot zone body temperature to drop. Similar effect is also shown by cooling time. The cooling time includes the handling and transportation time for the workpiece. As the body temperature of the hot zone of the workpiece drops the chances of buckling increases.

The workpiece length affects the slenderness ratio. A low workpiece length means a low s ratio thus preventing buckling.

Punch velocities affect the process both profitable and adversely. Increasing punch velocity causes a drop in the maximum force required and also in the process time.

The drop in the process time causes a drop in cooling time of the workpiece that is desirable. But high punch velocity can cause incomplete extrusion at the ends of the workpiece [Figure 7.23].

The heating zone length will affect the *s* ratio of the hot zone. The important point is that the, uniform temperature zones should not exceed critical s ratios.

The material type also affects the buckling behavior of the workpiece. The material type changes tangential elastic modulus (E_T) and the required punch force.

The characterization of the process and material is very important. The parametrical study showed that the process is sensitive to material data and environmental conditions.

CHAPTER 8

COMPARISON OF FEM WITH EXPERIMENTS

8.1 Introduction

The finite element simulations should be verified with experiments. This verification helps to improve the FEM simulation. In the verification process if the FEM simulation results do not relate with the experimental results then the FEM model used for that simulations should be corrected. In the following sections experimental results will compared with the results of the FEM simulations.

8.2 Cooling Experiments & Simulations

Cooling is difficult to analyze in the simulation because of the complex initial temperature distribution inside the workpiece body. This initial temperature distribution is made by setting one hot zone and letting the temperature to disperse inside the workpiece for a certain amount of time (Figure 8.1). The colored zones in Figure 8.1 refer to different temperature. In the experiments, the workpiece body temperature is measured at certain locations. The verification of the initial workpiece body temperature before the forging is done according to these measurements. The values obtained from the simulations at these locations compared with the experiments.

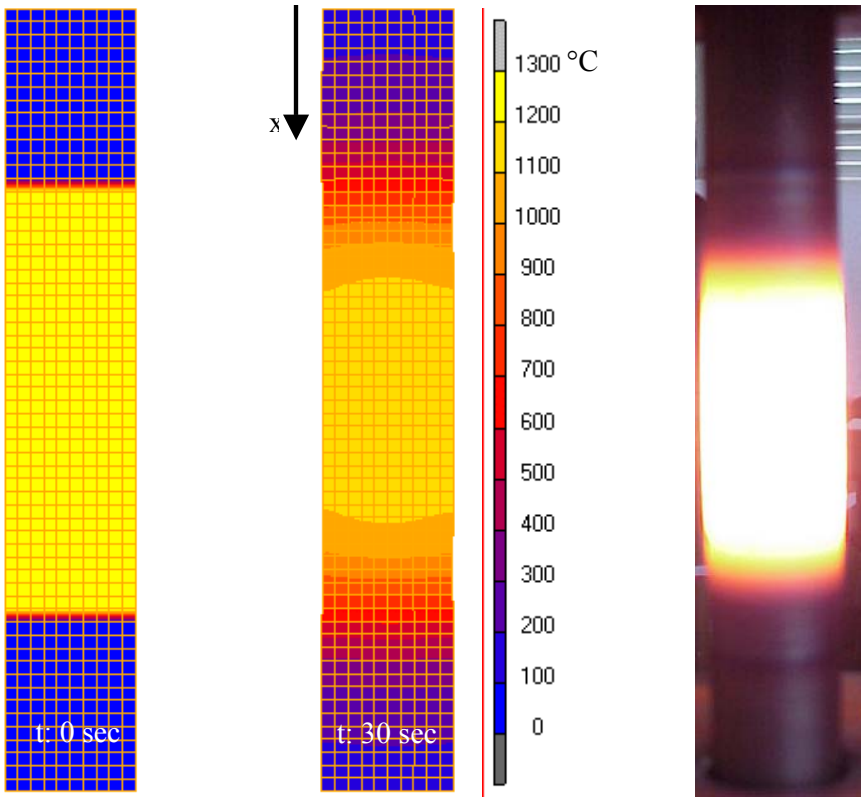

a) Temperature distribution at start of the cooling

b) Temperature distribution after cooling phase

c) Bright colored areas of the workpiece are above 500 °C

Figure 8.1 Distributing the temperature (16MnCr5, Length: 210 mm)

The Figure 8.2 shows the body temperature distribution both in the simulation and the experiments. In the Figure 8.2, it can be seen that there is a difference in the transition zone between FEM result and experimental results. But this difference does not affect the simulation results greatly. The reason is simple the points at 33.3 mm has a difference of 120 ºC but they are both in the cold forging region. At 66.6 mm FEM result and the experimental result have 170 ºC difference. This point is critical because the FEM result fall in to the warm forging region while experimental result is in cold forging region. This can result in difference between punch force result between experiments and the FEM simulations. At the mid-point of the workpiece the FEM result and the experimental result are nearly identical.

This comparison show that the temperature distribution acquired by finite element simulation is not identical to real case but it is satisfactory.

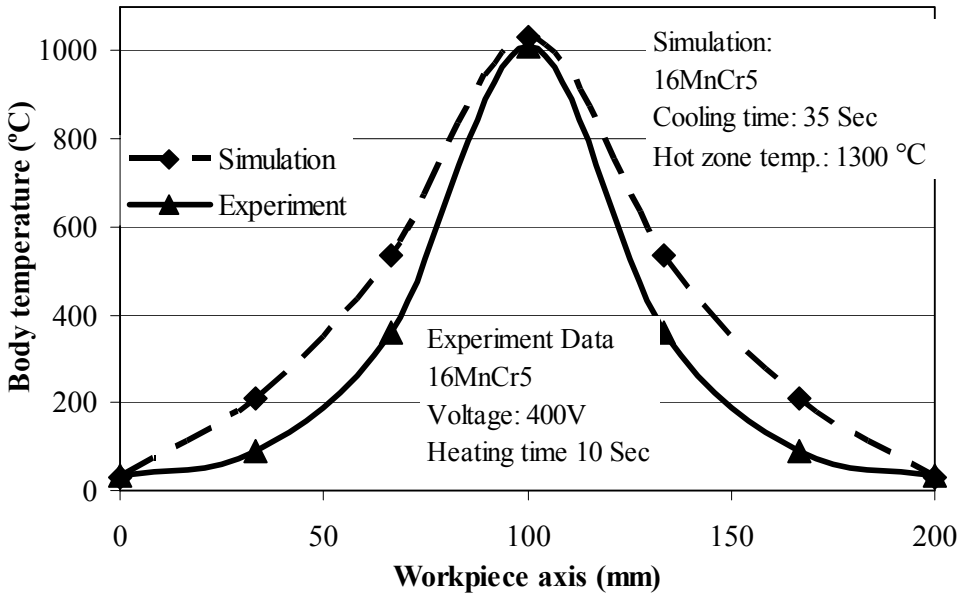

Figure 8.2 Comparison of experiment result with FEM result(1)

In the Figure 8.2, it can be seen that there is a difference in the transition zone between FEM result and experimental results. But this difference does not affect the simulation results greatly. The reason is simple the points at 33.3 mm has a difference of 120 ºC but they are both in the cold forging region. At 66.6 mm FEM result and the experimental result have 170 ºC difference. This point is critical because the FEM result fall in to the warm forging region while experimental result is in cold forging region. This can result in difference between punch force result between experiments and the FEM simulations. At the mid-point of the workpiece the FEM result and the experimental result are nearly identical. This comparison show that the temperature distribution acquired by finite element simulation is not identical to real case but it is satisfactory.

8.3 Forming Experiments & Simulations Comparison

8.3.1 Punch Force Comparison

The punch displacement versus force graph is important for a process. Because these graph shows the required punch force for the process. Also these graphs behavior is somewhat related to the stress-strain graph. The punch displacement versus force graph is a good way of comparing experiments and simulations because of the facts above.

The experimental data were obtained by a force measurement device discussed in Section 5.2.7. In the experiment the workpiece used was 160 mm long and 30 mm in diameter. The workpiece were heated with 450 Volts. A finite element model is built up using a base model. This model is modified according to the workpiece dimensions and the heating voltage. The punch displacement versus force graph can be seen in Figure 8.3. In the Figures 8.4 and 8.5 the corresponding regions of Figure 8.3 can be seen. In region 1, the extrusion and the bulging takes place depending on the temperature of the hot zone. If the temperature of the hot zone is below 500 °C than in region one only extrusion takes place. Region 2 starts as the lands of the dies touch the flange of the workpiece. In this region the cold zones at the ends collides at the center of flange and causes punch force to rise. After the die lands contact the flange area the forces increases steeply. In Figure 7.3, through the end of the process force from the experiments converge to a value. This is due to the press specifications. The punch force reaches to the force limitations of the press causing a speed drop at the end of the process. The punch displacements are calculated by multiplication of time passed with the punch speed. So the experimental results at the end of the force displacement curve is not correct. It should match the FEM curve.

The FEM result for the punch force is not exactly same with the experimental results but they resemble to each other and the differences between them are acceptable. These differences may come from the initial temperature conditions which are not exactly same with the real case. This fact is discussed in section 8.2.

The difference between two may also result because of the flow curve. The flow curve used for the simulation is from the MSC.Marc database. But it is known that materials do not have a unique flow curve.

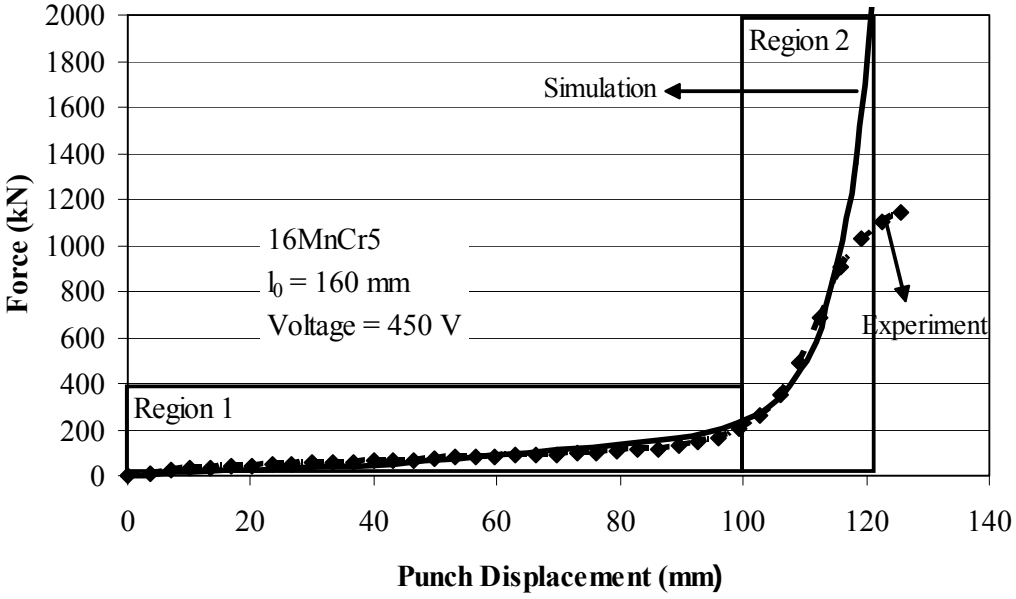

Figure 8.3 Comparison of experiment result with FEM result(2)

8.3.2 Hardness Values Comparison

Hardness values obtained from a process are important for the final product. By using the hardness values it is possible to calculate the strength of the material. In the cold regions of the workpiece it is possible to find hardness values from the yield strength. The experimentally obtained hardness values from the final product will be compared with FEM results. The hardness values from the FEM simulations are calculated by using the modified Tabor's approach [19]. The cold forged area in the simulations has strain values between 0.15 and 0.38 near the hardness measurement point (Figure 8.4). By using the Ludwik's formula (Equation 8.1), the yield strengths calculated with an offset strain of 0.112 are 761 MPa and 829 MPa respectively. The constants used as; K=912.4 and n=0.135.

a) Region 1

b) Region 2

c) Final shape

Figure 8.4 Experiment step by step
(16MnCr5, Length: 160 mm)

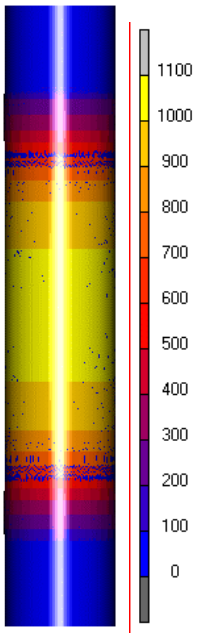

a) Region 1

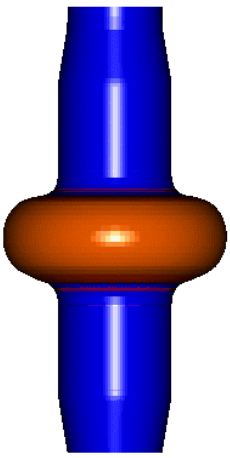

b) Region 2

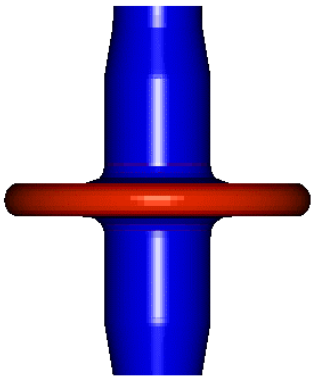

c) Final shape

Figure 8.5 FE Simulation step by step(16MnCr5, Length: 160 mm)

$$Y = K g\varphi^n \tag{8.1}$$

$$HV = 2.475gY \tag{8.2}$$

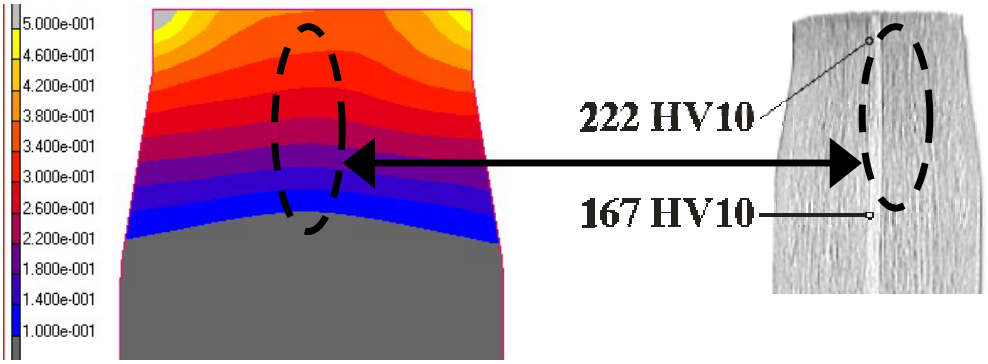

a) FE model
(extruded ends)

b) Experiment
(extruded ends)

Figure 8.6 Hardness comparison between experiments & FE simulation (1)
(16MnCr5, Length: 168 mm)

The strength values found from Equation 8.1 will help to find the hardness values by using the Equation 8.2. From Equation 8.2, the hardness values are found as 188 HV 10 and 205 HV 10 respectively.

The upper bound of these results (205 HV10) has a small error as compared to the experimental value which is about 222 HV 10 (Figure 8.4). The error between the experimental and the FEM result is about 7%. The hardness measurement is also done on a totally cold formed workpiece. The results of the experiment can be seen on Figure 8.7. Experiment of totally cold formed workpiece is compared with simulation using Equations 8.1 and 8.2. The results are plotted on Figures 8.8 and 8.9. In Figure 8.8, the hardness distribution along the workpiece can be seen. The values obtained from FE simulation are similar that are obtained in the experiments. In the FE simulation end points found to be 205 HV10 where the experimental results shows that it is about 215 HV10. At points where there is no deformation,

the experimental and FE simulation results coincide. The values at these points are 167 HV10 for experiments and 168 for FE simulation.

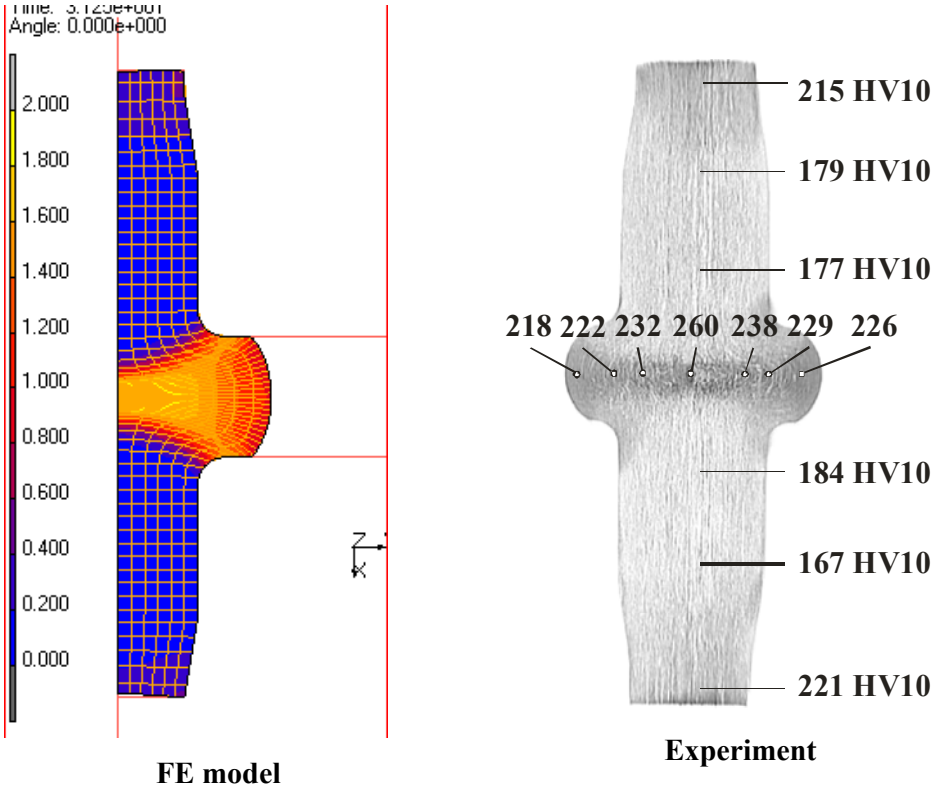

Figure 8.7 Hardness comparison between experiments & FE simulation (2) (16MnCr5, Length: 168 mm, Totally cold formed)

The hardness values near the flange increases steeply as can be seen from Figure 8.8. The maximum hardness value is at the middle of the workpiece for both FE simulation and the experiment and they are 250 HV10 and 260 HV10 respectively. The hardness values at the flange area are higher than other areas in the workpieces. In Figure 8.9 the radial distribution of the hardness values can be seen according to FE simulation. The hardness values obtained from experiment can be seen in Figure 8.7. In the flange area, the highest hardness values are at the center (radially). According to FE simulations the hardness value at the center is about 250 HV10 and decreases linearly to 225 HV10 at the edges of the flange. According to the experiments, maximum hardness values at center starts from 260 HV10 and decreases to 226 HV10 at one side and 218 HV10 at the other side. The behavior of

the decrease in the hardness values at the flange does no seem to be linear. The comparison of the hardness values of the totally cold formed workpiece for FE simulation and the experiments shows a difference of 0.5%-5% depending on the area of calculation. The highest error is at the ends of the workpiece where extrusion takes place.

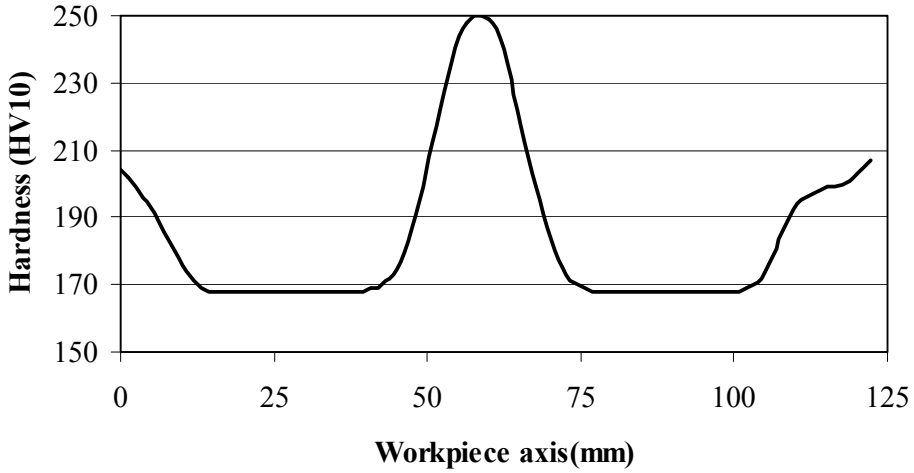

Figure 8.8 Longitudinal hardness values calculated by FE simulation

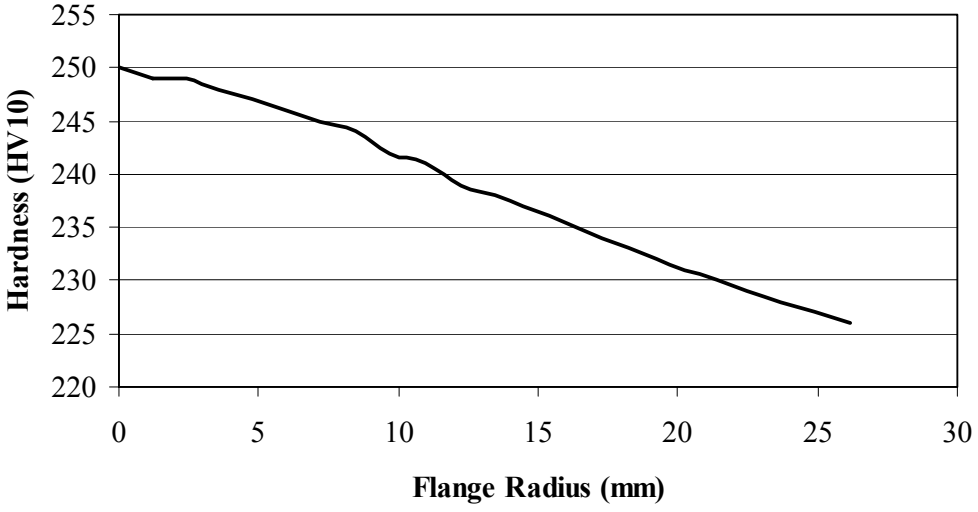

Figure 8.9 Radial hardness values calculated by FE simulation

8.3.3 Qualitative comparison of final geometry of workpieces

The FEM analysis generally is used for a qualitative analysis. In this type analysis the exact results are not the goal of the analysis. The results investigated relative to a base result (e.g. critical points that possible will fail in the process or that have high strains relative to the other parts).

Also the failure types of the process can also be determined by this kind of analysis (e.g. Buckling). How a parameter affects the failure can be investigated. This makes FEM an excellent tool for engineers. In this thesis, the FEM method used to produce quantitative results but these results can also be compared qualitatively with experiments.

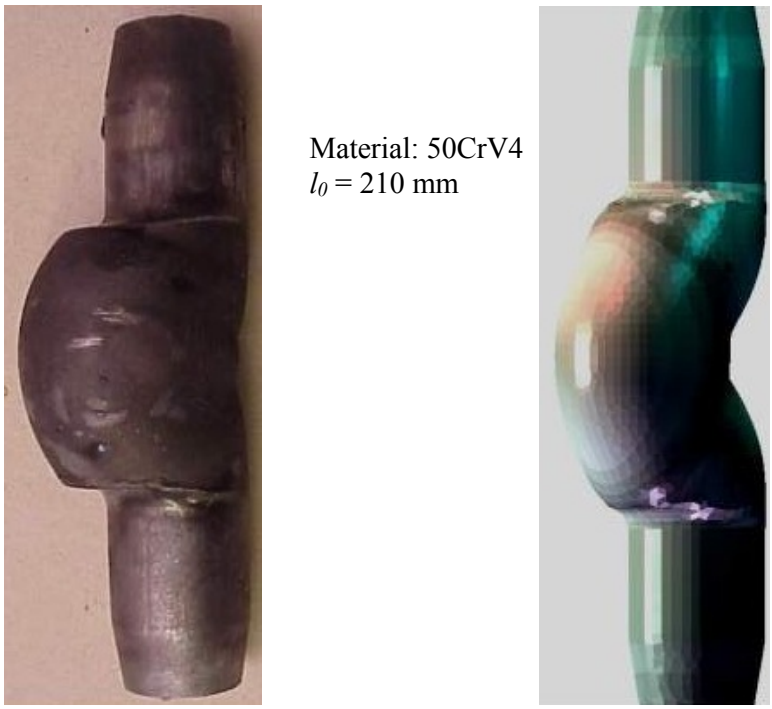

a) Experiment (Heating Voltage = 350 V)

b) FE Model (Initial hot zone temperature at 1300 °C)

Figure 8.10 Buckling in the experiments and in FEM(1)

In Figure 8.10, the buckling of the workpiece can be seen both from the experiment and the FEM. The experimental model material is 50CrV4 with l_0 = 210 mm and heating voltage of 350 V. The FEM model material is 40Cr4 with l_0 = 210 mm and cooling time of 15 s. Both workpieces fail similarly and also another type of buckling also found both in the experiments shown in Figure 8.9. This type of buckling mainly is caused by asymmetric heating of the workpiece. Because of this the hot region flows to one side. This type of buckling also can occur when there is excessive hot region in the flange zone.

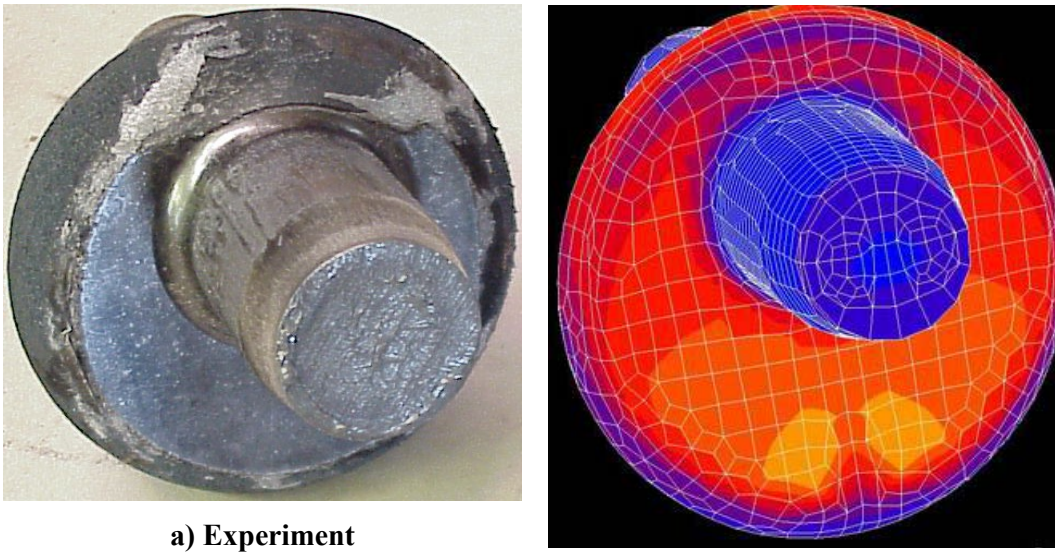

a) Experiment **b) FE Model**

Figure 8.11 Buckling in the experiments and in FEM(2)
Effect of unsymmetrical heating see Figure 5.19
(Material: 16MnCr5, l_0 = 210 mm)

In the Figure 8.11, the experimental model material is 16MnCr4 with l_0 = 200 mm and heating voltage of 450 V with medium coil. The FEM model material is 16MnCr4 with l_0 = 200 mm and cooling time of 10 s. Both are heated unsymmetrically. The result coming from FEM and the experiments are similar. This is discussed also in section 5.4.3.

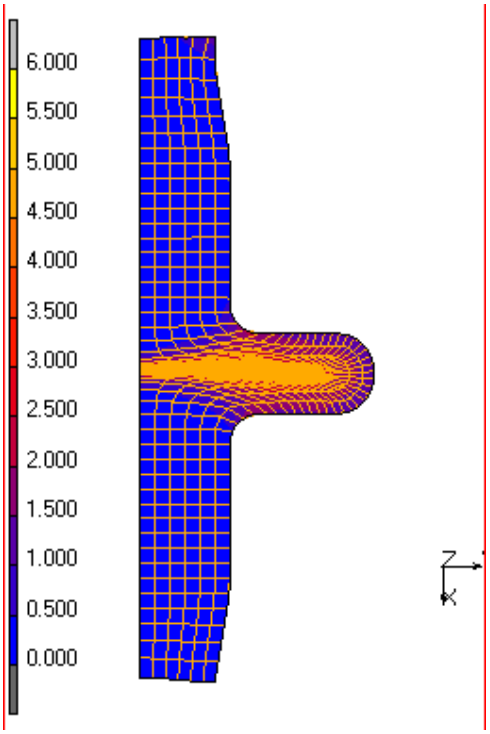

FE model

Experiment

Figure 8.12 Comparison of successful experiments with simulation (1) (16MnCr5, Length: 180 mm)

In Figure 8.12, final shapes from both experiment and FE simulation can be seen. In the experiment the workpiece material was 16MnCr5 with l_0=180 mm and it were heated at 540V with the medium coil. FE model is constructed using the same material and l_0. The cooling phase of the FE model is set to be 10 sec to estimate the heating profile. The FE simulation is run until it has the same flange thickness as the workpiece in the experiment. The workpiece flange thickness is 13.5 mm. At this flange thickness FE model has a flange diameter of 79 mm where as the workpiece has 80 mm. Both the FE model and the workpiece length is about 108 mm. The maximum punch force with 13.5 mm flange thickness is about 170 tons. The limit of hydraulic press used is about 150 tons. Both models have completed extrusion at the ends.

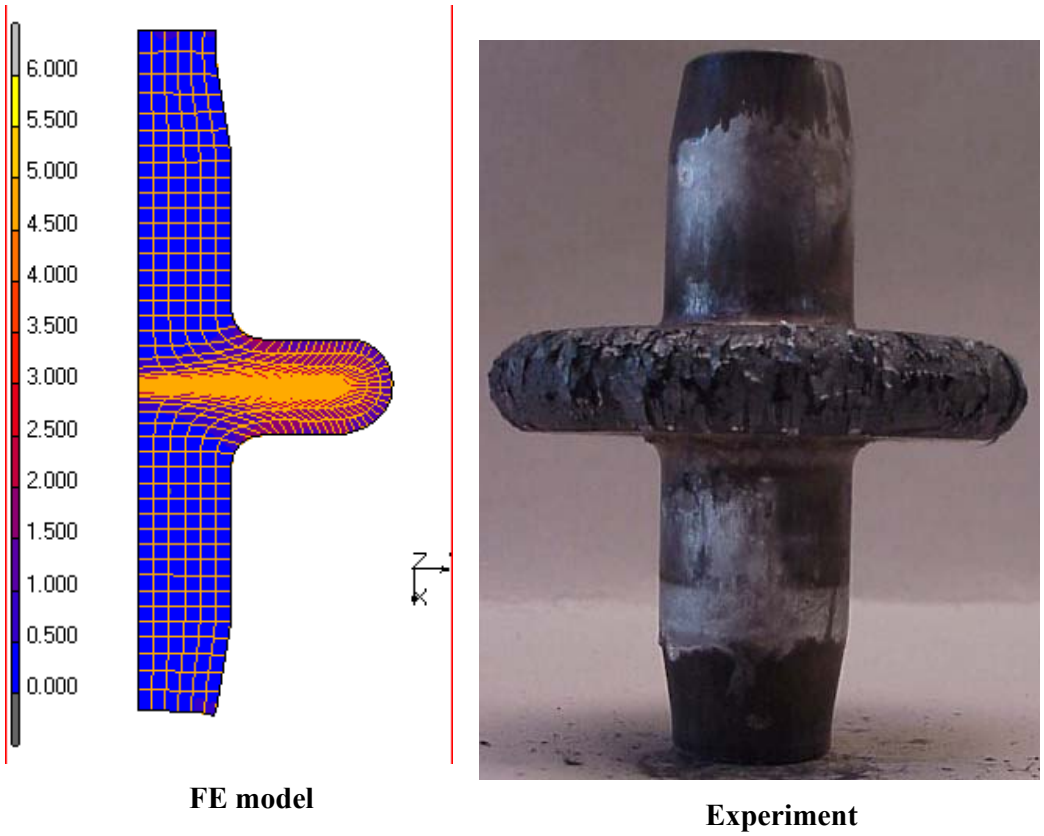

FE model **Experiment**

Figure 8.13 Comparison of successful experiments with simulation (2) (16MnCr5, Length: 200 mm)

Similar to Figure 8.12, Figure 8.13 compares the final geometry of the workpiece to its FE counterpart. The workpiece in Figure 8.13 is also 16MnCr5 with l_0=200 mm and it were heated at 540V with the medium coil. The FE model is constructed with 16MnCr5 with l_0=200 similar to the workpiece. Like the previous model it is also have 10 seconds cooling phase to distribute the temperature in order to obtain a good temperature profile. The workpiece flange thickness 15.4 mm. The FE model has a diameter of 82 mm at same thickness while the workpiece has 84 mm diameter. Both the workpiece and the FE model has a length of 111 mm. The maximum punch force at flange thickness of 15.4 mm is about 180 tons according to FE simulation. The hydraulic press used in the experiments is capable of maximum 150 tons (Table 5.2)

8.4 Conclusion

The FEM method does not give the exact result but it can be close enough to the exact value. Exact results can not be found because of the following facts:

- In FEM there are several assumptions made to simplify the solution.
- The input data for the simulations can not be exact.
- The exact solution is not known and experimentally measured ones already have errors induced because of the equipment tolerances and environmental noise.

This chapter prepared to show the reader the relevance of the results of FEM to the experiments. The results with acceptable accuracy can used to analyze a process. The FEM models used in chapter 7 shows good coherence with the experimental counterparts. This shows that the FE models are satisfactory. The punch force versus displacement diagram has coherence between experimental result and the finite element result. The hardness value resulting from FE simulation and experiment has an error of 7%. Also the temperature before forging diagram obtained by FE simulation is similar to the one obtained in experiments although mid-points have difference about 150 ºC.
Also the shape and the dimensions of final product can be obtained by using FEM. The qualitative analysis shows that the experiment results and the FE simulation results are similar when the dimensions are considered (about 2% error). But the maximum force obtained from FE simulation is higher than the maximum punch force value of the machine (13% - 20% error). This should be because of the difference between the flow curves in the MSC.Marc and workpieces used in the experiments.

These results shows that the FEM model used in thesis are satisfactory and there is no need to duplicate all the simulations in experiments. This was the aim of using FEM.

The FEM simulations can show good coherence to the experiments if the following conditions have been established:

- Accurate material characterization
- Well analyzed process (Boundary, initial conditions)
- Accurate model (implementing boundary and initial conditions)
- Fundamental knowledge of FEA (every process requires different set of values for several parameters. e.g. sheet metal forming uses different parameters then extrusion. Today there some special programs exist only for some type analysis like MSC.Superform which is specialized on sheet metal forming and forging.)

CHAPTER 9

CONCLUSIONS, DISCUSSIONS, RECOMMENDATIONS AND FURTHER STUDIES

The aim of this study was to explore limits of the simultaneous hot and cold forging and possible geometries can be formed by this technique. The workpiece geometry used in this thesis is a solid bar. This solid bar is transformed into a solid bar with a flange by the help of local heating and extruded ends. The possible failures and limitations are understood by the help of experiments and FE analysis. FE analysis helped to reduce number of experiments required to understand the process.

The experiments and the FE analysis showed that the heat distribution along the workpiece affects the process. Non-symmetric heating caused by the induction heater geometries influences buckling of the workpiece. Symmetrical heating should be done in order to prevent buckling. The solution found to be for this problem was turning the workpiece around its axis (Section 5.2.1).

The material type also influences buckling. The hot forging material 41Cr4 tend to buckle more than 16MnCr5. The reason for this behavior is that the 41Cr4 needs more force for forging process at the same temperature. This fact is because of 41Cr4's flow curve is higher than the flow curve of 16MnCr5.

The heating technology is important. The temperature zones, in the workpiece should be sharp rather than having a temperature transition zone. The induction heating seem to be fine but if sharper heating zones are required laser heating technology can be used for complex geometries. Another concern in heating is the time between the heating process ends and the forging process begins. This time affects the temperature boundaries and it should be kept as small as possible.

The flange radius is highly dependent on the heated zone length. As the heated zone length increases the flange radius will also increase. But the limiting factor for the heated zone length is buckling. Long uniform temperature zone tend to buckle. Also as the flange radius increases the possibility of cracking around flange increases. In the experiments, It is observed that the workpieces that have bigger flange radius has severe cracks around the radius. The cracking problem can be because of the high cooling rates and high strains included in the formation of a bigger flange.

The lubrication is very important for the process. In the experiments, the workpieces with insufficient lubrication is observed to have cold welding in the cold extrusion of the ends of the workpiece. This fact leads to early bulging or flange forming without finishing the cold extrusion of the ends of the workpiece. Flange forming without finishing the cold extrusion has one disadvantage. That is encouraging buckling of the workpiece because of the extra workpiece length that should be included in the extrusion of the ends. In the experiments, cold welding prevented by the use of phosphating the workpieces before heating process.

Hardness values obtained with this process are promising. At the start of the experiments it was thought that the hardness values of flange should be low. However, the experiments showed that the situation is opposite. The hardness values are higher than the cold extrusion part of the process. This means that no hardening process is necessary done afterwards. The hardness values can be increased further by spraying water on the surface of the product right after the removal of the punch. Spraying water on to the surface should be done carefully because the workpiece surface can form extreme cracks in the water sprayed area. The hardness values are also analyzed with FE simulations and the hardness values

obtained from the FE simulations by using modified Tabor's approach [19]. The results from experiments agree with the results from FE simulations.

Even though a simple geometry is used in this thesis, the simultaneous hot and cold forging is not limited to this case there are endless possibilities available. For example, with a proper die set up and heating equipment a product with double flanges is possible (Figure 9.1). The die setup can be identical as the one used in this thesis but there should be third die consisting two pieces in the middle of two flanges. The reason of two pieces die is for the easy removal of the workpiece.

More complex shapes can be produces by this technology. By the help of lasers localized heating are possible. Thus complex unsymmetrical parts can be produced (Figure 9.2). Okman [22] is working on the possibilities of forming with laser heating.

Laser heating can produce small hot spots so that only the hot spot and its periphery will form. The laser heating can be applied to many applications.

The heating process effectiveness can also be increased by heating the workpiece on the die so that the transportation time and other inefficiencies can be avoided. This can also reduce human involvement in the process. Thus reduces risks for the workers.

As a conclusion, this study showed us possible failures and the limitations of the process. The effect of each controlled parameter is examined. Thus characteristics of the process are understood. In the examination of final products of the experiments it was seen that the mechanical properties of the products are superior. In a single step the formed flange radius reached 2.5 times the original radius of the workpiece which was restricted by a factor of 2 by conventional forming techniques. This study showed that simultaneous hot and cold forging has a promising future because many parts can be produced in a single step, that are produced in multiple forming steps

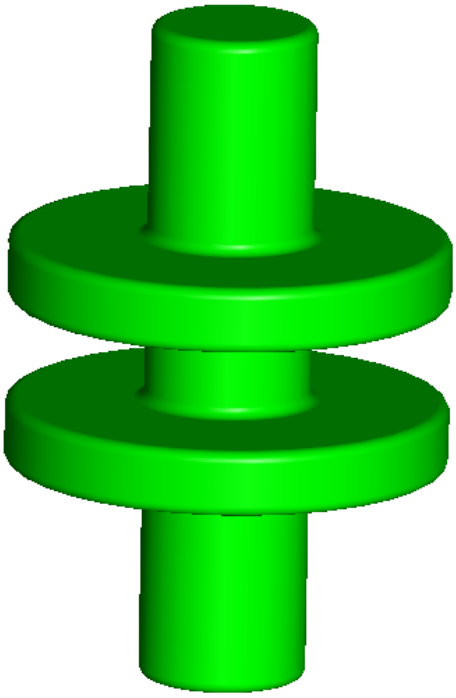

Figure 9.1 Final product with two flanges

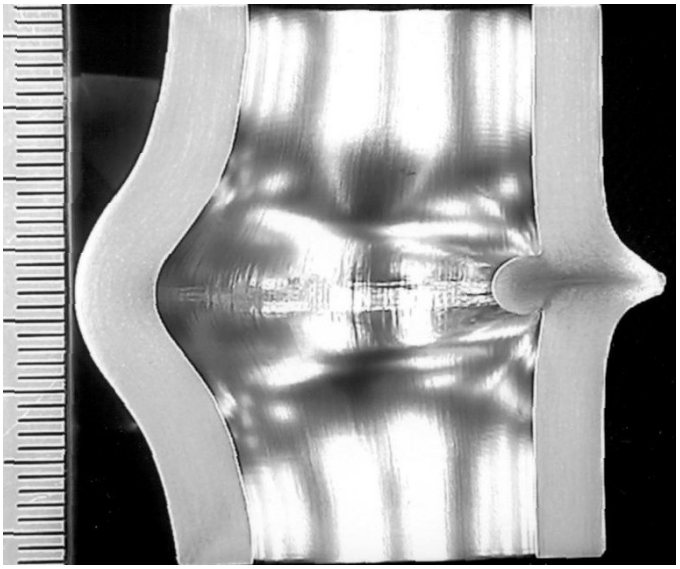

Figure 9.2 Bulge formed by laser heating [22]

.

Also the experience gained from this study showed that the finite element can accelerate the research of new forming techniques. With the help of the FE simulations further modifications can be done depending on the product geometry for the preferences. Another plus for FE simulations is that one cannot obtain detailed information about the process experimentally when compared from the output coming from the simulation.

This thesis about simultaneous hot and cold forging can only be a start. Complete understanding of this process can only be by making experiments and simulations with different heating profiles and geometries. The author believes that this process will draw attention of the industry because of reduced cost of production by this technique is obviously possible.

REFERENCES

[1] A.E. Tekkaya, ME 453 Lecture Notes, METU, ANKARA (2001)

[2] B. Avitzur, Handbook of Metal-Forming Processes, John Wiley & Sons (1983), pp. 907-940

[3] R. Kopp, "Some current developments trends in metal-forming technology", Journal of Materials Processing Technology (1996)

[4] K. Lange, Handbook of Metal Forming, McGraw-Hill (1985), pp. 10.11-13.7

[5] M. Geiger, "On the working accuracy of laser bending", Journal of Materials Processing Technology (1997)

[6] E. Merrygold, "Forging of complex geometries with differential heating", Journal of Materials Processing Technology (1998)

[7] W. D. Callister, "Materials Science and Engineering an Introduction", John Wiley & Sons (1997), pp. 269-279

[8] T. Belytschko, "Non Linear Finite Element Analysis", Chapter 4 (1996)

[9] _____, Autoforge Manual

[10] _____, MARC Command Reference

[11] B. Avitzur, "Metal Forming: Processes and Analysis",McGraw-Hill (1968) p. 331

[12] W. Prager, “Theory of Perfectly Plastic Solids” , John Wiley & Sons (1951)

[13] A. Kurt, “Simultaneous Hot and Cold Forging of Hollow Workpieces” METU, ANKARA (2002)

[14] H. Wagener, “Das Online-Rekristallisationsglühen beim Kaltfliesspressen von Stahl”, Dissertations Druck Darmstadt, Darmstadt (1996)

[15] E. Körner, R. Knödler, “Possibilities of warm extrusion in combination with cold extrusion”, Journal of Materials Processing Technology (1992), Vol. 35, pp 451-465

[16] E. P. DeGarmo, “Materials and Processes in Manufacturing”, Prentice Hall (1997), pp. 453-484

[17] _____, Bucher-Guyer Manual

[18] _____, Ameriterm Co. Induction Manual

[19] A. E. Tekkaya, “Hardness Measurements on Cold Forming Workpieces”, Proceedings of the 6th International Conference on Technology of Plasticity, Nuremberg (1999), pp. 825-830

[20] B. Avitzur, “Limit Analysis of Flow Through Conical Converging Dies”, The journal of Franklin institute (1977), Vol. 299, pp. 339-358

[21] A. E. Tekkaya, ME 543 Lecture Notes, METU, ANKARA (2001)

[22] O. Okman, “Free forming of Solid Parts by Local Laser and Inductıon Heating”, METU, ANKARA (to appear soon)

APPENDIX A

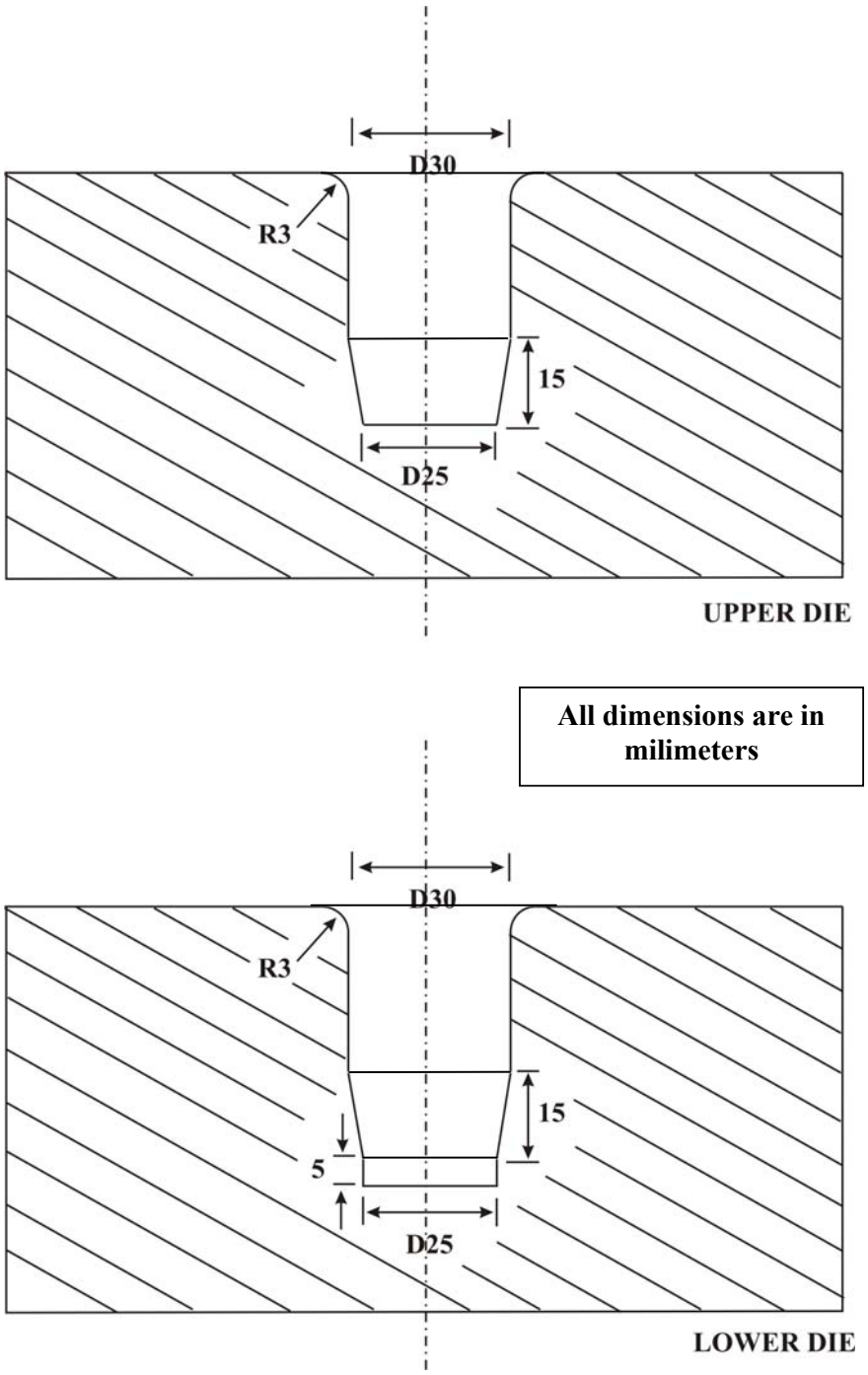

Figure A.1 Die geometry

APPENDIX B

Upper bound solution for extrusion part of the process

$R_f := 10mm \qquad R_0 := 15mm \qquad m := 0.1 \qquad \alpha := \frac{15 \cdot \pi}{180} \qquad \sigma_0 := 402 \cdot 10^6 Pa$

$$R_d := \sqrt{\left[1 + 2 \cdot m \cdot \left[\frac{1 - \left(\frac{R_f}{R_0}\right)}{1 + \frac{R_f}{R_0}}\right]\right]} \cdot \sqrt{\left(\frac{R_f}{R_0}\right)} \cdot R_0 \cdot \cos(\alpha) \qquad R_d = 12.064\ mm$$

$$A(\alpha) := \sqrt{\left[4 \cdot \tan(\alpha)^2 + \left(1 - \frac{R_0}{R_d}\right)^2\right]} - \sqrt{\left[4 \cdot \tan(\alpha)^2 + \left(1 - \frac{R_f}{R_d}\right)^2\right]}$$

Given

$$\frac{R_f}{R_d} + \frac{R_0}{R_d} - \left(\frac{R_d}{R_f} + \frac{R_d}{R_0}\right) \cdot \sec(\alpha)^2 + 2 \cdot m \cdot \left(\frac{R_0}{R_d} - \frac{R_f}{R_d}\right) + A(\alpha) = 0$$

$R_d := Find(R_d) \qquad R_d = 12.137\ mm$

$l_2 := R_0 \cdot \cot(\alpha) - 2 \cdot R_d \cdot \csc(2 \cdot \alpha) \qquad l_2 = 7.431\ mm$

$R_\gamma := R_0 - l_2 \cdot \tan(\alpha) \qquad R_\gamma = 0.013\ m$

$\beta_1 := acot\left[\left(\frac{R_\gamma}{R_f} - 1\right) \cdot \cot(\alpha)\right] \qquad \beta_1 = 41.686\ deg$

$\beta_2 := acot\left[-\left(\frac{R_\gamma}{R_0} - 1\right) \cdot \cot(\alpha)\right] \qquad \beta_2 = 63.646\ deg$

$w_{s1} := \frac{1}{\sqrt{3}} \cdot \frac{\sin(\alpha)}{\sin(\beta_1)\sin(\beta_1 + \alpha)} \qquad w_{s1} = 0.269$

$w_{s2} := \frac{1}{\sqrt{3}} \cdot \frac{\sin(\alpha)}{\sin(\beta_2)\sin(\beta_2 - \alpha)} \qquad w_{s2} = 0.222$

$$w_{fD} := \frac{2 \cdot m}{\sqrt{3}} \cdot \left(\frac{R_0}{R_d} - \frac{R_f}{R_d} \right) \cdot \cot(\alpha) \qquad w_{fD} = 0.178$$

$$F_\alpha(Z) := \int_1^Z \frac{1}{\xi} \cdot \sqrt{\left[4 \cdot \tan(\alpha)^2 + (1 - \xi)^2 \right]} \, d\xi$$

$$w_i := \frac{1}{\sqrt{3}} \cdot \cot(\alpha) \left(F_\alpha\left(\frac{R_0}{R_d} \right) - F_\alpha\left(\frac{R_f}{R_d} \right) \right) \qquad w_i = 0.48$$

$$\sigma_{xb} := \sigma_0 \cdot \left(w_{s1} + w_{s2} + w_{fD} + w_i \right) \qquad \sigma_{xb} = 4.616 \times 10^8 \, Pa$$

$$F := \frac{\pi \cdot {R_0}^2 \cdot \sigma_{xb}}{g} \qquad F = 36.674 \; ton$$

APPENDIX C

What if there was no buckling?

If the buckling was not a problem than the process will have two more kind of failures. This type of failure can only be achieved with the workpieces that will buckle in real life. But even it was possible, there some problems in the process. The long pieces will have more stock for the flange area. If one of the dies hits this stock before the other die than the bulge will collapse on to itself causing a bad failure (Figure C.1). In Figure C.2, the workpiece is very long and the bulge collaples onto itself with his own weight.

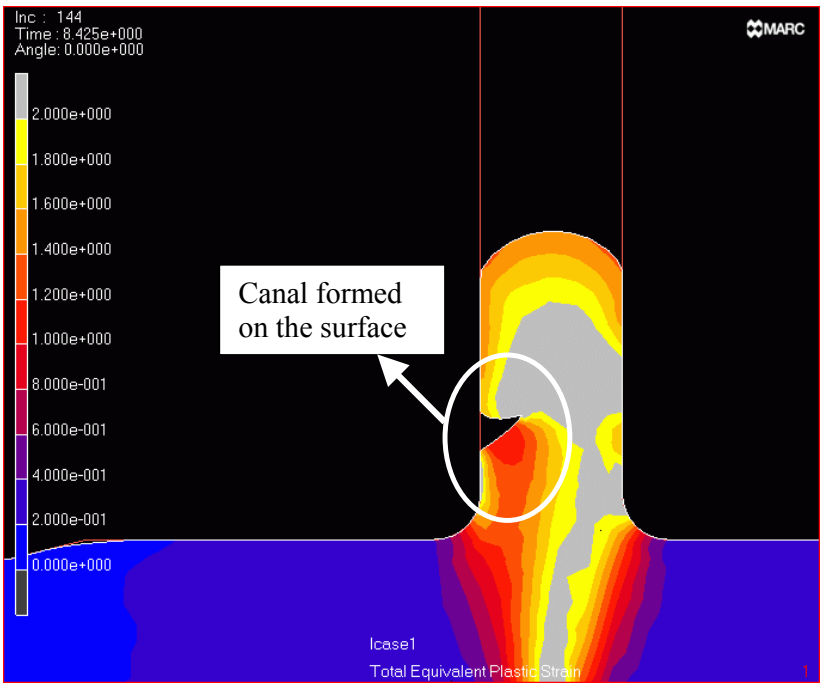

Figure C.1. Failure type one

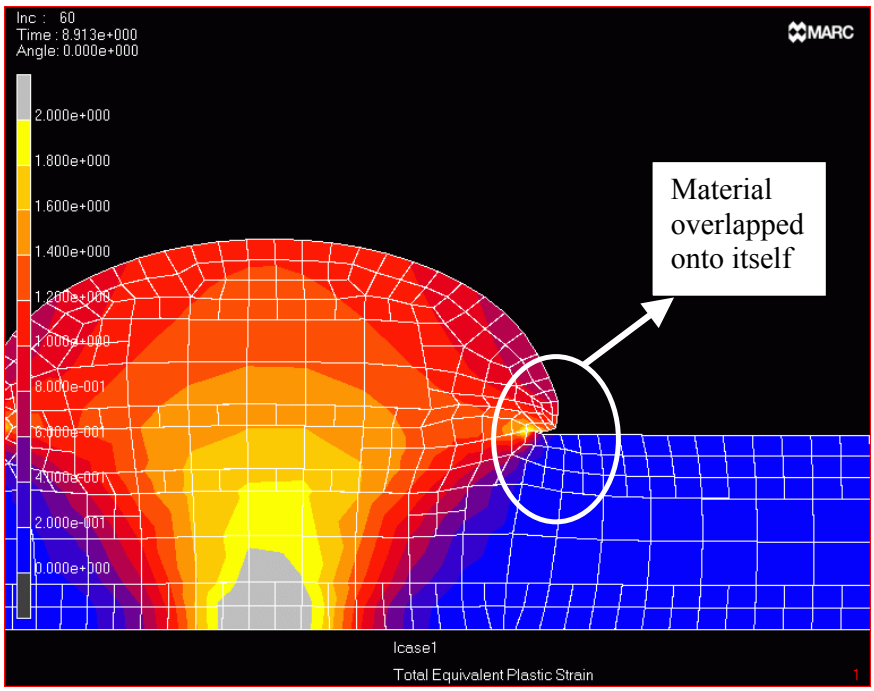

Figure C.2. Failure type two